XPS CHARACTERIZATION OF DILUTE NITRIDE INDIUM GALLIUM ARSINIDE MATERIALS

NANOPOROUS SILICA FOR ACTIVE SAMPLING OF ALDEHYDES

By

SAMANTHA SCUDDER

Bachelor of Science in Biochemistry
Schreiner University
Kerrville, Texas
2016

Submitted to the Faculty of the
Graduate College of the
Oklahoma State University
in partial fulfillment of
the requirements for
the Degree of
DOCTOR OF PHILOSOPHY
December, 2021

XPS CHARACTERIZATION OF DILUTE NITRIDE INDIUM GALLIUM ARSINIDE MATERIALS

NANOPOROUS SILICA FOR ACTIVE SAMPLING OF ALDEHYDES

Dissertation Approved:

Dr. Nicolas Materer

Dissertation Adviser

Dr. Richard Bunce

Dr. Christopher Fennell

Dr. Toby Nelson

Dr. Lisa Mantini

ACKNOWLEDGEMENTS

The completion of my research would not have been possible without the guidance of my advisor, Dr. Nicholas Materer. I would also like to thank the rest of my committee, Dr. Richard Bunce, Dr. Chris Fennel, Dr. Lisa Mantini, and Dr. Toby Nelson, for their encouragement and insight during my writing process.

I thank my former group member Jim Dickinson my lab mates, Dr. Moumita Bhattacharya and Dr. Evgueni Kadossov, for always being there for me and creating countless memories.

Last but not least, I would like to thank my friends and family. My parents Debby and Bill Scudder for their love and unwavering support throughout my endeavors. My sister Megan Scudder for being such an amazing role model and friend. I could not have done it without y'all.

Name: SAMANTHA SCUDDER

Date of Degree: DECEMBER, 2021

Title of Study: XPS CHARACTERIZATION OF DILUTE NITRIDE INDIUM GALLIUM ARSINIDE MATERIALS NANOPOROUS SILICA FOR ACTIVE SAMPLING OF ALDEHYDES

Major Field: CHEMISTRY

Abstract: Multi-junction solar cells have been of recent interest due to their ability to achieve efficiencies as high as 50%. When small amounts of nitrogen are incorporated into the lattice, material quality problems can arise with the formation of Ga-N and Ga-In-N defects. The creation of nonradiative centers, and a decrease in homogeneity results in lower efficiencies. Annealing these solar cells in a nitrogen-rich environment can facilitate the rearrangement to the favorable In-N configuration. X-ray photoelectron spectroscopy was used to characterize these binding configurations to determine if these defects were passivated after annealing and hydrogenation treatments. The nitrogen associated region was studied, illuminating details that have not been seen previously. A second project investigated methods to look at natural or anthropogenic sources of air pollution. Among various indoor air pollutants, low molecular weight aldehydes (formaldehyde and acetaldehyde) have become an important class of volatile organic compounds because of their classification as known or probable human carcinogens. A nanoporous silica sorbent, named OSU-6, was explored in this study for its use in aldehyde sampling with subsequent thermal desorption and gas chromatography/mass spectrometry analysis. A series of analyses were performed to determine the materials sorption capacity in a variety of sampling conditions.

TABLE OF CONTENTS

Chapter Page

LIST OF TABLES

Table Page

LIST OF FIGURES

Figure Page

Figure Page

Figure Page

Figure Page

CHAPTER I

INTRODUCTION

This introduction as well as the following dissertation, is broken into two parts. The first part of this dissertation (Chapters I-IV) examines the passivation of defects in nitrogen dopped multijunction solar cell exploration using X-ray photoelectron spectroscopy (XPS). Multi-junction solar cells are of interest due to their ability to achieve efficiencies as high as 50%. In manufacturing, the small amounts of nitrogen incorporated into the lattice material can create Ga-N and Ga-In-N defects. The creation of these nonradiative centers and a decrease in homogeneity results in lower efficiencies. Annealing these solar cells in a nitrogen-rich environment and hydrogen atom implantations can passivate these defects and possibility facilitate the rearrangement to the favorable In-N configuration. The multijunction solar cells were provided on behalf of the Seller's group at OU, and hydrogenation was made possible by Dr. Khalid Hossain at Amethyst. This work revealed an unknown peak in the nitrogen associated region associated with implanted nitrogen.

This part begins with brief review of XPS (Chapter I and II) and experimental methods outlining calibration and surface treatments. Chapter III summarizes analysis that was conducted on a set of pure semi-conducting samples. Finally, Chapter IV exams actual multi-junction solar cells.

The second part of this dissertation (Chapters V-VII) describes research accomplished with nanoporous silica to be used for aldehyde sampling. Natural or anthropogenic sources of air pollution include fossil fuel combustion, coal-burning power plants, automobile exhaust, and

wood-burning fumes. Urbanized areas are more susceptible to high concentrations and exposure to volatile organic compounds (VOCs) that can have a direct or indirect impact on human health. Among various indoor air pollutants, low molecular weight aldehydes (formaldehyde and acetaldehyde) have become an important class of VOCs because of their classification as a known or probable human carcinogen. Aldehydes can be generated indoors from existing infrastructure or can infiltrate from an external source.

Understanding concentrations of air toxins such as aldehydes within urban areas has been identified as a research priority. A variety of methods are currently used to measure levels of aldehydes in the air such as sorbent-based sampling with subsequent instrumental analysis (Chapter V). The most common technique involves sorbents functionalized with 2,4-Dinitrophenylhydrazine (DNPH). However, quantification interferences occur in the presence of ozone or nitrogen dioxide (NO_2). A nanoporous silica sorbent named OSU-6 was explored in this study for its use in acetaldehyde and formaldehyde sampling followed by thermal desorption and gas chromatography/mass spectrometry (TD-GC/MS) analysis (Chapter VIII). This worked was completed with the help of Dr. Allen Ablett and Dr. Moumita Bhattacharya at Xplosafe.

1. Review of X-ray Photoelectron Spectroscopy

The history of XPS began when Wilhelm Roentgen, a German physicist, discovered X-rays and won a Nobel Prize in 1901.[1] Shortly after Charles Barkla, a British physicist experimented with X-ray scattering later discovering the correlation between X-ray radiation and atomic weight. P.D. Innes outlined a kinetic energy spectrum of photoelectrons excited by radiation of an X-ray tube containing a platinum anode, a magnetic analyzer, and a photographic detector.[2] Manne Siegbahn formed the foundation of the nomenclature of spectroscopy for describing the spectral lines that characterize elements. His son Kai Siegbahn went on to develop XPS which allowed for the accurate measurement of binding energies of photoelectron peaks. He was awarded a Nobel Prize in 1981 for his contribution to the development of high-resolution spectroscopy. [3, 4] When XPS became commercially available in the 70's it has been considered a widely used method for the investigation of the surface of solid materials. Due to its sensitivity, this spectroscopy technique is widely used to analyzed semiconductors, polymers, electronics, and many more materials.

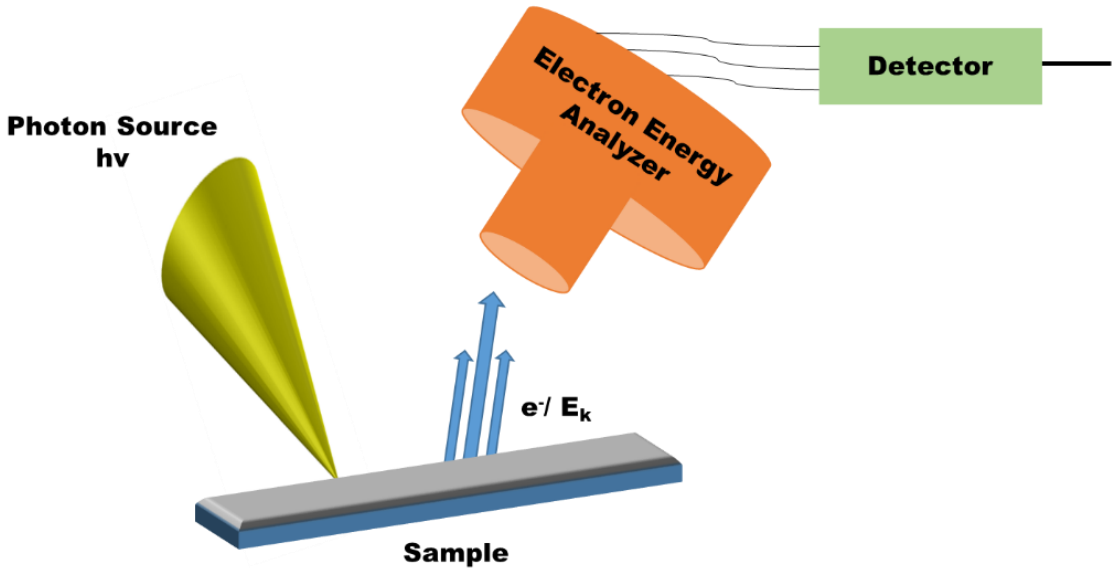

Figure 1.1. Diagram of X-ray Photoelectron Spectroscopy Instrument

The main elements of an XPS instrument include a photon source, an electron energy analyzer, and an electron detector (Figure I-1). Typically, the X-ray source consists of an aluminum (1486.6 eV) or magnesium (1253.6 eV) anode is used to excite the surface of the sample causing the emission of electrons. The electrons are emitted due to the sample's absorbance of electromagnetic radiation, which is why we refer to these electrons as photoelectrons.[5] The amount of energy that is required to pull the electron away from the attractive coulombic force of the nucleus is known as the binding energy (B.E.). The energy provided by the X-ray is used to overcome these forces. The energy of the X-ray is greater than the binding energy of the electron. Thus, the binding energy of the electron can be calculated by the following equation:

$$E_B = E_{hv} - E_K \qquad \text{[Equation I-1]}$$

Where (E_{hv}) is the energy of the X-ray photon and (E_K) is the measured kinetic energy of the electron. The X-rays do penetrate deeper than the surface of the sample (10 nm) however, the emitted electrons collide elastically or inelastically with the electrons in the upper layers. Elastic collisions do not alter the kinetic energy of the electron, while inelastic collisions cause a decrease in energy. The inelastically scattered electrons tend to form a spectrum background are not counted if they do not escape the lattice.[6]

The photoelectrons that are ejected from the sample are highly energetic particles moving hundreds of thousands of meters per second and would collide with the nearest gas molecule in air, so XPS is frequently performed in ultra-high vacuum (UHV) conditions. The average distance the electron will travel between inelastic collisions is defined as the inelastic mean free path (IMFP λ). Most of the photoelectrons (3σ or 99.7%) will come from 3λ of depth. A photoelectron with a kinetic energy of 100 eV in the gas phase at 1 torr has the mean free path of

approximately 1mm. The pressure under UHV is typically 1 x 10^{-6} - 1 x 10^{-11} torr, which drastically changes the mean free path of the electron to approximately 40km.

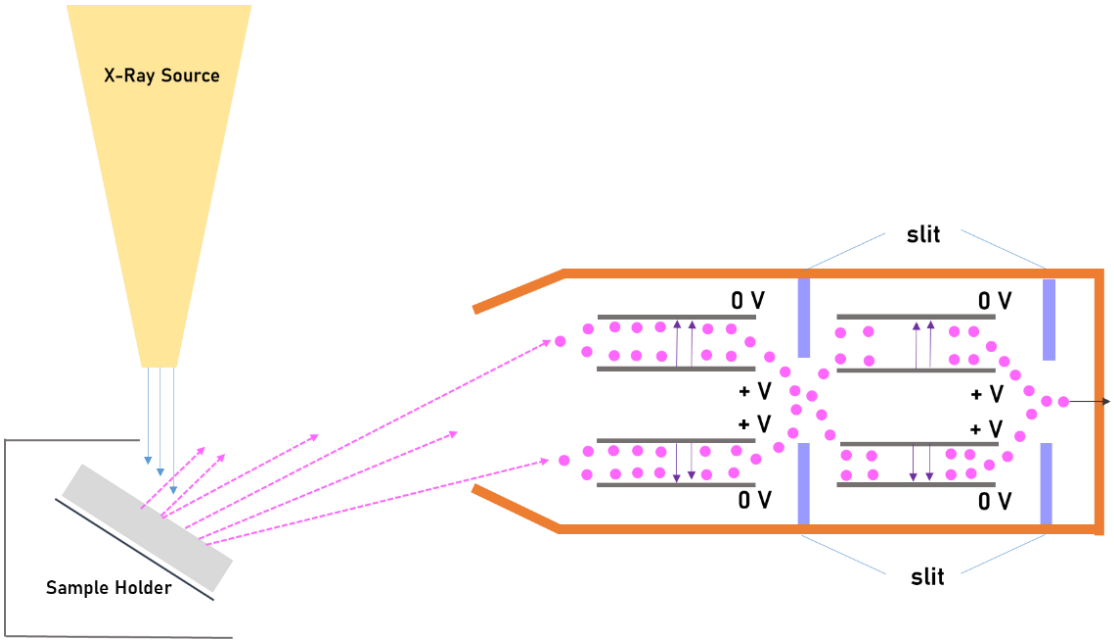

Figure 1.2. Diagram of cylindrical mirror analyzer (CMA)

After the photoelectrons are ejected, they can then travel into the analyzer. The analyzer is a cylindrical mirror analyzer (CMA) which consists of two concentric cylindrical electrodes held at different electrical potentials creating an electrostatic field (Figure 1-2), this guarantees that only photoelectrons with specific energies can reach the detector, this is known as the pass energy (P.E.). [7] The field between the cylinders is given by $\ln(r_2/r_1)$, resulting from the focusing condition:

$$E_0 = \frac{eVK_0}{\ln(r_2/r_1)} \qquad \text{[Equation I-2]}$$

The second-order focusing conditions are obtained for the special case where $K_0 = 1.31$, the entrance angle $\alpha_e = 42.3°$, and the distance *L* between *S* and *F* is given by $L = 6.130$. The photoelectrons are recorded in a small kinetic energy range and determine the resolution of the analyzer. Sweeping the voltages of the electrodes generate the spectrum. If the surface contains no charging the kinetic energy (E_k) can be quantified by the Einstein equation where *hv* is the energy of the X-ray quantum, E_B is the binding energy of the core level electron, and Φ is the sample's work function.

$$E_K = hv - E_B - \Phi \qquad \text{[Equation I-3]}$$

This is essentially conservation of energy Equation I-3 where the work function can be viewed as an adjustable instrument parameter to account for the loss of energy from the photoelectron emission and absorption by the detector.[8] For materials containing two or more elements (except H and He) the elemental concentration from the XPS survey spectrum can be determined using Equation I-4.

$$X_A = \frac{I_A/S_A}{\sum_n I_n/S_n} \qquad \text{[Equation I-4]}$$

Where X_A, I_A, and S_A are the atomic concentrations, the relative sensitivity factor (RSF) for an element and peak area *A*, in a surface having *n* elements. A library of RSF values has been compiled for the Physical Electronics spectrometer and are based on the empirically derived cross-sections of Wagner. [9] Using a subtraction algorithm any contributions from the energy loss background to the photoelectron peak intensities can be removed.

The XPS spectrum consists of peaks from the core-level electrons which are well defined by the binding energy and electronic state of atoms. The binding energy of the core level electron depends on the neighboring atoms as well. If there is a difference in lattice parameters, oxidation states, and molecular environment, shifts in the binding energies for an element can arise. [10] A chemical shift or binding energy shift can also occur due to environmental effects. For samples with charged surfaces, an energy scale can easily be established by referencing the electron energies to the Fermi energy of the spectrum.

The photoemission process is the transition from the initial electronic state to the final ionized state. The initial state effects arise from the electron structure of the material before ionization which can include spin-induced interactions and Coulombic interactions. Coulombic interactions are controlled by the local chemical environment and electron structure of the atom. These effects are commonly observed in the binding energy scale, a peak shift (chemical shift) can be seen with a change in the formal oxidation state of the element. When the number of valance electrons decrease, weaker screening of the core level hole is observed, so the photoelectron ejected from this site will have stronger Coulombic attraction and will reach the detector at a lower kinetic energy and be observed at a high binding energy. The kinetic energy of the ejected electron increases and the binding energy decreases with increased screening of the nucleus from the addition of valence electron charge.

Energy calibration for non-conducting samples is more complicated because electrons that are ejected from the sample cause a potential difference to occur between the sample and spectrometer. This can result in a retarding field that affects electrons leaving the surface and can cause a significant shift in peaks (up to 150 eV). To mitigate this effect, charge compensation is designed to replace the electrons ejected from the sample. [11, 12]

There are multiple types of lines that are observed in the XPS spectra. Photoelectron lines are most commonly observed and are frequently outlined in XPS catalogs. The photoelectron spectral lines are identified by the shell from which the electrons were emitted and their electronic configuration (1s, 2s, 2p, etc.).

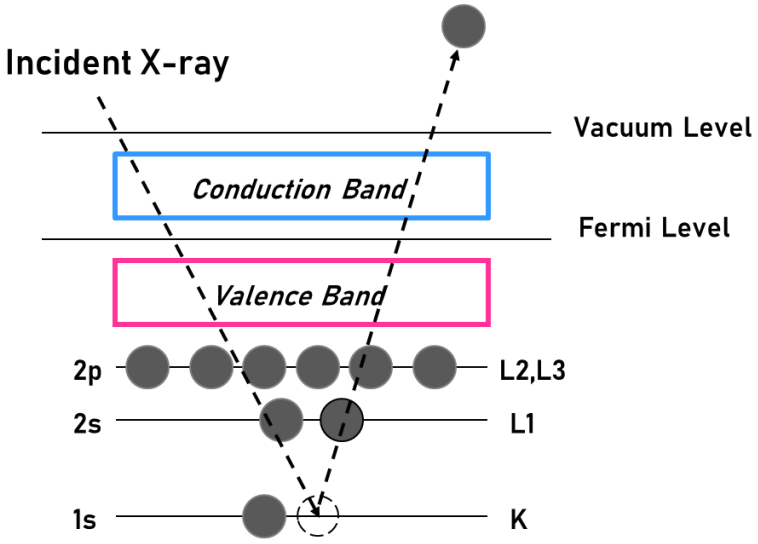

Figure 1.3. Schematic diagram of the core-level-photoelectron emission process

Note: Adapted from Practical Materials Characterization.

Auger lines can arise from the decay of a more energetic electron to fill the vacant hole (transition from L to K shell) created by the X-ray photon to conserve energy (Figure I-4). If the spectrum is plotted using the binding energy the Auger peaks will appear at different locations based on the X-ray anode used (Mg or Al). Satellite peaks (shake-off and shake-up) are also observed in an XPS spectrum though less common than Auger lines. A monochromatic X-ray source creates satellite peaks offset from the primary spectral lines due to a sudden change in Coulombic potential when the core electron is ejected, it passes through the valance band of the atom. Due to the interaction between the photoelectron and other electrons, there is an increased probability for loss of a specific amount of energy (Plasmon loss peaks). [13]

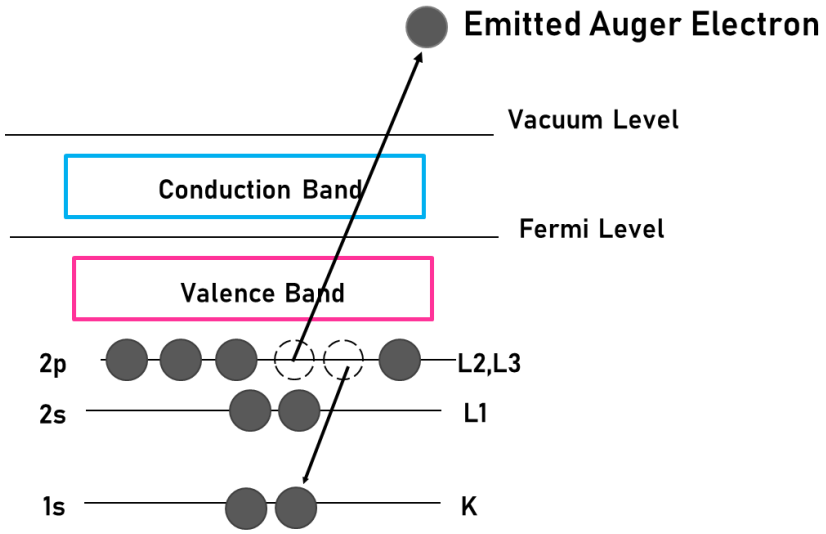

Figure 1.4. Schematic diagram of Auger electron emission process

Note: Adapted from Practical Materials Characterization.

The peaks position, and intensity are used to quantify the XPS spectra. The position allows us to identify the element and chemical composition, while the intensity measures the amount of material on the surface. The width of the peak (ΔE) is defined as the full width at half maximum (FWHM), assuming the peaks are Gaussian-Lorentzian shaped, ΔE can be calculated by Equation I-5.

$$\Delta E^2 = \Delta E^2_{\text{peak}} + \Delta E^2_{\text{instrument}} \qquad \text{[Equation I-5]}$$

Where ΔE_{peak} is the width of the XPS peak, $\Delta E_{instrument}$ is the resolution of the instrument which is affected by the pass energy, slit width, and line width of the X-rays. The peak can be broadened by charging of the sample (insulating materials), energy uncertainty (Heisenberg's), inhomogeneity in the sample, or instrumental broadening. When multiple chemical states of the same element coexist in the sample numerous overlapping components can be present in the

peak. Another peak of the same element that does not overlap should be used to quantify the peak. Identifying the sharpest peaks, which tend to be peaks with the highest orbital angular momentum in each shell (1s, 2p,3d, 4f), is easier to find and perform a background subtraction on. The estimation of peak shape and stoichiometry can only be quantified after the background is subtracted. The most common backgrounds are linear, Shirley, and Tougaard. [14-16] Peak-fitting is typically created from a set of Gaussian/Lorentzian line shapes, and careful modeling construction is essential for an accurate representation of the data.

2. Energy Scale Calibration

When assessing the binding energies from the XPS spectrum one of the most essential steps relies on accurately calibrating the energy scale of the spectrometer. There are various methods in the literature for binding energy calibration. The binding energy scale referencing the adventitious carbon (C 1s) peak as an internal standard is integrated into the International Organization for Standardization method.[23] [24] This peak is located at 284.5 eV and is used to assign to the work function offset when calibrating the binding energy scale. The binding energy scale is calibrated with respect to the Fermi level and the kinetic energy of the photoelectrons that are measured by the spectrometer. The binding energy of the photoelectron depends on the work function of the spectrometer and not the sample and is typically scaled up to the Fermi level. The typical method of calibrating the electron spectrometer relies on measuring the binding energies of several peaks that span the kinetic energy range of the spectrometer. [25]

We had originally measured the multi-junction solar cells in chapter IV using an incorrect work function offset. After further evaluation of the spectra and referencing the literature, we decided to recalibrate the binding energy scale to get a more accurate representation of the materials. This was conducted by measuring the binding energy of elements in the sample and correcting them using a reference manual for the accurate binding energy. The table below shows the raw data vs. the corrected data and a graph of the two values showing a linear relationship.

Table 1.1. raw and corrected binding energies collected via XPS used in energy scale calibration

Peak	Raw Data (eV)	Corrected (eV)
Oxygen 1s	520.75	531
Oxygen 2s	18	23
Indium $3d_{5/2}$	442.75	452.2
Indium $3d_{3/2}$	435.5	446.6
Carbon 1s	279.25	284.5
Arsenic 3p3	138.5	143
Gallium 3p	102	104.75

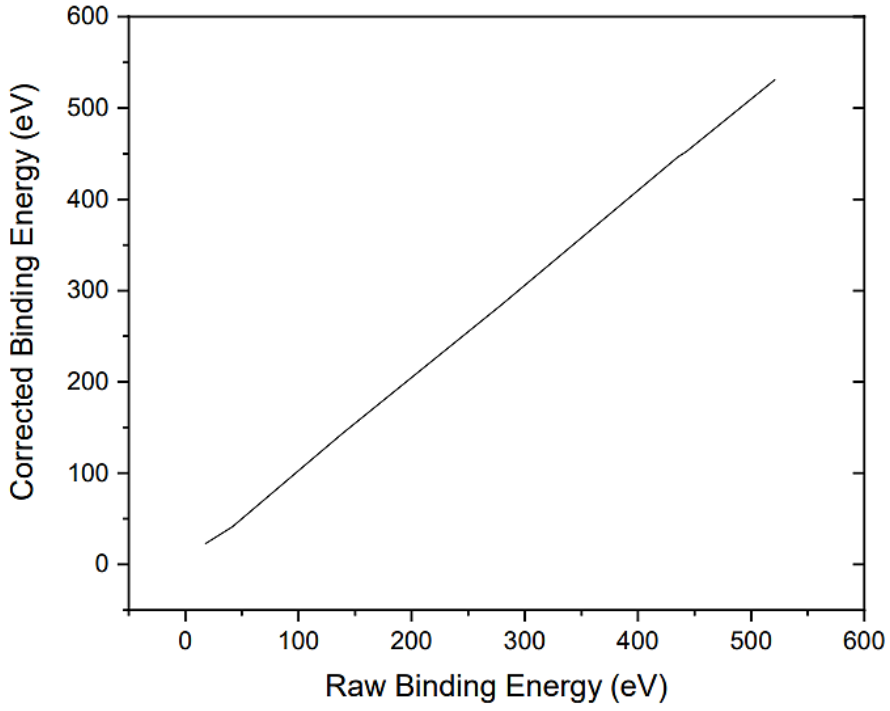

Figure 1.5. Plot of raw binding energy data (eV) vs. corrected binding energy data (eV) for Oxygen 1s, Oxygen 2s, Indium $3d_{5/2}$, Indium $3d_{3/2}$, Carbon 1s, Arsenic 3p3, and Gallium 3p

After the binding energy scale was properly corrected using the reference peaks the appropriate work function offset could be applied and accurate binding energies could be determined. Following the calibration, the C 1s peak was still utilized as a reference prior to every analysis to properly align the sample and verify the energy scale.

3. Argon Sputtering

Monoatomic depth profiling is a destructive technique that uses an ion beam to etch the top layers or contaminations off the surface of the material. Non-destructive techniques rely on energy and angle dependence of the depth of the ejected electrons. However, this technique is limited to the depth range of the attenuation length in the energy range of the electrons used, which is related to the inelastic mean free path.[17] Typically, argon or xenon are used to reduce the inclusion of the primary ions. Ion beam sputtering utilizes an ion source to generate a focused ion beam directed at the sample. When high voltage is applied (2-10 keV) to the anode an electrostatic field is established inside the ion sources, this confirms the electrons around a saddle point in the center of the source. After the argon gas is injected into the ion source the high electrostatic field causes the gas to ionize forming a plasma inside the source's region. These ions are then accelerated from the anode to the cathode creating a collimated ion beam. The sample is etched by rastering the argon ion beam over a known surface area, the sputter yield determines the rate at which the surface is etched during a depth profile represented by the following equation:

$$\text{Sputter yield} = \text{Number of atoms removed} / \text{Number of incident ions} \qquad \text{[Equation I-6]}$$

The sputter yield can be increased by increasing the angle of incidence (maximum= 60°). If the ion beam energy is too high atomic mixing in solid samples can occur, so low ion energy with high masses results in the best depth resolution. Upon sputtering, material from the surface is removed, which causes atoms to become displaced and form empty spaces to which argon can implant. Various factors conditions must be considered when optimizing the profiles. [18-20]

4. Nitrogen Sputtering

In the case of the pure samples of GaAs, InAs, and InGaAs that were used for references the specimens were chemically etched with a 2:1 citric acid/30% hydrogen peroxide solution for 60 seconds. Following the wet etching, the samples were loaded into the XPS chamber where it was allowed to pump down to a pressure of 1 x 10^{-9} torr overnight. Once the appropriate vacuum was reached the samples were moved into the sputtering position where they were bombarded with argon ions at 2 keV with a beam intensity of 1-10 μA cm^2 in an 8 mm x 8 mm raster for 20minutes/cm with an incident angle of 55°.

An XPS spectrum was first obtained following argon sputtering. The samples were moved back to the sputter position for nitrogen implantation. This was conducted at the same base pressure (10^{-9} torr) as argon sputtering. The samples were implanted with N_2^+ using research plus nitrogen gas (99.9999%) at a beam energy of 4 keV. The samples were sputtered in a 1 cm x 1 cm raster for 5 mins/cm. Once the samples were implanted with nitrogen, they were transferred back into the XPS analysis chamber and analyzed with an Mg Kα anode (hω = 1253.6 eV) at pass energies of 50 eV for high-resolution scans, and 100 eV for survey scans.

CHAPTER II

MULTI-JUNCTION SOLAR CELLS AND STANDARD SAMPLES PROCESSING

1. Multi-Junction Solar Cells

The 1 μm thick $Ga_{0.91}In_{0.1}N_{0.03}As_{0.97}$ multijunction solar cells were grown by the Sellers group at The University of Oklahoma by molecular beam epitaxy at 420° C on a GaAs substrate capped by an undoped 75 nm GaAs layer[21]. To generate nitrogen radicals a high purity N_2 radio frequency plasma (ADDON) source was used. Prior to growth, a GaAs buffer of 550 nm was deposited on the GaInNAs films at 580° C. After the samples were grown, they were originally annealed in a nitrogen-rich environment at 850°, 600°, and 300° C for 30 seconds. Following annealing, a piece of each sample was hydrogenated using a UV-activated process at a dosage of $1.1x\ 10^{15}$ atoms per cm^2. [22] One GaInNAs sample was left as grown without RTA or hydrogenation. Confirmation of hydrogen penetration was achieved by the use of ion beam analysis, which indicated a penetration depth of 2μm.

The GaInNAs samples were initially analyzed with a Physical Electronics Inc. X-ray photoelectron spectroscopy instrument under ultra-high vacuum (UHV) working at a pressure of 1×10^{-9} torr. To ensure the spectrum was only influenced by the samples, they were placed on a piece of carbon tape before being inserted into the vacuum chamber.

The samples were then mounted on a stainless steel sample holder. A gate valve connects the two chambers and is only open to the atmosphere when the sample is being transferred and is thought to be mildly contaminated. The sample holder inside the loading chamber is connected to a long transfer arm that is manually controlled by a motor. Once in place, the loading chamber was allowed to pump down (1×10^{-9} torr) overnight. After the appropriate vacuum is obtained the gate valve connecting the two chambers is opened and the sample holder is moved into the main chamber. Most of the experiments were performed using the non-monochromatic Mg K_α anode ($h\omega = 1253.6$ eV) to eliminate Auger peaks that are observed in the binding energy regions of interest. Some experiments were conducted using the Al K_α ($h\omega = 1486.6$ eV) which was non-ideal for the samples containing gallium because of the Auger Ga $L_2M_{4.5}M_{4.5}$ transition. The energy scale linearity was calibrated by the dual anode by setting an energy difference of 223 eV between the two Ag $3d_{5/2}$ peaks. Electrons that were ejected from the samples were analyzed using a cylindrical mirror analyzer (CMA) operating in the constant analyzer energy mode. The pass energy was set to 100 eV for the survey of the whole spectrum, and 50 eV for the multiplex analysis of specific binding energy regions which was defined as the width of the Ag $3d_{5/2}$ peak at half its magnitude. The spectrometer was calibrated by setting the binding energy of the C 1s peak to 284.5.

2. Capping Layer Removal

The undoped GaAs capping layer was removed with a chemical etch using a 25% aqueous solution of NH_3 (ammonia hydroxide) for 60 seconds, this method interfered with an accurate analysis of the samples.[26] A new piece of the sample was etched using a 2:1 citric acid/30% hydrogen peroxide solution for 60 seconds. The GaAs capping layer was removed at an etch rate of 14.3 Å/cycle.[27] The samples were analyzed with XPS and etched in the peroxide solution once more. After analyzing the spectra an error in the energy scale was detected, so proper adjustments were made, shifting peaks to their correct binding energies. The peaks were resolved by curve

fitting with a product of Gaussian and Lorentzian lines. The intensities were determined as integrated peak areas with a linear background. On the fitted components, the FWMH of Ga-N N1s peak and the In $3d_{5/2}$ peak were fixed. This allowed for changes in the surface order, the FWMH was allowed to vary in a narrow margin.

For depth profiling analysis, the samples were sputtered etched with Physical Electronics Inc ion gun fed by high-purity argon gas at 2 keV with a beam intensity of 1-10 μA per cm^2 with a base pressure in the chamber of 1×10^{-9} torr. The samples were sputtered in an 8 mm x 8 mm raster for 20minutes/cm with an incident angle of 55°. The samples were analyzed with XPS and sputtered using the same conditions once more.

3. Standard Samples

A set of standard samples were obtained to determine what elements were influencing the formation of certain peaks in the spectra, particularly in the nitrogen associated region. The following samples were obtained: GaInAs, InAs, GaAs, and GaP. These samples underwent the same chemical etching treatment and sputtering method as the solar cells. Once the samples were treated, they were split into two, half of the sample was analyzed as is with XPS. The other half of the samples were sent to amethyst for hydrogenation at the same dosage and rate as the GaInNAs samples (1.1×10^{15} atoms per cm^2).

4. GaN Samples

The acquired GaN samples were grown on (0001) sapphire using a vertical hydride vapor phase epitaxy method on an orientated sapphire substrate.[28] The wafer was divided into multiple pieces for different oxidation treatments. The first oxidation treatment was performed in the XPS transfer chamber, which was filled with oxygen to 10 psi and left for 24 hours. After XPS analysis a more aggressive method was required to oxidize the surface. The samples were then etched using a 1:1 HCl: DI H_2O solution for 60 seconds followed by a thorough DI water rinse.

They were then blown dry with N_2 to remove any moisture left on the surface. After the chemical etch, the samples were subjected to dry oxidation. The samples were placed in a quartz tube furnace (Thermolyne 21100) and dry air was allowed to purge the system for 5 minutes at room temperature. Oxygen was then passed through the tube at a flow rate of 100 ml/min at temperatures of 400 °C, 600 °C, and 800 °C for 30 minutes to 4 hours. [29-32] The samples were allowed to cool to room temperature before XPS analysis. The samples were then sputtered with argon *in-situ* (8mm x 8mm^2 raster for 20minutes/cm with an incident angle of 55°) twice to remove the oxide overlayer before analyzing again. To analyze oxidation effects of the citric acid/hydrogen peroxide etch on the GaN samples they were etched using the same method as the GaInNAs samples. Prior to peroxide etch the samples were cleaned for 60 seconds in a 1:1 HCl: DI H_2O solution. After subsequent peroxide etch the samples were blown dry with N_2 and analyzed with XPS.

CHAPTER III

PURE SEMI-CONDUCTING REFERENCE SAMPLES

1. Introduction

To ensure that reliable and useful information was being obtained from our analysis, we acquired a set of high-quality semiconducting wafers to be used as standards to reference our measurements from the solar cells (Chapter IV). The electron binding energies allow for elemental identification and with small shifts (a few eV) providing information about chemical states of the elements of interest so it's important to scrutinize pure forms of these materials. The following samples were obtained for XPS measurements: GaInAs, InAs, GaAs, and GaP. These samples were initially analyzed without any chemical treatments or sputtering. A survey scan was originally performed on all of the samples to allow for a quantitative elemental composition determination. Binding energies become more important with the multi-junction solar cells and to quantify the binding states of the elements present in these samples high energy-high resolution scans of the nitrogen region were performed.

2. XPS Analysis

After initial XPS analysis, the samples underwent the same treatment methods as the GaInNAs samples to ensure that the etching and depth profiling techniques were not influencing any peak

formation. A pure sample of GaInAs was etched, sputtered, and analyzed. The first measurement via XPS was a full survey of the entire binding energy range of the sample (Figure 3.1) A survey of the whole region allows us to identify the carbon (C 1s) peak to assign a proper work function offset which is essential during calibration.

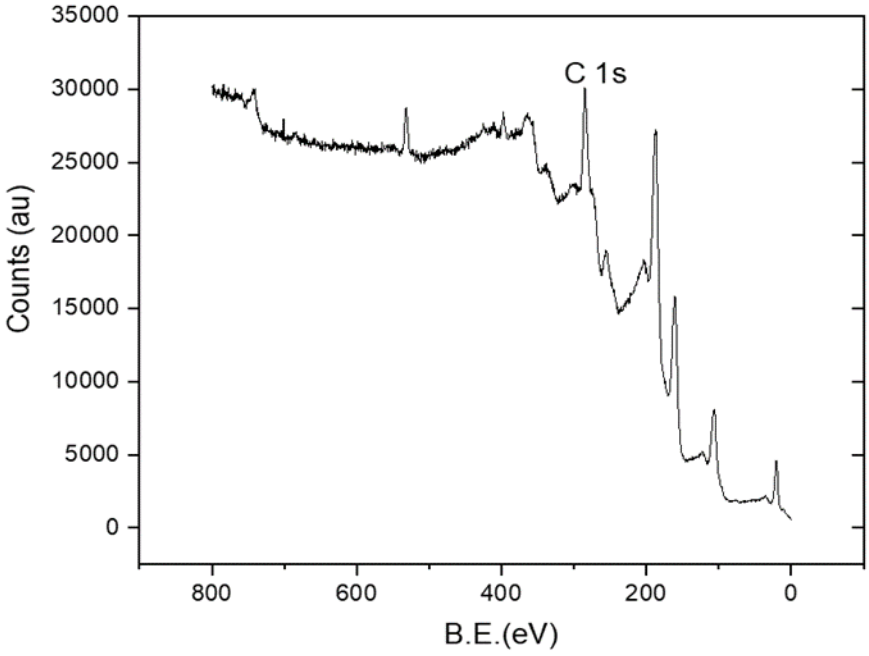

Figure 3.1. XPS survey spectra for GaInAs sample after hydrogenation and argon ion sputter

The high resolution XPS spectra for the nitrogen region show a minor peak in the form of Ga-N, however, the signal-to-noise is too high to get an accurate fit (Figure 3.2).

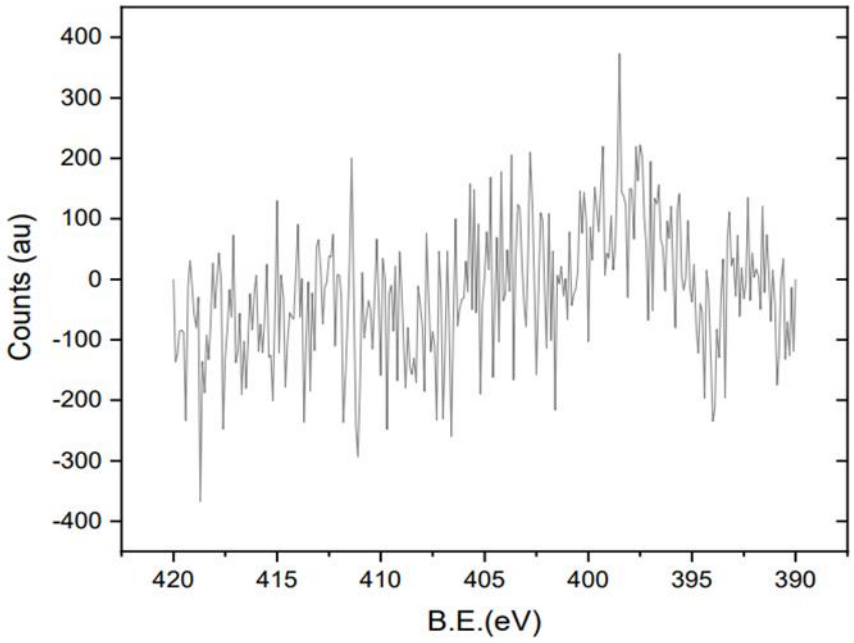

Figure 3.2. XPS spectrum for N associated region for GaInAs sample after hydrogenation and after argon ion sputter

In order to determine the influence of indium and arsenide with the binding configurations in the nitrogen associated region, a set of InAs materials was measured. The survey spectra for InAs after etching and sputtering are outlined in Figure 3.3 and the high-resolution nitrogen associated region is shown in Figure 3.4.

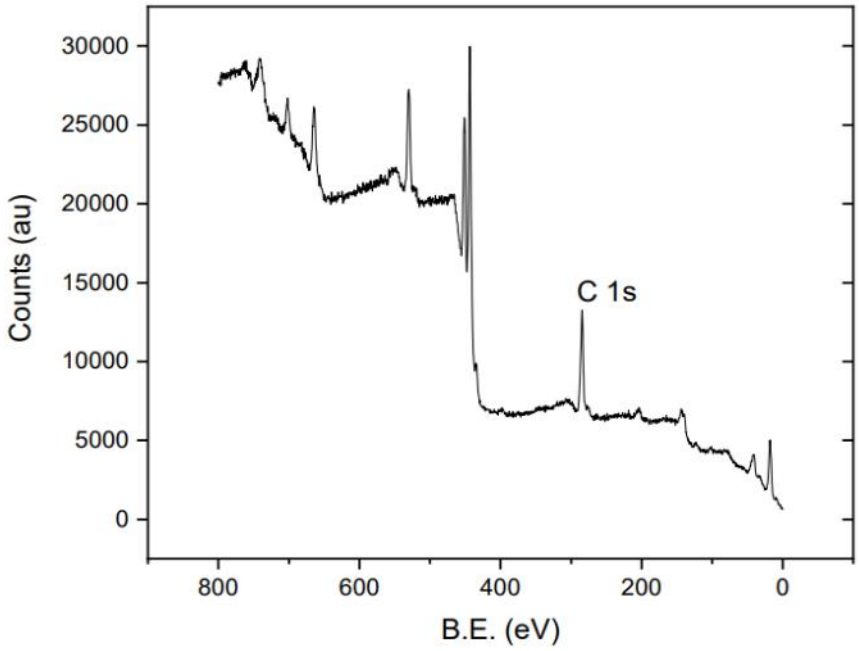

Figure 3.3. XPS survey spectra for InAs sample after hydrogenation and argon ion sputter

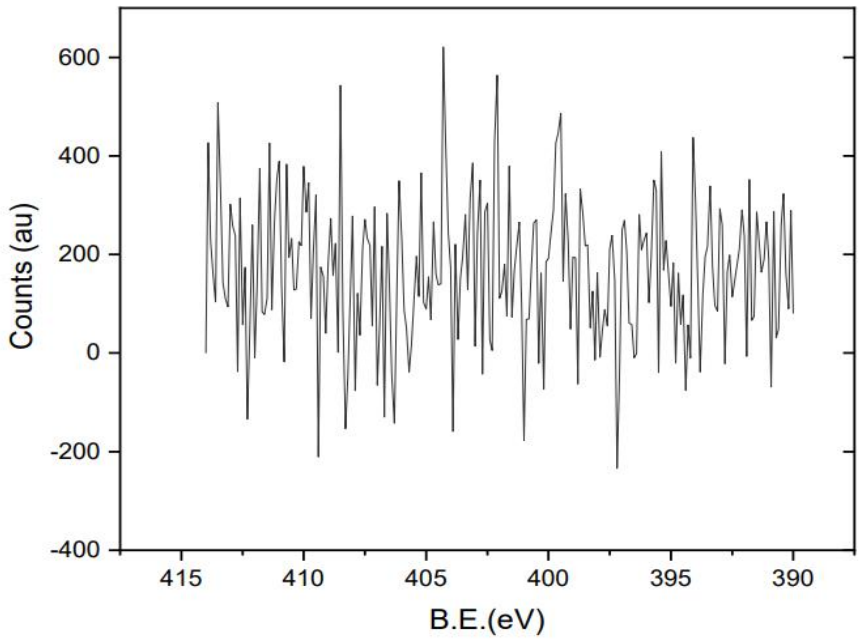

Figure 3.4. XPS spectrum for N associated region for InAs sample after hydrogenation and argon ion sputter

As expected, there is no peak formation in this region even after hydrogenation. Materials containing nitrogen contaminations would typically form a substitutional nitrogen peak (N 1s) located around 396-398 eV.

The survey (Figure 3.5) and high-resolution nitrogen associated region (Figure 3.6) for the GaP sample are shown below. After initial analysis, prior to hydrogenation, the nitrogen-associated region for this sample showed two very small peaks located at approximately 398 eV and 410 eV. However, after hydrogenation, these peaks were not present. The hydrogenation process has the ability to dislodge or react away any nitrogen contaminations that could have been on the surface of the sample originally.

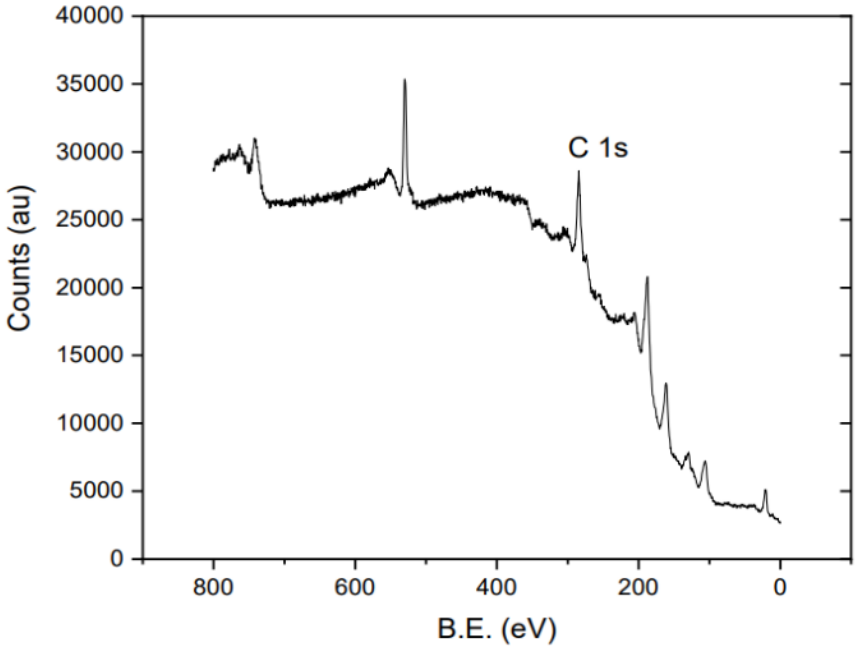

Figure 3.5. XPS survey spectrum for GaP sample after hydrogenation and argon ion sputter

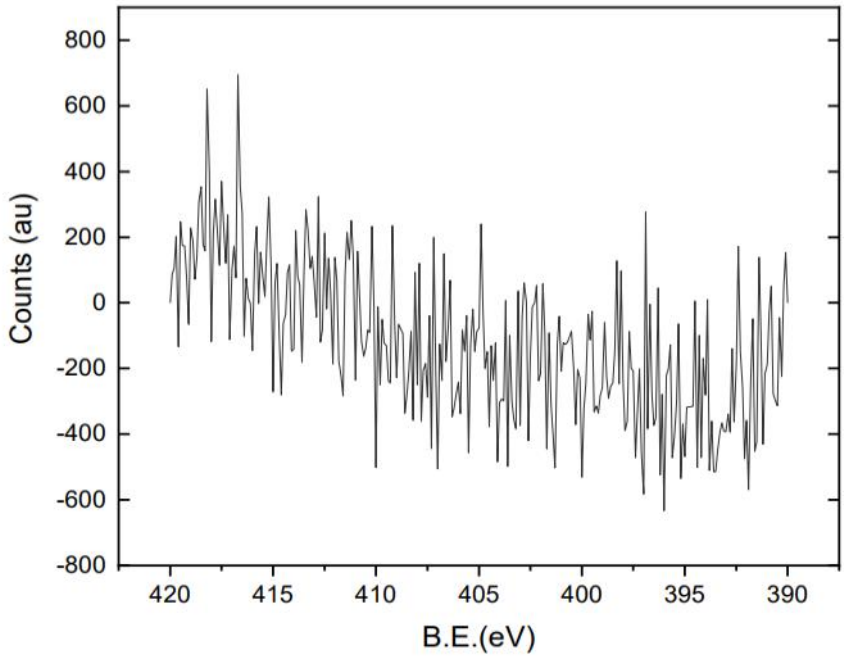

Figure 3.6. XPS spectrum for N associated region for GaP sample after hydrogenation and ion argon sputter

The measurement of these pure samples helps with peak identification of later samples and ensures that the spectrums are accurate and reproducible. The GaAs turned out to be more complicated than the other pure samples. While the survey spectra of this material (Figure 3.7) did not reveal any significant peaks the nitrogen-associated region the high-resolution N 1s scan turned out to be more complex.

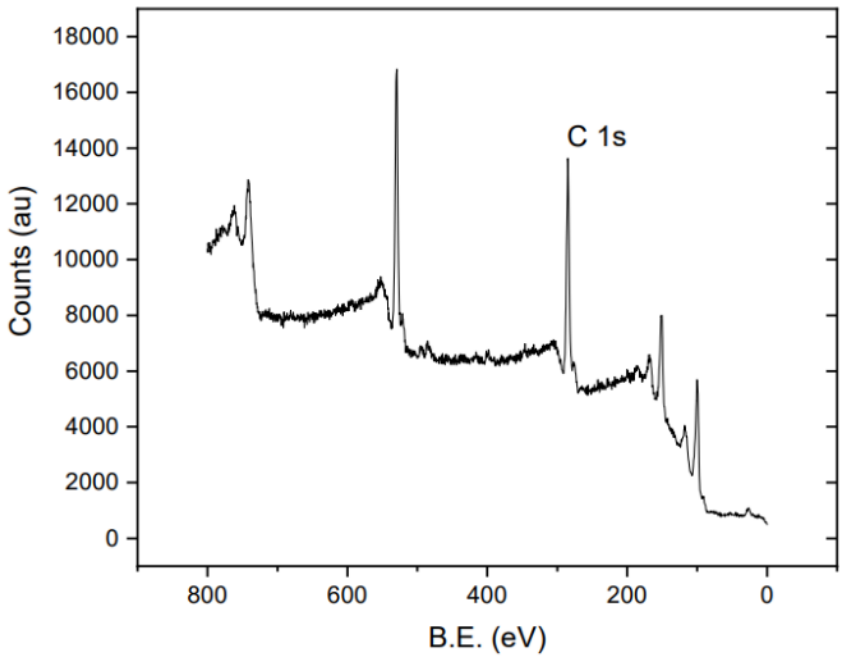

Figure 3.7. XPS survey spectrum for GaAs sample after argon ion sputter and hydrogenation

The high-resolution spectra show weak two peaks located at 398 eV and 410 eV even after hydrogenation and sputtering (Figure 3.8). Studying the nitrogen associated regions in these materials becomes important because, unlike the GaP sample where the peak is no longer present after hydrogenation the higher binding energy peak is still present in the GaAs material. We are now hydpothesizing that the nitrogen was traped in the mateiral during the growth process and not presented as a surface contaminent.

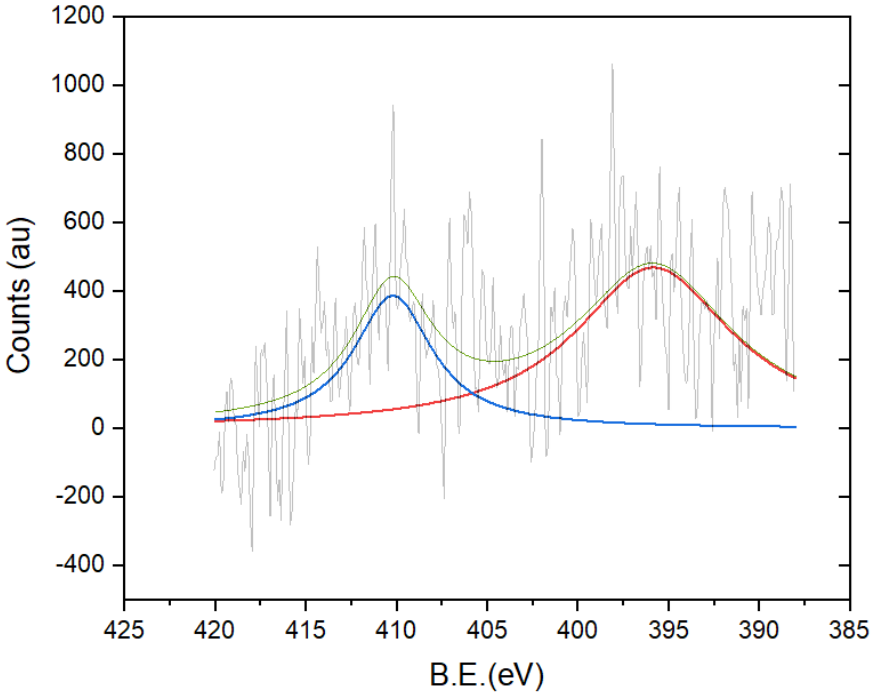

Figure 3.8. XPS spectrum for N associated region for GaAs sample after hydrogenation and after argon ion sputter

The peak located at 398 eV is consistent with the literature as the N1s peak with gallium binding to nitrogen in the lattice. [33] However, the weak peak located at 410 eV is not reported in the literature and remains unidentified. For example, Lay et al. investigated nitride semiconductors, which included InGaAsN, GaAsN, and InAsN. The samples were sputtered with argon and the XPS spectra were obtained, the nitrogen region showed the N 1s peak (N-Ga and In-Ga) located at 397-398 eV respectfully. However, the spectrums did not show any satellite features or peaks in the higher binding energy region.[34] To further investigate what type of elements were binding in the lattice to form the higher binding energy peak we obtained a pure GaN sample. This sample will help to independently identify the binding energies of nitrogen and gallium.

3. Gallium Nitride

The GaN samples were initially analyzed as is, and then were chemically etched, sputtered, and hydrogenated like the previous pure samples. The resulting spectra shows one broad peak at 398 eV (N 1s Ga-N) and a smaller peak located at approximately 410 eV (Figure 3.9). If the peak at 410 eV was caused by nitrogen on the surface it should disappear after sputtering with argon and hydrogenation as the GaP samples did. However, the peak is still present similarly to the GaAs samples.

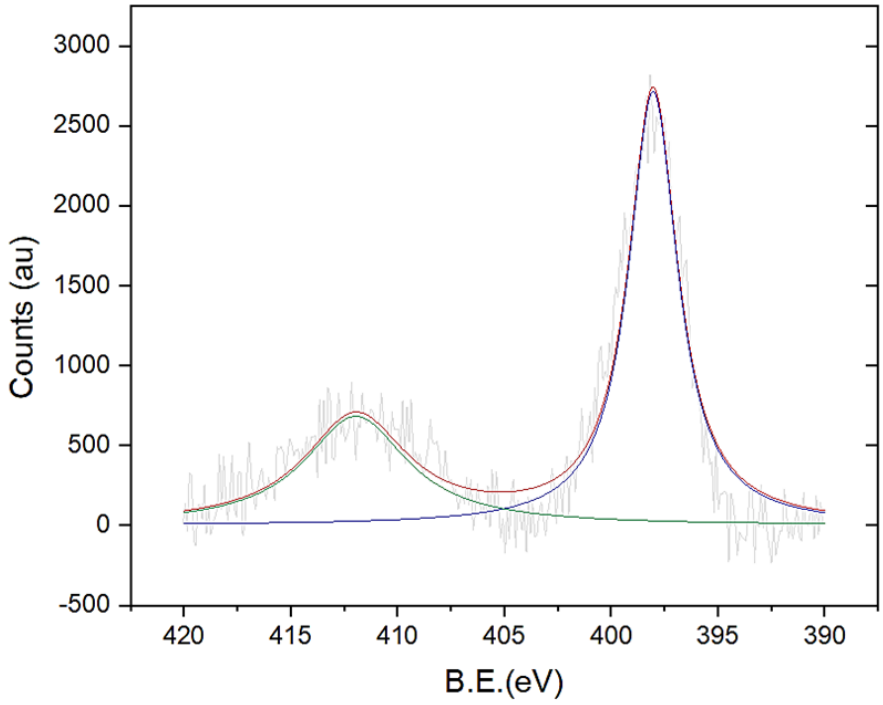

Figure 3.9. XPS spectrum for N associated region for GaN sample after hydrogenation and argon ion sputter

The peak located at 410 eV has not been report in the literature. However, a peak has been reported around 408 eV and is characterized as a nitrate compound with nitrogen atoms absorbed

on the oxide surface as well as nitrogen entry into the lattice.[35, 36] Bian et al. report an XPS spectrum for ZnO-based films where two peaks were observed in the nitrogen-associated region when the film is doped with nitrogen, at approximately 397.5 eV and 407.5 eV. It is also reported that in N-In codoped Zn-O films the peak at 397.5 eV is more pronounced and indicates the presence of an N-Zn bond. However, the peak at higher binding energy (407.5 eV) that corresponds to an N-O bond disappears with N-In co-doping. [37] Levtushenko et al. reports similar spectra for N-doped ZnO films and N-Al co-doped ZnO films, where two peaks are observed at approx. 398 eV and 408 eV.[38] The sputtering process should remove any surface oxygen from the samples, so the formation of an N-O bond is unlikely. It is reported in the literature that samples containing oxygen show no nitrate or nitride peaks after they have been sputtered with argon, the only peak that remains in the nitrogen-associated region of the N1s peak at approximately 396-398 eV.[39, 40] Previous research has also pointed out that there are two types of N species in titanium dioxide materials; one at the N1s peak position, but one that appears above 400 eV. This work was evaluated through electron pragmatic resonance spectroscopy measurements and density function theory (DFT) calculations. They attributed the nitrogen peak at 400 eV to interstitial nitrogen (which will be explored in section 4) bound to lattice oxygen. This puts the nitrogen in a positive oxidation state similar to that found in nitrite (NO_2^-) and nitrate (NO_3^-) species.[41]

3.1. Gallium Nitride Oxidation

To understand if this peak is influenced by oxygen, the chamber of the XPS instrument was filled with oxygen slightly above atmospheric pressure (10 psi). After oxidizing, the samples were analyzed with XPS and showed that not enough oxygen had been incorporated into the GaN wafer. A native oxide layer of approximately 5 Å is typically detected on as-grown Ga

terminated, (0001) GaN surfaces. To incorporate more oxygen, the sample was treated using a chemical etching solution and was then subjected to an oxygen-rich environment for various times and temperatures.[29-32, 42]Once the samples were treated, they were analyzed using XPS. The confirmation of oxidation is observed by an increase in the intensity of the O 1s peak (Figure 3.10), this represents the oxygen on the surface having a lower coordination number than the bulk oxides on the as-grown sample.

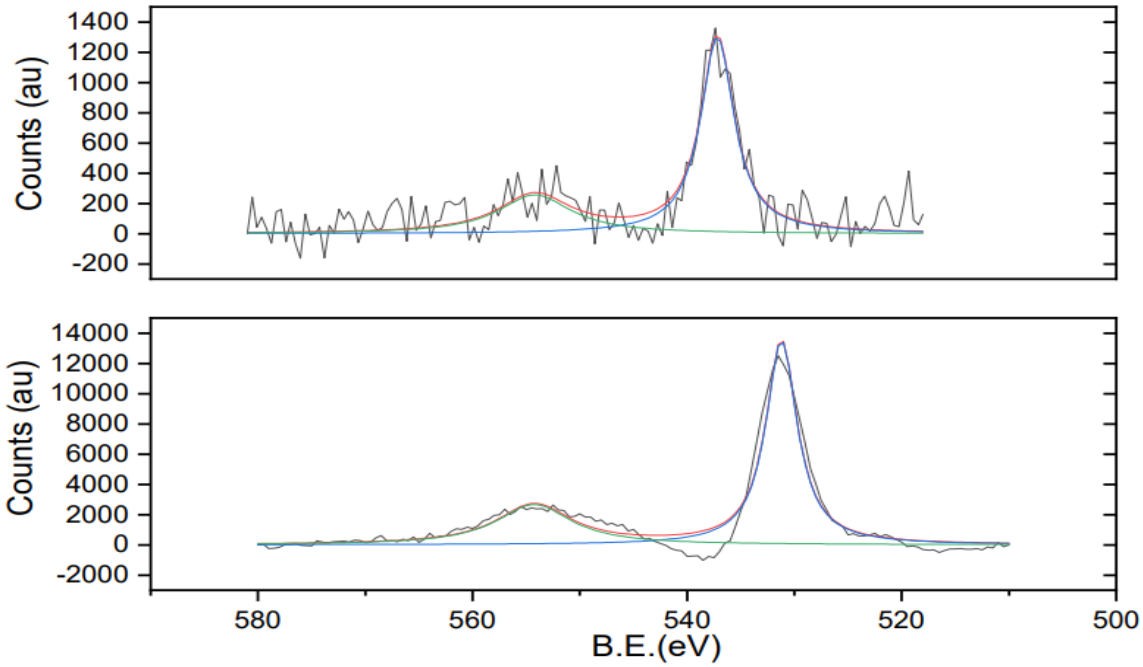

Figure 3.10. XPS spectrum for O 1s associated region for GaN sample untreated and after oxidation treatments

The spectrum for the samples that were oxidized (Figure 3.11) only revealed one weak peak in the nitrogen region that is associated with the N1s peak (GaN). There could be a very small undetectable peak at higher binding energies, however, if NOx was formed it should be a significant peak. Pal et al. reported that the lower energy N 1s peak became undetectable upon plasma oxidation of the GaN surface,[42] Indicating that a GaO film forms and the nitrogen is

eliminated. Watkins et al. report no real changes in the N 1s peak in GaN upon oxidation representing no surface NO_x formation.[43] These results are consistent with what is observed in the GaN sample.

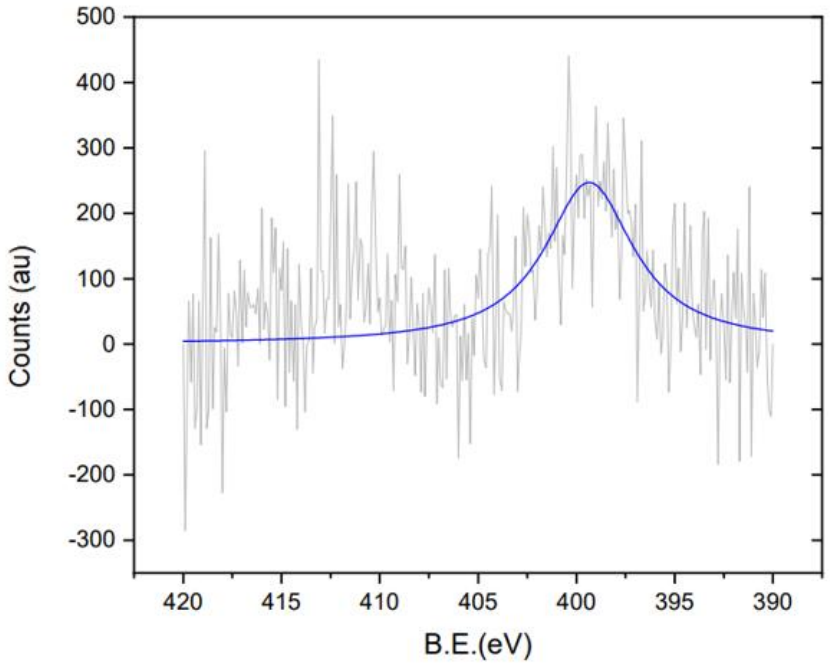

Figure 3.11. XPS spectrum for N associated region for GaN sample after chemical and dry oxidation treatment

There is also concern that the peroxide/citric acid etch, used to remove the protective overlayer on the InGaNAs samples (chapter II), could have oxidized the surface and formed the higher binding energy peak. Thus, the same etching method was used on the GaN wafer. The XPS spectra were obtained after the GaN was soaked in the peroxide etching solution. The spectra reveals only one nitrogen peak identified as the N 1s peak at 398 eV (Figure 3.12). Chemical reactions during the

peroxide etching solution did not cause the formation of the higher binding energy peak observed in the GaInNAs samples.

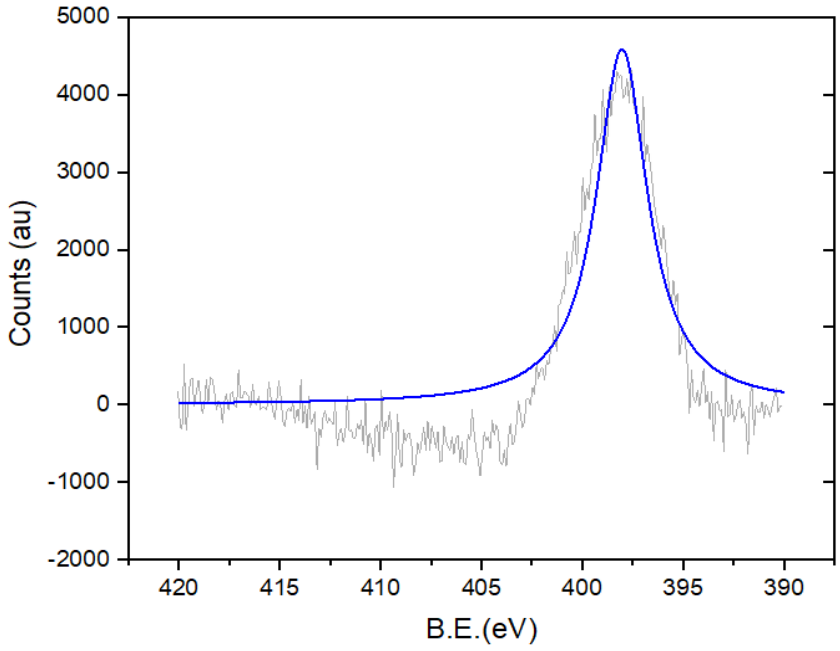

Figure 3.12. XPS spectrum for N associated region for GaN sample after HCl cleaning and H_2O_2 etch

After evaluating the influence of oxygen on the nitrogen associated region, we have concluded that nitrooxy peaks are not seen in these samples. We oxidized the surface using various methods and this was confirmed through the increase in intensity of the O1s peak. Once the samples were completely oxidized, we see the higher binding energy peak disappear from the spectra. Further investigation into this unknown peak will be explored in the next section by means of nitrogen ion sputtering.

4. Nitrogen Ion Sputtering

To determine the effects of nitrogen had on these samples, particularly the higher B.E. peak, we introduced N_2 into the lattice of the pure samples (InGaAs, GaAs, InAs). There are three main methods for the introduction of nitrogen to these materials: thermal nitridation, plasma nitridation, and N_2 bombardment. As InAs and InGaAs samples did not show any nitrogen features in the binding energy region of 390 eV-420 eV, any nitrogen observed should be associated with nitrogen implantation . Since the GaAs sample showed two low-intensity peaks in this region, the addition of more nitrogen into the sample should significantly increase the intensity of these two peaks.

Typically, an inert gas is used to sputter samples to prevent reactivity on the surface or atomic mixing within the lattice. In traditional sputtering techniques with xenon or argon, ion implantation is one of the drawbacks that causes sample modification. However, in order to introduce sufficient amounts of nitrogen into the sample to evaluate the higher energy peak formation, N_2^+ implantation will be used. Nitrogen ion bombardment is an easy way to introduce reactive nitrogen into the lattice at low temperatures.

Ion bombardment has been previously used to modify the microstructure and improve the hardness and density of thin films. The implantation of nitrogen has also been studied for use in semiconductors to form buried insulating and barrier layers. Nitrogen implantation at room temperature can led to the formation of metal nitrides.[44, 45] Previous research has reported the effects of low-energy N_2 beam bombardment on InAs, InSb, and InP materials using *in-situ* XPS and the formation of nitride surface layers and interstitial nitrogen. The recombination of molecular nitrogen can also take place, which is more likely in compounds that offer more space for the N_2 on the interstitial lattice sites. [46]

Using the sputtering process described in (Chapter II) , the films were bombarded with high-energy N_2 ions where the energy of the incoming gas is a function of the applied substrate bias voltage.[47] Figure 3.13 shows nitrogen ion bombardment and implantation into the lattice. To reduce the effects of nitrogen thin film deposition with this technique the amount of N_2 was carefully controlled through the amount of voltage applied to the sputter gun (about 4 keV).

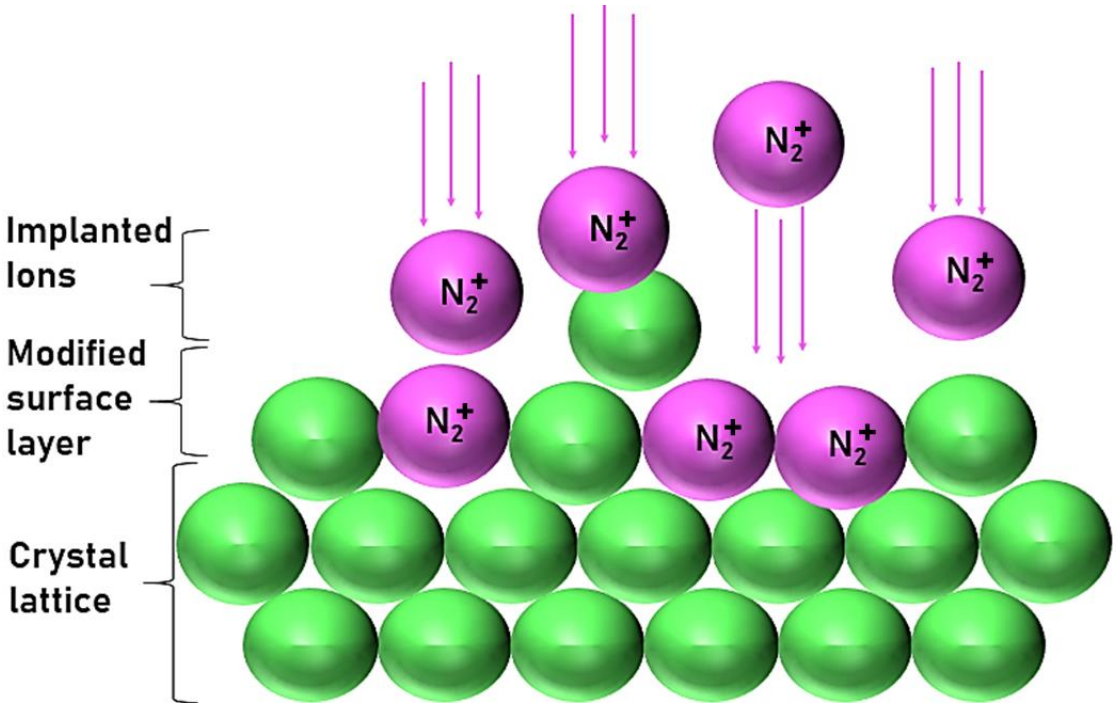

Figure 3.13. Diagram of nitrogen ion implantation into the crystal lattice

Once the samples were sputtering with sufficient amounts of nitrogen, they were transferred back into the XPS chamber for analysis. The high-resolution spectra for the nitrogen associated region for InAs before and after nitrogen implantation is shown below (Figure 3.14)

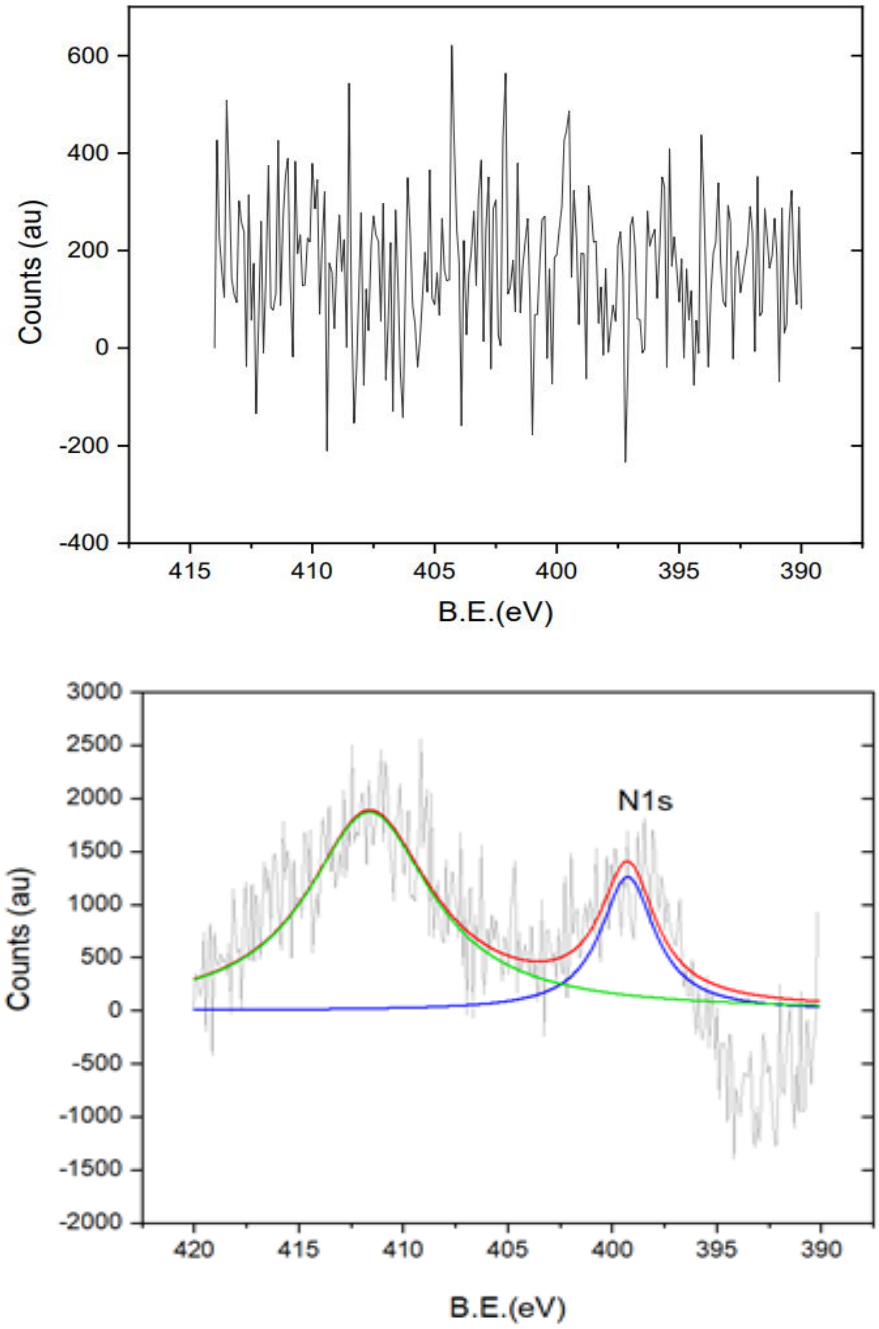

Figure 3.14. XPS spectra of nitrogen associated region for InAs before (top) and after (bottom) nitrogen sputtering

A shown in the spectra there is a clear increase in the N1s peak at (398 eV) and the peak at higher binding energy indicating that a significant amount of nitrogen has been incorporated into the InAs lattice. The XPS spectra for InGaAs before and after nitrogen implantation is shown below.

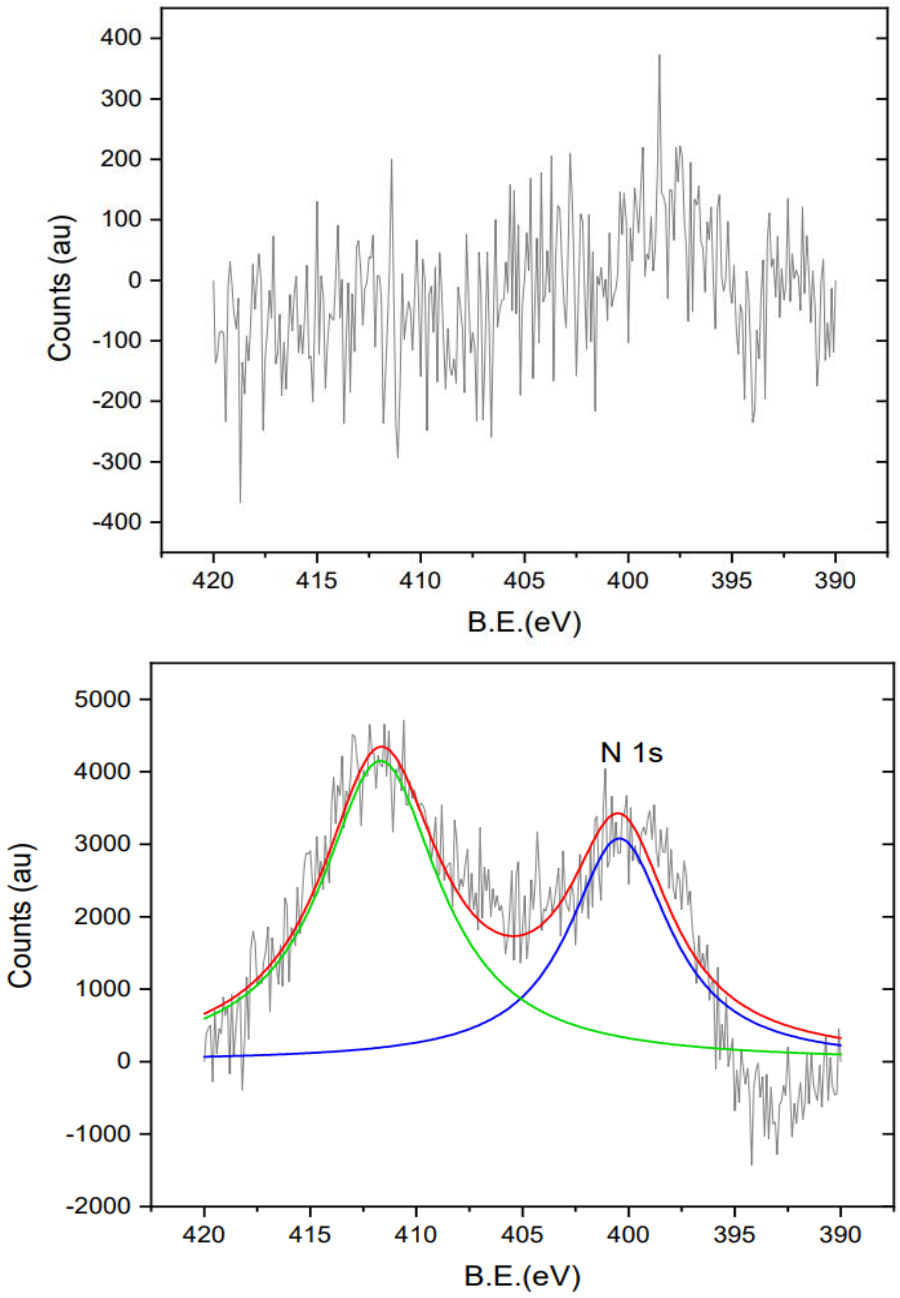

Figure 3.15. XPS spectra of nitrogen associated region for InGaAs before (top) and after (bottom) nitrogen sputtering

The spectra for the InGaAs sample confirmed nitrogen implantation by the formation of a clear N 1s peak and the unknown peak at higher binding energy. Previous measurements of GaAs samples show two low-intensity peaks in the nitrogen associated region. In order to understand if adding more nitrogen increase an already existing peak, the sample underwent the sample nitrogen ion implantation method. The spectra for before and after nitrogen ion sputtering is shown below (Figure 3.16).

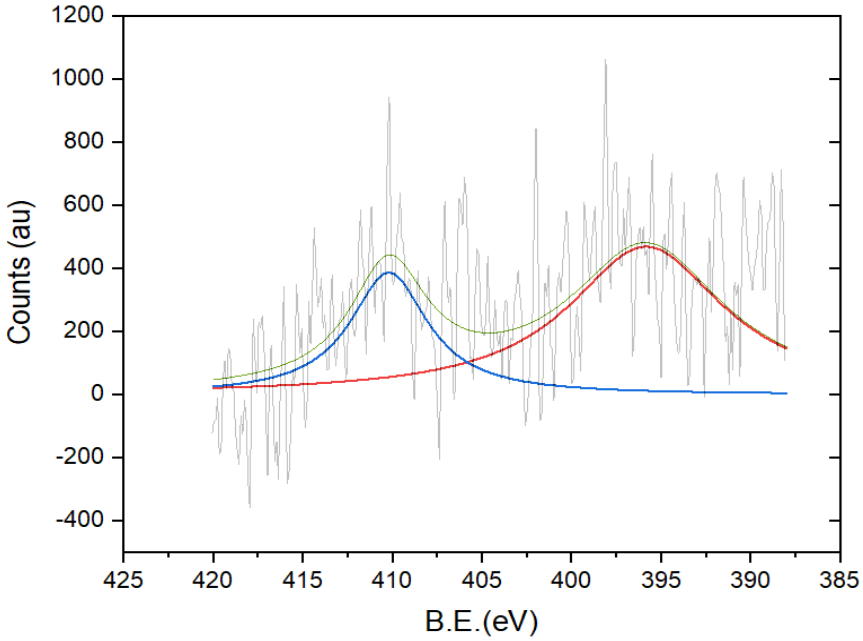

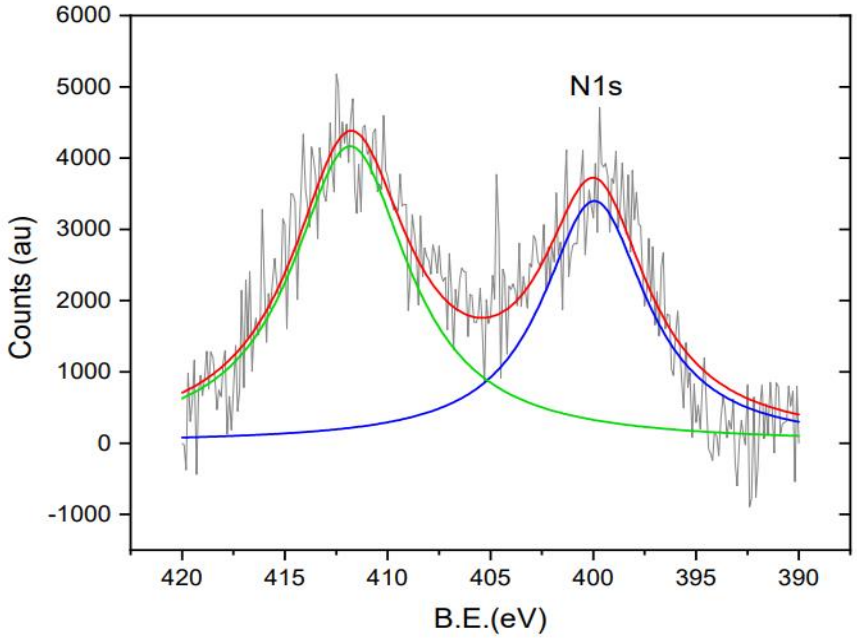

Figure 3.16. XPS spectra of nitrogen associated region for GaAs before and after nitrogen sputtering

5. Conclusion

The peak locations in the nitrogen associated region were consistent throughout the samples and various surface treatments showed similar modifications to the surface. Chemical etching had no effect on the N 1s region nor did oxidation. During the nitrogen implantation experiment alterations in the higher binding energy peak are finally observed. A clear indication of implantation is observed in the GaAs, InAs, and InGaAs, in which the peak at 410 eV intensity is significantly magnified.

Nitrogen is small enough to fit in between normal crystalline lattice locations or it can replace the cation to form substitutional nitrogen.[48] The N 1s peak around 398 eV is consistent with substitutional nitrogen most commonly in the form of GaN or InN. The higher binding energy peak (410 eV) is occasionally seen in the literature but is not identified. When reported, this peak is either ignored or associated with surface N-O bonds. Another issue can arise with the

appearance of Auger lines, which can obscure this region of the spectra. These lines are only observed when using the more traditional aluminum anode. For our measurements the magnesium anode was purposefully selected to avoid these peaks.

With nitrogen ion sputtering, this higher energy peak can be seen with greater intensity than the N 1s substitutional nitrogen. This observation indicates that the nitrogen implantation is causing this peak formation. The peak locations for the samples that received nitrogen ion implantation remained the same with respect to binding energy as well as the area and FWHM.

Although the binding energy of this unknown peak was much closer to the range of nitrites and nitrates instead of nitrides, further oxidation of the sample did not increase this peak. Therefore, this peak can be assigned to interstitial nitrogen. The significance of this peak is discussed in the next chapter.

CHAPTER IV

XPS STUDY OF MULTI-JUNCTION SOLAR CELLS

1. Introduction

A development in new renewable energy technologies has become increasingly more important in the last 10 years. Improving the conversion efficiencies of these new technologies is crucial in making them competitive with conventional sources of energy. Commercially available solar panels are commonly comprised of single-junction solar cells, typically using silicon as a semiconductor with efficiencies around 32%.[49] The method used today that is the closest to practical implantation for harnessing the full solar spectrum and improving efficiencies is through the application of multi-junction solar cells. The Multi-junction solar cells have been of recent interest due to their ability to achieve efficiencies as high as 50% .[50] These multi-junction devices use a high-bandgap cell to absorb high-energy photons while a slightly lower bandgap material is below to absorb photons with longer wavelengths. Materials such as gallium indium phosphide (GaInP) and indium gallium arsenide (InGaAs) create multiple layers that all respond to various wavelengths of solar irradiation. These systems are typically used in space applications such as satellites and spacecrafts because of the ability of each cell to absorb different regions of the solar spectrum.

In these materials, the incorporation of small amounts of nitrogen in the lattice can cause material quality problems during the growth process with the formation of Ga-N_4 and Ga-In-N_3 defects. [21] These create nonradiative centers and decrease homogeneity that results in lower efficiencies. To passivate these defects rapid thermal annealing (RTA) in a nitrogen-rich environment is shown to facilitate the rearrangement of the unfavorable Ga-N configuration to In-N. [51, 52] An alternative method of hydrogenation has also been studied as a method of reducing nitrogen-based defects in dilute nitride materials and form strong N-H bonds. [53, 54]

2. XPS Analysis of Thermal Annealing Defect Passivation

The initially received GaInNAs samples were hydrogenated and rapidly thermally annealed at 850°,600°, 300°, and one as grown. The samples were placed in the XPS chamber and were left overnight so the pressure could reduce to 1.5 x 10^{-9} torr. The carbon C 1s peak (284.5 eV) was used as a reference to properly align the binding energy scale of the spectra and assign an appropriate work function offset. The GaAs capping layer interfered with initial analysis of the sample, so it was originally etched with an ammonia solution. This treatment chemically reacted with the first junction (GaInNAs layer) forming contaminations and causing interference with the XPS spectra. [26]An acid-based etchant (hydrogen peroxide/citric acid) solution was then applied to fresh samples to remove the capping layer without interfering with the materials below.[27] Experiments on GaN (Chapter III) showed that this etching solution did not affect the N1s peak and did not influence the formation of additional peaks. Etching time and solution etchant concentrations were selected based on the etch rate, so that the capping layer was only removed.

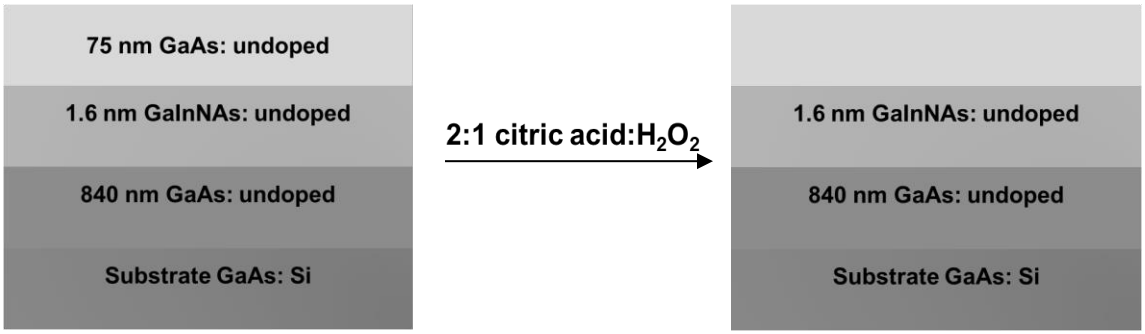

Figure 4.1. GaInNAs samples before and after citric acid/peroxide chemical etching

Once the capping layer was properly removed the samples were analyzed with XPS using an aluminum and magnesium anode. Both anodes were required to span the binding energy range of the peaks and to shift the X-ray-dependent emission of Auger electrons. The indium-related binding region (460 eV-430 eV) shows that one of the indium 3 $d_{5/2}$ peaks is predominantly binding to nitrogen in the lattice and is located at approximately 444.5 eV (Figure 4.2), which is near the InN reference Auger parameter point.[57, 58] The splitting causes a second peak (3 $d_{3/2}$) peak located at 452 eV, the difference in energy between these two peaks is 7.5 eV which is consistent with the literature for semiconductors. The indium 3 $d_{5/2}$ and 3 $d_{3/2}$ peaks (with intensity ratio 3:2) remained constant for the samples that were annealed at different temperatures and were used alongside the carbon C1s peak as a reference.

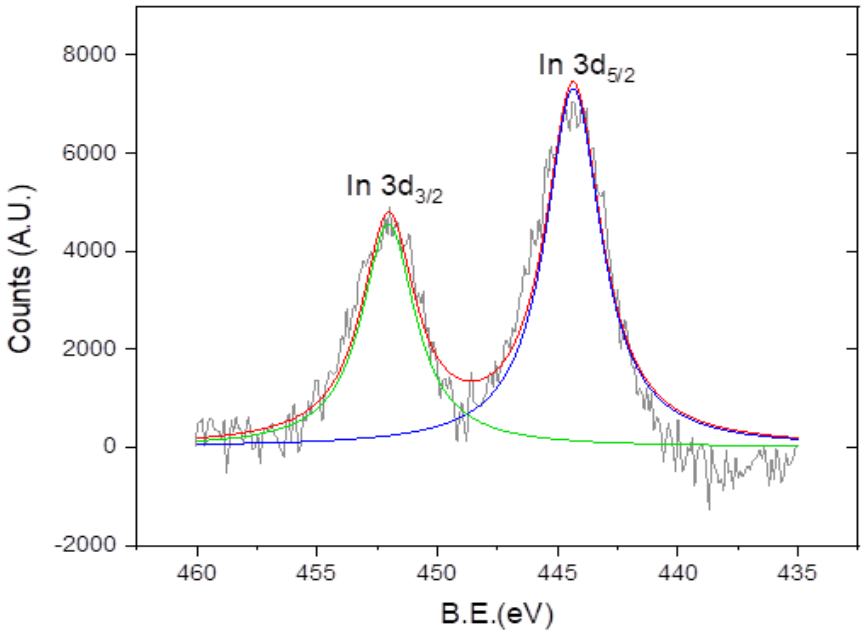

Figure 4.2. XPS spectrum for Indium associated region for GaInNAs sample at 300° C RTA

The indium ($3d_{3/2}$) peak is an occurrence from spin-orbit splitting (*j-j* coupling), all orbitals (except s) give rise to a doublet with the two states having different binding energies. These peaks have specific area ratios based on the degeneracy of each spin combination, which assists in elemental identification. The arsenic ($3d_{5/2}$) peak at approximately 41 eV (Figure 4.3) was constant throughout all samples. The gallium ($3p_{3/2}$) peak at approximately 104 eV was also constant throughout all of the samples.[59]

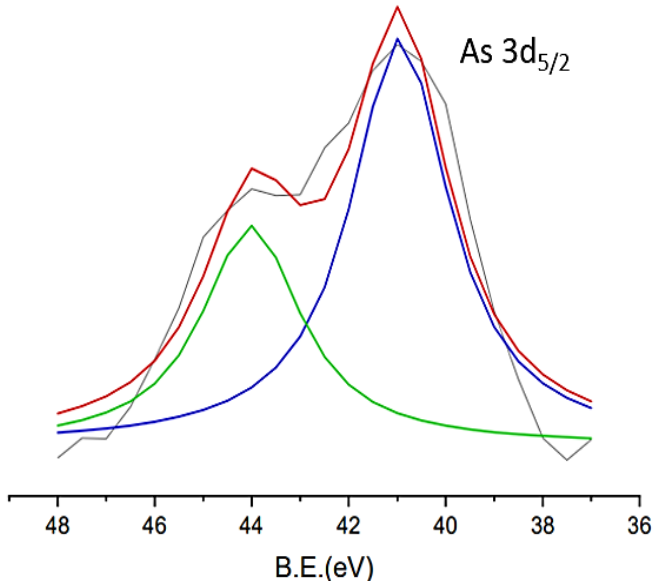

Figure 4.3. XPS spectrum for As $3d_{5/2}$ associated region average for as grown, 300 °C, 600 °C, 800 °C RTA GaInAs samples.

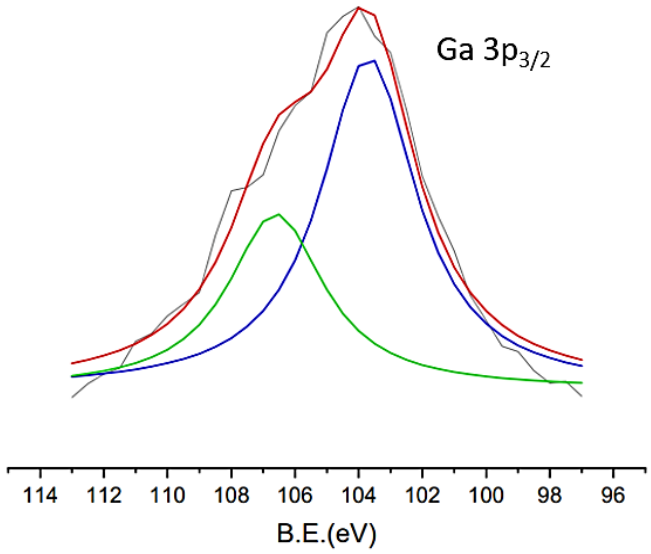

Figure 4.4. XPS spectrum for As $3d_{5/2}$ associated region average for as grown, 300°, 600°, 800° RTA GaInNAs samples.

The primary reason for characterizing these GaInNAs solar cells with XPS was to identify if RTA in a nitrogen-rich environment and hydrogenation facilitated the rearrangement of the nearest neighbors from Ga-N to the more favorable In-N configuration, so the nitrogen binding associated region (420 eV-385 eV) was extensively studied. A representative spectrum was selected to show this region. The preliminary analysis of the XPS spectra revealed three peaks in this region (Figure 5.5).

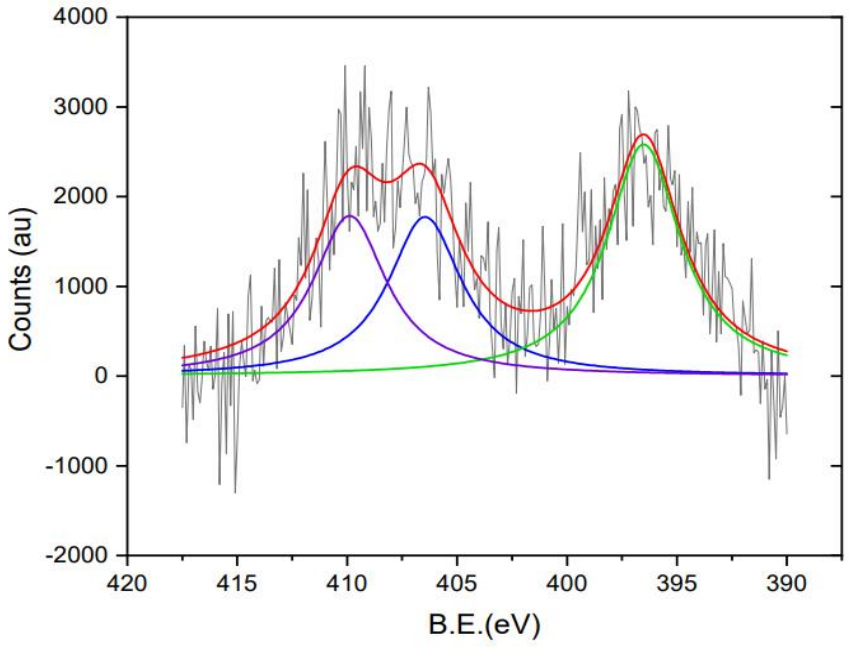

Figure 4.5. XPS spectrum for N associated region for GaInNAs sample RTA at 300° C.

The peaks were analyzed using XPSPeak fit, a peak-fitting software designed for XPS. A linear background was subtracted, and the peaks were fit using a Gaussian-Lorentzian function. The most prominent peak, which is constant throughout the samples annealed at different temperatures was thought to be centered around 396 eV. This peak is typically regarded as the N 1s peak and is the substitutional nitrogen form of indium nitride.[60-63] The possible N 1s binding

species and their corresponding energies are relatively close. Thus, multiple fittings were attempted using the following binding energies:

Table 4.1. N 1s species and corresponding binding energies

N 1s Species	Binding Energy (eV)	Ref.
Ga-N	398	38-40
In-N	396	34-37
As-N	394	39

After further investigation of the remaining samples, an error in the energy scale was discovered. Using the indium $3d_{5/2}$ reference peak, the work function was adjusted properly. Accurate spectra were then collected, which shifted the N 1s peak to a slightly higher binding energy (Figure 4.6). This peak is now in agreeance with the Ga-N configuration at approximately 398 eV.[34, 64, 65]

Identifying all the peaks in the nitrogen-associated region of the spectrum was especially challenging due to the unidentified peaks located at higher binding energy. The literature does not classify any material or chemical states associated with these locations on the spectra.

3. XPS Analysis of Hydrogenation Defect Passivation

Hydrogenation removes the local electronic effects of nitrogen by shielding the atom with protons. To understand if hydrogenation passivated the nitrogen-related defects and initiated the formation of the In-N configuration, we obtained GaInNAs samples that removed this step and compared the two. The same etching procedure was applied to these new samples, and they were analyzed with XPS. As expected, there was no change in the indium, gallium, arsenic, and carbon

region of the spectra. The spectra for the nitrogen associated region (Figure 4.6) showed more defined peak formation following hydrogenation.

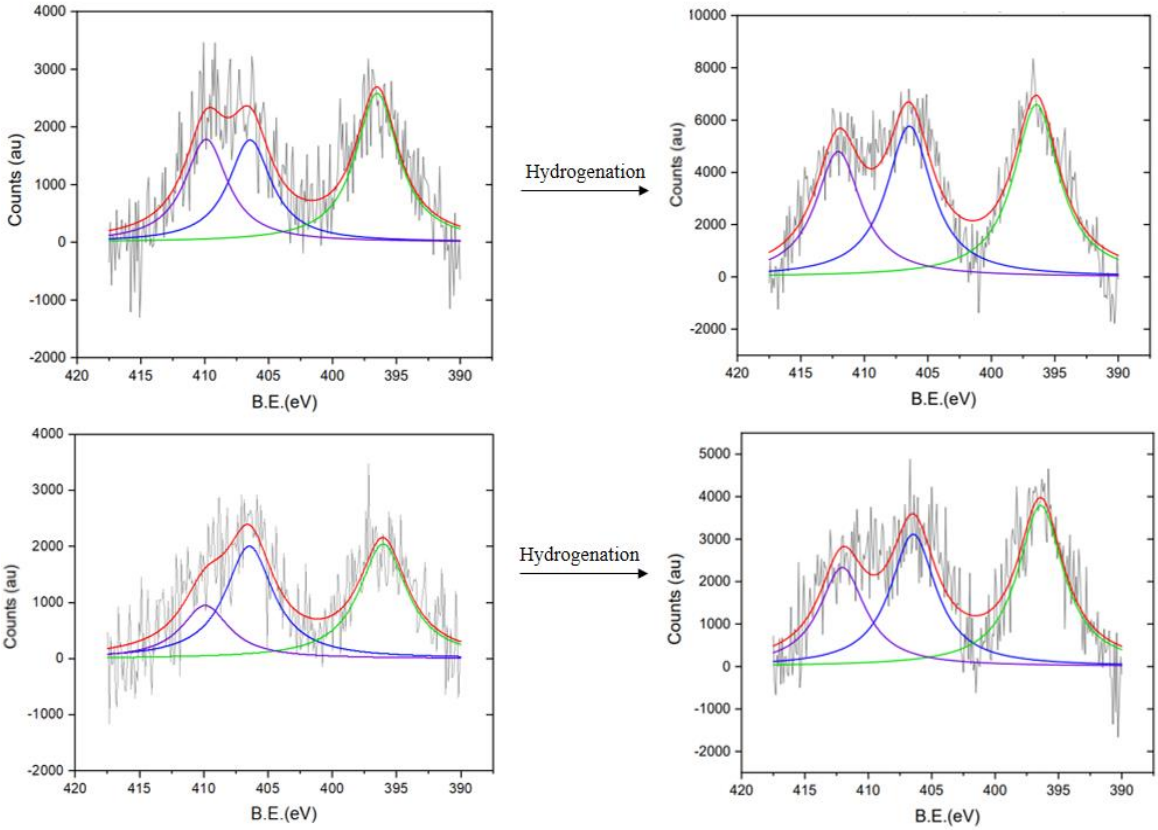

Figure 4.6. XPS spectrum for N associated region for GaInNAs sample RTA at 300 ° C (top) and 600 ° C (bottom) before (left) after hydrogenation (right)

The nitrogen region reveals the same N 1s (GaN) peak at 398 eV, however, the two peaks at higher binding energy become more defined after hydrogenation treatment. Despite changing the intensity of the peaks, no shifts in binding energy were seen for the N 1s peak which indicates that nitrogen is still binding to gallium in the lattice. The peak located at 408 eV (middle peak) also remains in the same location throughout the samples. However, the highest binding energy peak (410 eV) shifts slightly higher (412 eV) after hydrogenation. The samples annealed at the

highest temperature (850° C) showed the greatest increase in intensity and peak formation after hydrogenation shown in Figure 4.7.

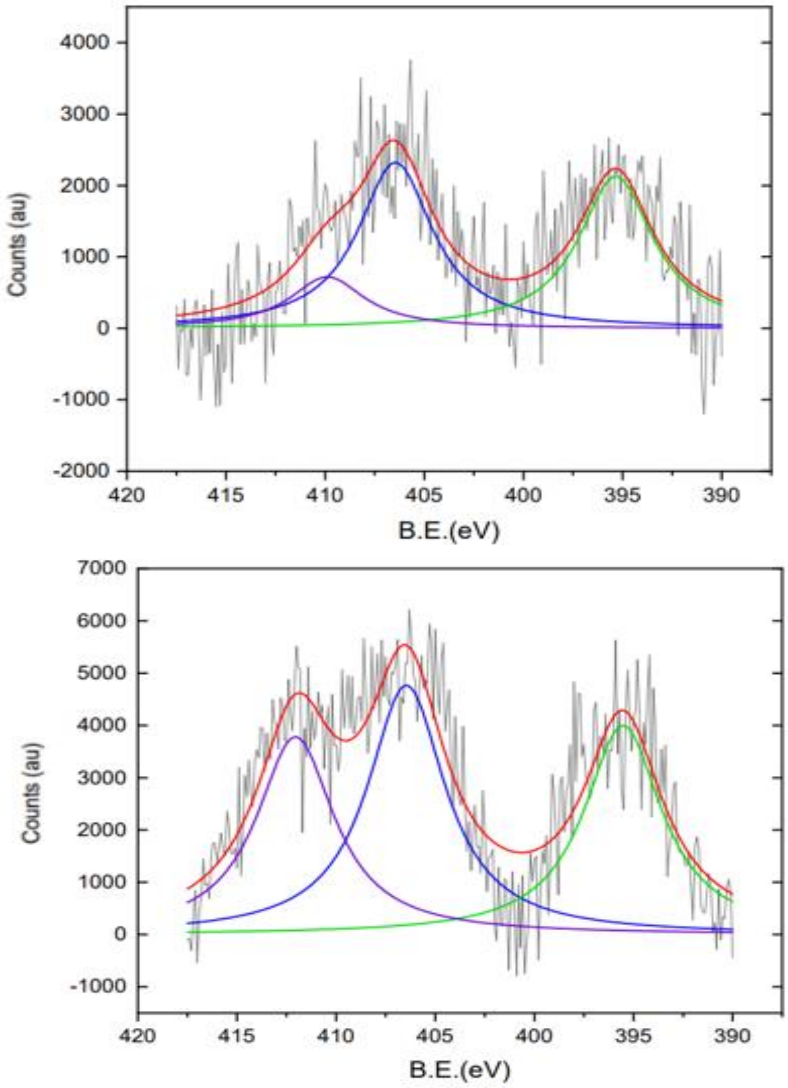

Figure 4.7. XPS spectrum for N associated region for GaInNAs sample RTA at 850° C before (top) and after hydrogenation (bottom).

To ensure the etching solution did not react with the surface and influence the formation of these higher binding energy peaks, the samples that underwent hydrogenation were sputtered *in-situ* with low-energy argon ions. This is to confirm there was not contamination remaining on the

surface before analysis. The samples were sputtered at 2 keV in a raster 9 mm x 9 mm for 20 minutes at a base pressure of $5x10^{-7}$. This process removes several nm from the surface. Once the samples were sputtered, they were analyzed with XPS again (Figure 4.8). The peak that was located at the highest binding energy (412 eV) has now disappeared and the peak that was located at 408 eV shifted slightly higher to 410 eV. The N 1s (GaN) peak remained unchanged. This remains true for all samples that were annealed at various temperatures.

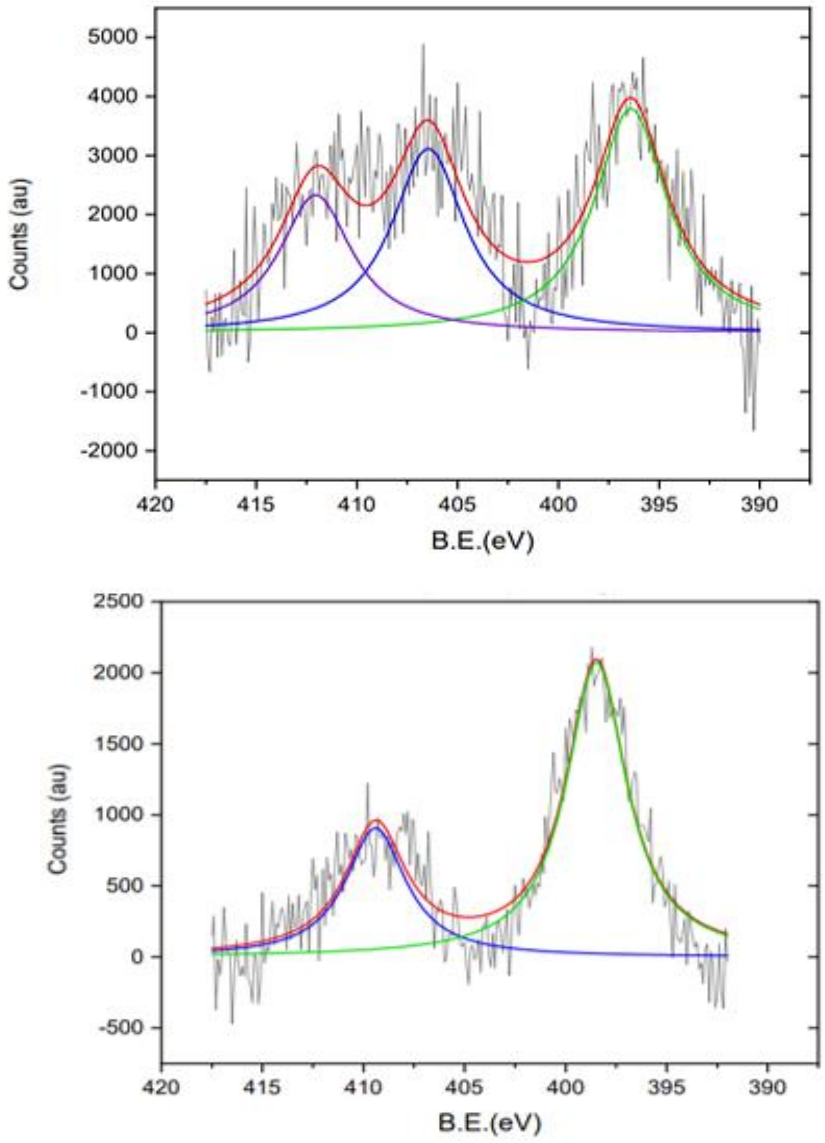

Figure 4.8. XPS spectrum for N associated region for GaInNAs sample RTA at 600° C before (top) and after (bottom) sputtering

Due to the fact that the higher binding energy peak was still present, the samples were sputtered once more to ensure any additional surface contaminations were removed and to etch further into the junction layer. This caused a slight decrease in peak intensities, but the peaks remained at the same binding energies. The highest B.E. peak is thought to be a contamination introduced during the chemical etching process; this peak is removed after argon sputtering.

The relative concentrations of the nitrogen peak to the indium peak were calculated for the samples after argon sputtering at different RTA temperatures. Using the intensity and sensitivity factors of the N 1s peak and the In $3d_{5/2}$ reference peak the relative concentrations were plotted in Figure 4.9.

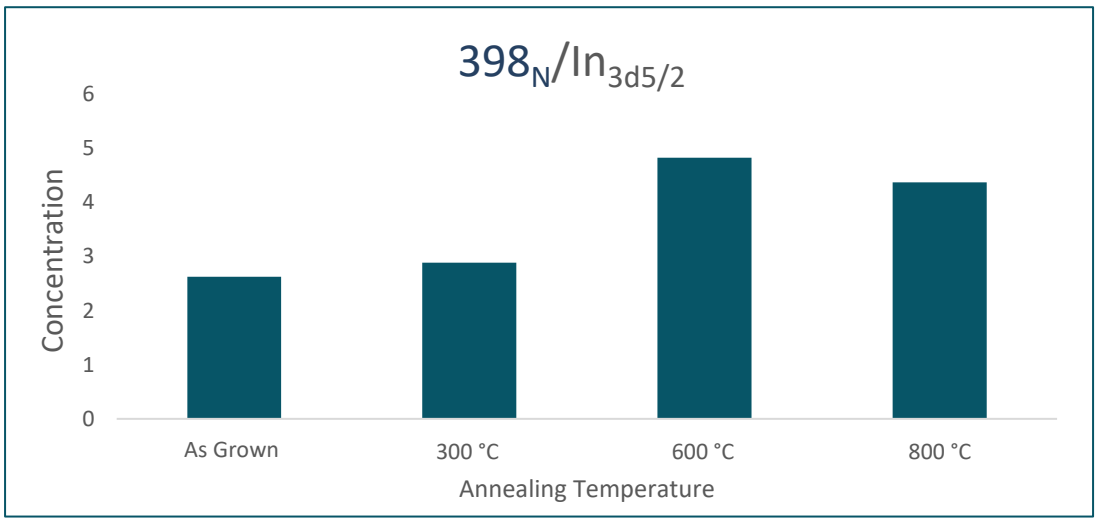

Figure 4.9. Graph of relative concentrations of N 1s (398 eV)/ In$3d_{5/2}$

The relative concentrations can be calculated using equation IV-1, where *I* is the intensity of the peak and *S* is the sensitivity factor determined by the spectrometer

$$\frac{n_1}{n_2} = \frac{I_1/S_1}{I_2/S_2}$$ [Equation IV-1]

The sensitivity factor is used to scale the measured peak areas so that discrepancies in the peak areas are representative of the amount of material in the sample. An elemental library from Physical Science Instruments was used for this determination. From the plot, there appears to be a trend with an increase in RTA temperatures and N concentrations. This could be facilitating the formation of more substitutional nitrogen in the lattice. The samples annealed at 600°C show the highest concentrations of nitrogen, it has been reported that the thermodynamic solubility of N in bulk GaAs is at about 650 ° C.[66] This could account for the highest relative concentration of nitrogen for the samples that were rapidly annealed in a nitrogen rich environment around this temperature. Higher annealing temperatures appear to help facilitate the formation of the favorable In-N configuration, as seen by an increase in the N/In concentrations.

The relative concentrations were also determined for the higher binding energy peak after sputtering at different RTA temperatures. The same indium $3d_{5/2}$ peak intensity was used along with the intensities for the peak located at 410 eV.

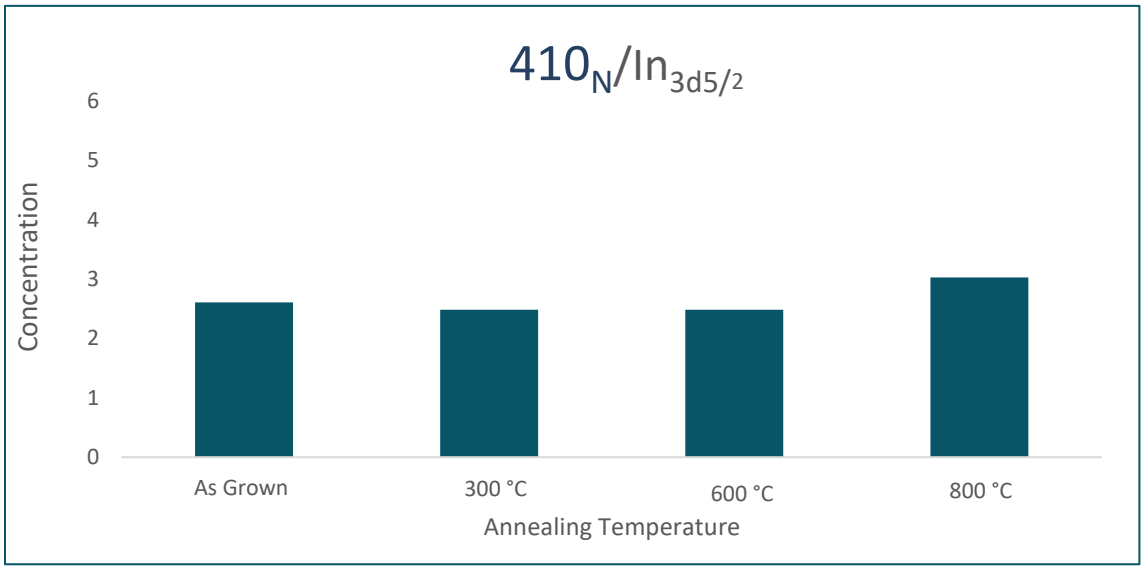

Figure 4.10. Graph of relative concentrations of higher binding energy peak (410eV) / $In3d_{5/2}$

From the plot, we can see that the RTA annealing temperature did not impact the relative concentration of nitrogen in this peak. This is in agreeance with our hypothesis from the set of pure samples, that this peak is formed by interstitial nitrogen. If this peak was a form of substitutable nitrogen, then RTA should have altered the concentrations as we observed with the N 1s (398 eV) peak.

5. Conclusion

A better understanding of the nitrogen associated region was acquired through the nitrogen implantation. The exploration of the InAs, GaAs, and InGaAs samples and N_2 bombardment we were able to identify the higher biding energy peak at 410 eV. This peak was formed as a result of interstitial nitrogen. Previous work suggests that a majority of nitrogen atoms added to these materials would be expected to go to the isoelectronic substitutional indium or gallium sites.[67] Interstitial nitrogen could form in high concentrations under non-equilibrium conditions during

the molecular beam epitaxy growth process. Bösker *et al* [68] showed that nitrogen diffuses in the GaAs lattice by a kick-out mechanism involving interstitial nitrogen.

The location of this peak on the binding energy scale indicates interstitial nitrogen. The N 1s peak is located at a slightly lower B.E. due to the -3 charge on the nitrogen in GaN, so less energy is required to eject this core electron. The addition of valance electrons can decrease the binding energy by increasing the screening of the nucleus. However, a chemical shift is observed with the interstitial nitrogen due to the higher oxidation state which increases the coulombic interaction between the ejected electron and the nucleus. This shift is observed in the binding energy scale with the interstitial nitrogen at a higher binding energy (410 eV).

Typically, interstitial nitrogen incorporation was dramatically reduced when the samples were annealed at high temperatures. Annealing atoms were dissociated in the crystal structure and a reduction in interstitial sites were observed. From the relative concentration determination for this higher binding energy peak, we did not observe a relationship between annealing temperatures and nitrogen concentration. The efficiency of these materials goes down at high temperatures, and from Figure IV-9 we can see that the samples annealed at 650° C forms the most favorable In-N bonds. This is because the solubility of N into bulk GaAs is around this temperature.

Interstitial nitrogen has not been previously reported at such a high of binding energy before. Typically, interstitial nitrogen at this B.E. derives from nitride-related peaks located at 404 eV. However, the previous oxidation experiment disproves that oxygen influences the formation of this peak. In contrast to previous research reported a detailed XPS analysis indicates the presence of interstitial nitrogen as shown by the presence of a sharp peak at 410 eV. The quantity of interstitial nitrogen increased significantly when the pure samples were bombarded with N_2 which

was revealed through a peak formation at 410 eV that was not observed in the samples before the treatment.

It has been reported that Ar^+ sputtering can facilitate the formation of nitrogen interstitials. This mechanism involves the displacement of N atoms from the Ga-N lattice into the interstitial position from the collision cascade caused by the ion bombardment. The theoretical studies have shown a defect state of Ga-N materials formed by ion bombardment. Although we suspect nitrogen to be predominantly binding to Gallium, there are multiple N configurations such as N-N split interstitials, N-As split interstitials, and isolated interstitial N. It has been reported that the formation of isolated N is unlikely because of its high formation energy. The defect energy levels predict this defect in the form of stable interstitial state of the N-N configuration in the form of a split interstitial.[69, 70] This could be why we see the higher binding energy shift to higher after argon sputtering. The energy provided by the argon ions break the Ga-N bonds on the surface leaving the Ga and N uncoordinated on the surface. The nitrogen can be displaced into the interstitial position.

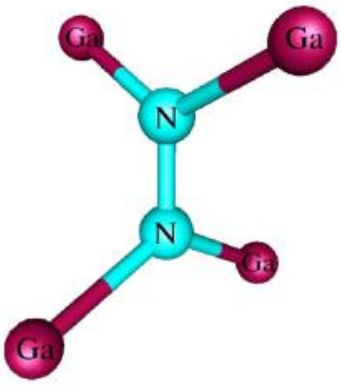

Figure 4.11. Geometry of N-N split interstitial in bulk GaAs

Figure Adapted from Carrier et al.[72]

The geometry of the N-N split in Ga-As is shown in figure 4.11 The nitrogen atoms might energetically favor moving out of the substitutable site to the neighboring interstitial site as the incorporation of nitrogen increases. Previous calculations have displayed that isolated interstitial nitrogen is typically unlikely because of their high formation energy in the lattice[71] Instead of this formation nitrogen would complex to form N-N split interstitials which are more energetically favorable to form. For this defect the most important transition levels in the bad gap are (0/-) transitional at 0.12 and 0.29 eV above the valance band maximum. This complex causes less strain in the epilayer compared to the substitutional N_{Ga}.

From the previous exploration of N-N interstitials and the peaks we are observing in the XPS spectra we are led to believe that we are observing these types of defects in the lattice. This is demonstrated upon nitrogen ion sputtering and increasing the intensity of the peak by forcing these ions further into the interstitial of the lattice. Although small amounts of N in these samples should reduce the band gap, however it is unclear how the N is incorporated into the lattice. From the experiments we have conducted during this study we believe that part of the nitrogen is mixed as an isovalent constituent forming a substitutional alloy, but small amounts are being incorporated as a defect in the form on split interstitials. Identifying these defects in the future will be possible with this presenting experimental evidence of this peaks location and further DFT calculations.

CHAPTER V

MEASURMENT OF VOLATILE ORGANIC COMPOUNDS IN AIR

1. Volatile Organic Compounds

Natural or anthropogenic sources of air pollution include fossil fuel combustion, coal-burning power plants, automobile exhaust, and wood-burning fumes. Urbanized areas are more susceptible to high concentrations and exposure to aldehydes, ketones, and particulate matter.

Volatile organic compounds (VOCs) have been found in rural, urban, and indoor air. These compounds have both a direct and indirect impact on human health. VOCs are defined as organic compounds with a boiling point ranging from 50-260 °C at room temperature and standard pressure.[1] The polarity, volatility, and concentration can range from low parts per thousand (ppt) to high parts per billion (ppb). Photochemical smog and tropospheric ozone formation are formed when VOCs emitted from natural and anthropogenic sources interact with UV light. These compounds typically consist of low molecular weight pollutants including C_2 to $C_{14\text{-}n}$, hydrocarbons, aldehydes, ketones, benzene, sulfur compounds, and many more. Some natural sources that emit VOCs are forest fires, vegetation, and animals. Although a large contribution of VOCs comes from natural sources, heavily populated and industrialized areas result in a majority of the anthropogenic sources.

These are not limited to biomass burning, refining, use of fossil fuels, household chemical products, and certain coatings and paints. The sources of VOC emissions from a 2017 study conduct in the European Union (EU) are shown in figure V-1.[2]

As people spend a majority of their time in indoor environments the adverse effect of indoor air pollution has become an issue of global concern. People in the US spend at least 90% of their time indoors, making this environment a key setting for potential human exposure to air pollution. Various factors can influence the air quality indoors such as proximity to anthropogenic sources, buildings design, air circulation rates, furniture within the building, and the occupants' habits. Pollutants that are generated indoors can come from smoking cigarettes, specific cleaning solutions, emissions from the building's paint or furniture, and personal care products.

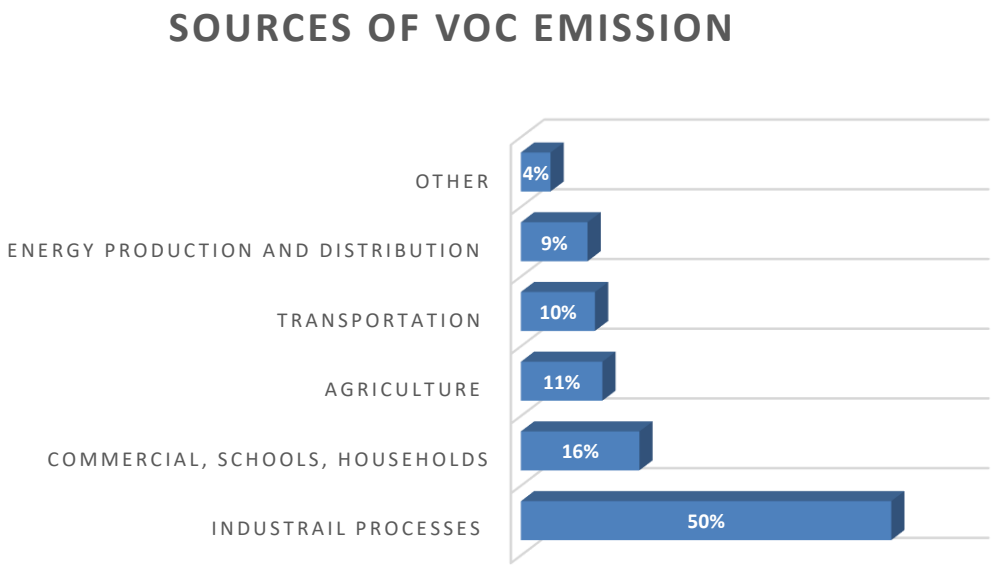

Figure 5.1. Sources of VOC emission in the European Union (28 area) in 2017[2]

Among various indoor air pollutants, low molecular weight aldehydes (formaldehyde and acetaldehyde) have become an important class of VOC because of their classification as known or probable human carcinogens. Air pollution has been listed as the greatest environmental risk to human health by the World Health Organization (WHO). Not only do these compounds cause potential health problems, but their reactivity in the atmosphere and high concentrations can also cause environmental problems. Aldehydes are present in the air we breathe but are also emitted from the products we use and consume.

2. Environmental Aldehydes and Exposure

Environmental aldehydes include acrolein, acetaldehyde, and formaldehyde. The burning of fossil fuels and the combustion of organic material releases high concentrations of aldehydes. It is estimated that 1-2% of aldehydes released are produced from vehicle exhaust, and the increase of ethanol-blended gasoline increased formaldehyde emissions by 30-50%. [3, 4] Industrial manufacturing releases aldehyde into the atmosphere as a by-product. Due to its high thermal stability and reactivity, formaldehyde is extensively used in the synthetic resin industry. This is of great concern in the industrial workplace, where formaldehyde has been measured as one of the most abundant carbonyl compounds.[5] Occupational exposure of aldehydes may occur from inhalation of vapors or direct skin exposure from persons working in aldehyde production industries, laboratories, and the healthcare industry. [6] The International Agency for Research on Cancer (IARC) classified acetaldehyde and formaldehyde as Group 1 carcinogens. The reactivity of the aldehydes due to their electrophilic nature gives them their toxic properties which can modify proteins and DNA. [7, 8]

Aldehydes can be generated indoors from existing infrastructure or can infiltrate from an external source. The combination of these two causes a higher concentration presence indoors compared to outdoors. [9] These compounds can vary in homes and buildings depending on a multitude of factors such as emissions, ventilation, and building design and materials. A list of some of the commonly detected indoor aldehydes and possible emission sources are shown in Table V-1 .

Table 5.1. Table of Indoor Sources for Formaldehyde and Acetaldehyde

Aldehyde	Sources
Formaldehyde	Building materials, pesticides, flooring, fuel-burning appliances, wood products
Acetaldehyde	Building materials, laminate, varnishes, paints, tobacco smoke, HVAC System,

Primary indoor emission sources of formaldehyde include decorative building materials, furniture that was bonded using urea formaldehyde resins and UF foam insulation, floorings, and other wood-based materials. Large quantities of formaldehyde are released from the interior components of building materials and furniture such as adhesives, wood glues, plywood, and synthetic fibers. Typically, the volatiles are contained deep within the material which results in a slow continuous release that decreases over time. Fossil fuel combustion is an important source of indoor formaldehyde since traditional fuels (biomass, coal, liquid petroleum, kerosene) are used as heating and cooking sources in the household, specifically in developing countries. [10]

With the growth in urbanization, the time which people spend indoors has increased. Indoor air quality (IAQ) has become an issue of concern as building-related illness (BRI) and sick building syndrome (SBS) have increased in recent decades.[11, 12] With a shift towards more energy efficient buildings with minimal air leakage and increased insulation these adverse side effects could increase. It has been shown that these building-related symptoms have increased negative health

effects, i.e., eye, nose, and throat irritation and headaches, and led to a decrease in productivity in the workplace and schools. [13]

Understanding concentrations of air toxins such as aldehydes within urban areas has been identified as a research priority. [14] There is a large range of chemicals that are detected in the indoor environment, therefore a complex method of analysis such as gas chromatography-mass spectrometry is used to quantify the compounds. Exposure limitations set by the Occupational Safety and Health Administration (OSHA) for formaldehyde and acetaldehyde are outlined below.

Table 5.2. Exposure limits for formaldehyde and acetaldehyde outlined by OSHA

Analyte	OSHA Exposure Limitations 8-hour-time-weighted average (PPM)	OSHA Exposure Limitations 15-minute-short-term exposure limit (PPM)
CH_2O	0.75	2.0
C_2H_4O	100	150

3. Sampling and Quantification Methods

There are various methods for sampling, analyzing , and quantifying VOCs present in specific environments outlined in Table 5.3. While there are handheld continuous read-out instruments used to collect atmospheric pollution data, they can vary due to environmental influences such as the activity of VOC emissions from industries, wind velocity and direction, and peak traffic times. This causes fluctuations in VOC concentrations making it difficult to accurately assess the concentrations that could led to adverse health effects. This type of detailed sampling requires a

more in-depth method. Due to the nature of VOCs in air, a better analytical assessment is needed to accurately evaluate the concentrations.[15]

Table 5.3. Table of common analysis methods for VOC

Analysis Method	Pro	Cons
Gas Chromatography- Thermal Desorption with Flame Ionization Detector (FID)	High sensitivity and linear in response, good for fixed site observations in serviced laboratory, stable and reliable	Not selective and will respond to all organic compounds except HCHO, identification based on retention times, unable to identify unknown compounds, not portable, and requires hydrogen gas
Thermal Desorption GC-MS	High sensitivity, capable of identifying unknown compounds in air samples from MS library, increased sensitivity with selected ion modes	Benchtop analysis set up too large for field analysis, challenging to calibrate, moister can interfere with measurements
Proton Transfer Reaction Mass Spectrometry (PTR-MS)	High sensitivity to numerous VOCs, no sample treatment, fast response	Only identifies mass of product ions, cannot distinguish isomers, not portable, expensive (200K-400K)
Bulk Photoionization Detection (PID)	Handheld detector, lower power demands, can be used to pinpoint the source of VOC emission	Not selective to one gas requires calibration for each VOC, photochemical reactions with vapors can cause reduced sensitivity from the internal surface coating.

Gas Chromatography-Mass Spectrometry (GC(MS)) is the most common analytical technique for detecting and quantifying a broad range of compounds that have reasonable volatility and thermal stability. The method consists of liquid extraction coupled with GC(MS). Typically, activated charcoal is used for air sampling, while carbon disulfide is used to extract the adsorbed organics. This technique tends to have lower sensitivity to other available methods because of solvent

dilution during extraction. Additionally, because of its polarity and strong binding interactions charcoal cannot efficiently desorb the organics in aqueous and polar environments.

Thermal desorption (TD) combined with GC is used to determine VOCs in air samples even at low concentrations (0.5 ppb-25 ppb). Thermal desorption is used to extract the target compounds from a sorbent material and transfer them to the GC(MS) analytical instrument (Figure 5.2). This method offers advantages over using a sampling canister by reducing the cost per analysis because there is no sample preparation and no air extraction equipment needed. Using thermal desorption tubes offers better recovery than the canister method for a wider range of vapor phase organics and polar compounds.

The TD process employs a high purity intern gas (typically helium) that is used in high-temperature extractions. The target compound is transferred from the air sample to the pre-concentrator which is either a cryogenic trap or an electrically cooled Peltier trap. The VOCs are desorbed from the tube using high temperatures and a stream of helium to transfer them into the trap for pre-concentration. In the final step, the helium flow is inverted through the trap and the cold trap is rapidly heated to a high temperature at the maximum rate to transport the VOCs into the GC(MS).

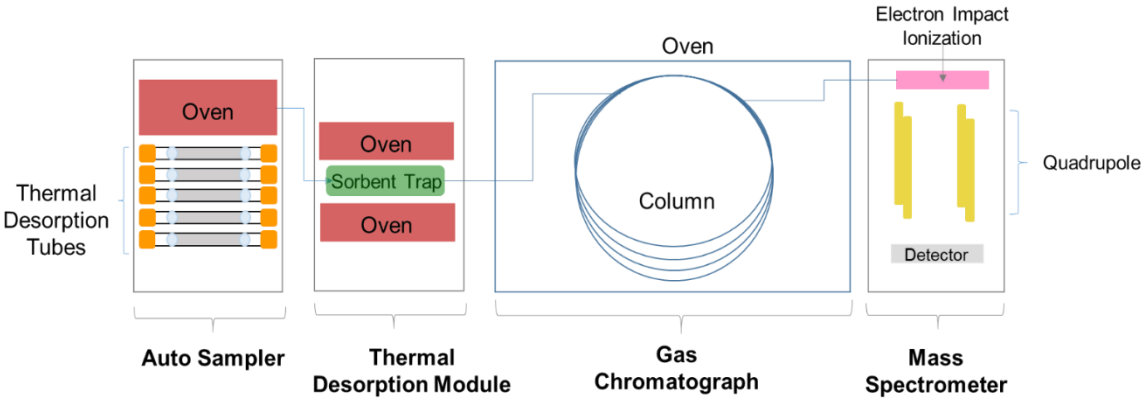

Figure 5.2. Schematic of thermal desorption coupled with gas chromatography/mass spectrometry

Whole air sampling methods consist of collecting the air sample using tightly sealed containers such as highly durable polymer bags or stainless-steel canisters. During canister whole air sampling, samples are collected by drawing air through an orifice into the evacuated vessel by free or applied movement (vacuum). Prior to analysis, the samples are withdrawn, and enrichment of the VOCs is carried out using a cold trap to improve the sensitivity of the method. The sample is then analyzed through GC(MS) to determine concentrations of the collected compounds. Multiple analyses can be performed on one sample by injecting aliquots of air from the sampling vessel into the instrument. This method can be used to accurately quantify the amounts of extremely volatile compounds such as acetylene, N_2O, H_2S, and SF_6. However, problems arise when too much moister is present in the sampling environment. Water is a severe interference and limits the sample quantity from which the compounds can be pre-concentrated while freezing in the cryogenic traps. Clogging at the cryogenic trap and capillary interface can occur from high moister levels as well. Limitations also arise with the cost of transporting the heavy containers and equipment for cleaning the vessels.

Polymer bags could ease the transportation prices of stainless steel canisters and offer a wide range of volumes. [16]Although multiple polymer bags are available, Tedlar is the most commonly used. The use of these bags is outlined for use in various EPA compendium methods (TO-3, TO-12, TO-14A, TO-15A). The bags are cleaned thoroughly by repeatedly filling the bag with an ultra-pure inert gas and evacuating it under a small amount of pressure. The outgassing procedure of the container material leds to large contamination levels. These bags are reusable but do require a rigorous cleaning procedure using an ultra-pure inert gas. Micro-damages and defects from mechanical stress during sample handling can alter the polymer film structure and interness of the material, so repeated bag usage is not recommended.[17]

3.1. Sorbent Sampling

Sorbent tubes are widely used in combination with GC and thermal desorption. Target compounds can range in volatility and include polar, apolar, and reactive species. An assortment of sampling techniques and sorbent materials have been developed to be used in specific applications. These techniques include passive (diffusive) sampling onto sorbent tubes, active (pumped) sampling onto sorbent tubes, and transfer of whole air samples from canisters or bags onto sorbent.

During sorbent sampling, the target analyte is entrapped onto a solid adsorbent material followed by thermal desorption and chromatographic analysis. The thermal desorption of these compounds from the sorbent offers a higher level of sensitivity than other methods because there is no dilution of the sample. Sorbent tubes allow for high recovery of polar and reactive target compounds, that would otherwise react using a canister. Unlike other sampling methods, sorbent tubes are relatively small, easy to condition, facilitate collection, and transport. [18, 19] Sample tubes can usually be reused at least 100 times before the sorbent material needs to be replaced. Optimizing the sorbent material is necessary to prevent artifact formation and breakthrough problems when sampling. The selection of the sorbent material is very critical and depends on the sample matrix and the target compound. Recovering compounds that are non-volatile and strongly adsorbed onto the material and breakthrough problems with volatile compounds are the limiting steps of this method. The environmental sampling conditions (humidity, temperature, and concentration) can impact the quantity of the substance that is captured on the sorbent.[20-22]

Passive sampling typically consists of open-faced badges or cartridges that contain sorbent material. [23] This sampling method is best suited for long-term monitoring to allow for sufficient concentration of the compound onto the sorbent material. During molecular diffusion, the compounds move from an area of high concentration to an area of lower concentration and

diffuse into the tube and collects on the adsorbent. The limitations of these sampling devices come in terms of surface air velocity and back diffusion. Passive sampling utilizes the two concepts of axial diffusive samplers and radial samplers. Axial diffusive sampling was developed in the late 70's and is comprised of a stainless-steel tube packed with a single sorbent and capped with a fine mesh gauze. A fixed 15 mm air gap between the surface of the sorbent and the gauze allows for diffusion across a barrier. The sampling surface and air gap can be fixed and provide the vapor concentration at the sorbent surface, while the sampling rate is a constant function of atmospheric concentration.

Radial diffusive samplers are typically comprised of a cartridge containing the sorbent sampling material housed in a porous polymer body that allows for sampling around the circumference of the cylindrical surface. To minimize air velocity effects and low uptake a porous polymer is used however, the sorbent material saturates relatively quickly and back diffusion occurs. These sampling devices are well suited for short-term (0.5 h to 6 h) air monitoring at low concentration levels.

Active sampling onto a sorbent tube is one of the most used TD sampling methods. This approach utilizes a pump to draw an air sample through the sorbent tube to trap the target analyte on the sorbent material. In the last 10 years, international standard methods including thermal desorption, procedures have grown rapidly. There are now TD standards that cover a wide range of sampling environments such as ambient, indoor, and workplace atmospheres. The most used EPA method (TO-17) employs the use of TD tubes that are 3.5" long with an outer diameter of 6.4 mm and an inner diameter of 4 mm for glass and 5mm for stainless steel shown in Figure 5.3. The total mass of the sorbent typically ranges from 100-600 mg. These tubes have the capacity to be packed with up to three discreet sorbent beds that are arranged in order of increasing sorbent strength from the sampling output. Since the sorbent selection is specific for each target analyte the tube size is allowed to be constrained within the range described in the standard method

without concerns for lower retention of the organic compounds. During active sampling, a known volume of air is pulled through a sorbent tube at a constant flow rate (20-200 ml/min).[24] The limiting factors in active sampling are typically related to sorbent selection and preparation.

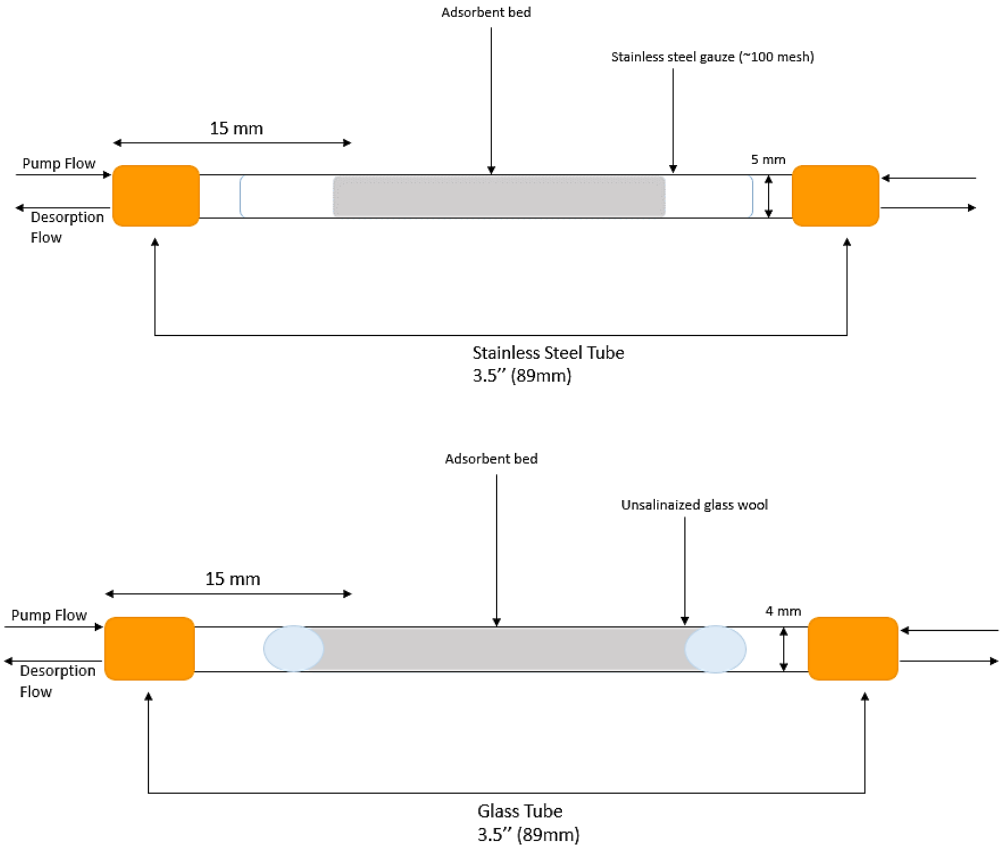

Figure 5.3. OSHA standard stainless steel and glass sorbent tube parameters

3.2. Sorbent Selection

The consideration of sorbent strength (analyte breakthrough), artifact formation, and sampling environment (relative humidity) need to be considered when selecting the sorbent material and types of sorbent tubes. The Environmental Protection Agency (EPA) outlined situations where one sorbent is not well suited for the capture of all compounds so, it is essential to select a sorbent

capable of sorbing the class of compounds with the highest health risks or deploy multiple samplers to capture all of the compounds of interest. The most important information from the application of adsorbents is the breakthrough volumes. This is defined as the collection efficiency, the retention value for the adsorbate versus adsorbent combination, and the number of theoretical plates of the adsorbent.[25-28] The breakthrough volume and characteristics give information for field sampling in order to calculate safe sampling volumes. During sampling, it's possible for the sorbent to show degradation problems that can impact the adsorption process. During sampling and thermal desorption oxidizing reactions can occur on specific adsorbent materials. Moister retention on sorbents is typically avoided because water content may cause degradation of the chromatographic column. The most widely used sorbents for organic gas sampling can be found in table 5.4.[16, 29-32]

Table 5.4. Common sorbent materials used for VOC sampling

Adsorbent Name	**Adsorbent Class**	**Suitable Analytes**	**Surface Area (m^2/g)**	**Advantages/Disadvantages**
Activated Carbon	Graphitized Carbon	- Most non-polar VOCs - Slightly polar VOCs	2000	- High Capacity - Reactive with some compounds
Carbotrap	Graphitized Carbon	- Most non-polar VOCs - Slightly polar VOCs	100	- Low background - Reactive with aldehydes
Carboxen	Carbon Molecular Sieves	- Polar VOCs - Non-polar VOCs	700-1200	- Significantly hydrophilic - Low artifacts - Retains water in high relative humidity's
Carbosieve	Carbon Molecular Sieves	- Mostly polar VOCs - Chloromethane	820	- High capacity/ Breakthrough - Low desorption efficiency
Adsorbent Name	**Adsorbent Class**	**Suitable Analytes**	**Surface Area (m^2/g)**	**Advantages/Disadvantages**

Porapak	Porous polymer	- Most non-polar VOC	300	- High background - Low thermal stability
Tenax TA	Porous polymer	- Most non-polar VOCs - Slightly polar VOCs - Aldehydes - Terpenes	35	- Low background - Low surface area - Does not react - Decomposition can occur
Silica Gel		- Polar hydrocarbons - Low molecular weight mercaptans - Inorganic acids	750	-High surface area -Low reactivity -Not compatible in high humidity environments

3.3. Sorbent Strength

The adsorption/desorption relationship largely determines the analytical sensitivity and precision of this method. The sorbent must be selected to sufficiently retain the target analyte during sampling but weak enough to desorb it during the thermal desorption phase. The retention of breakthrough volume is typically used to measure the sorbent's strength. A stronger sorbent is one that offers greater safe sampling volumes for most organic compounds relative to different weaker sorbents. Sorbent strength is usually related to the surface area, generally weaker sorbents are described if their surface area is less than 50 m^2/g (Tenax, Carbopack C), medium strength if the surface areas are in the range of 100-500 m^2/g, (Carbopack B), and strong if the surface area is around 1000 m^2/g (Sperocarb, Carbosieve S-III, Carboxen 100).[33] The strongest sorbents are used to capture the most volatile species. Ambient conditions can affect retention volumes of the sorbent. The retention volumes of hydrophobic sorbents such as Tenax TA, carbon black, and high porosity polymers are not as sensitive to relative humidity like carbonized molecular sieves are. When sampling VOCs the weakest compatible sorbent should be selected because it offers reliable retention volumes and quick quantitative recovery during thermal desorption and quantitative analysis.[34, 35] Commercial sorbet are available in a wide range of strengths that allow

for quantitative retention and release of organic compounds. However, these sorbates have issues with artifact formation, recovery, and humidity effects.

During the recovery process, some sorbents are known to release organic compounds closely associated with the nature of the sorbent. Some of these porous polymers such as Cromosorb, HayeSep, and PoraPak, have been shown to have relatively high artifact formation associated with thermal desorption.[36] Carbonized molecular sieves and carbon black tend to not have any inherent artifacts but are more likely to contain chemically active materials. Sorbents derived from natural charcoals are generally unsuitable for reactive species.[19]

Water and water vapor can greatly influence the collection and analysis of VOCs. Relatively high humidity's have been the most critical concern affecting the validity of VOC measurements. Weak and medium strength sorbents including porous polymers (Tenax TA) and graphitized carbon (carbopack) are selected for high relative humidity (>80%) sampling because of their hydrophobicity.[35] Strong sorbents are typically less hydrophobic (Carbosieve, Carboxen, carbon molecular sieves) and facilitate the retention of high volatility polar analytes, but excessive water retention on the adsorbent material causes breakthrough and leds to artifacts during thermal desorption analysis. [36, 37]

Nanoporous silica is one solution. With a large surface area and uniform pore distribution, nanoporous silica has high sorption capacities and VOC sampling capabilities. In the 1970s the first patent for the preparation for low-density silica was filed which eventually led to the synthesis of the first nanoporous silica material.[38, 39] This family of materials has uniform pore distribution and relatively high surface areas (>1000 m^2/g) resulting from a self-assembling molecular array of surfactants used as the organic template. Nanoporous silica production involves adding a silicate source to an aqueous surfactant solution followed by hydrolysis and

condensation to builds a silica framework around the surfactant micelles. The surfactant is then removed by microwave digestion, calcination, or solvent extraction.[40]

Previous studies have focused on the use of MCM-41 and SBA-15 for the adsorption of organic pollutants from the air. Mobile Composition of Matter (MCM) and Santa Barbra Amorphous (SBA) are made of hexagonal, cubic, or meso-lamellar phases. The sampling process using these materials involves organic molecules adsorbing on the surface of the silica by van der Waals forces (London dispersion forces and dipole-dipole interactions). The strength of this material is fairly weak so desorption from the surface is possible through heating or solvent extraction. A range of pore sizes can be achieved by manipulating the alkyl chain length of the surfactant template, which can improve the selectivity of adsorption by immobilizing the gas molecules of certain sizes. [41] The hexagonally structured nanoporous silica material was originally created as molecular sieves with a wide range of pore sizes. The particularly high internal surface area and ability to precisely tune the pore size are some of the favorable properties that have made these materials of high interest. Unlike carbon-based sorbents that are currently being used, nanoporous silica does not contain reactive groups that could interfere with sample collection and subsequent analysis.

4. Problems with Aldehyde Sampling

The use of an inert sorbent is especially important when sampling reactive carbonyls like acetaldehyde and formaldehyde. Although several standardized methods are outlined by the U.S. EPA (Method 0100) they lack ease in use and contain data quality concerns. Typically, the method relies on 2,4-dinitrophenylhydrazine (DNPH) functionalized sorbent materials, but it has been known that ozone interferes with formaldehyde measurements by degrading DNPH and DNP-hydrazones. Another difficulty arises with the encounter of nitrogen dioxide (NO_2) on the DNPH-coated sorbent which reacts and forms 2,4-dinitrophenylazide (DNPA). Formaldehyde-

DNP-hydrazone and DNPA show similar chromatographic properties, which may result in higher formaldehyde concentration estimates. [42, 43] There is also competition for the adsorption sites during sampling, the aldehyde along with NO_2 and ozone is drawn into the sorbent tube simultaneously. When all of these compounds are competing for adsorption on the surface the aldehyde could be released prematurely before it can react with the DNPH.

To mitigate the interference from these compounds, the EPA suggests removing ozone prior to sampling. This involves constructing an ozone denuder or scrubber that can intercept the contaminant before it reaches the sorbent tube. However, the use of an upstream ozone scrubber can oxidize NO to NO_2 which can interfere with quantification.[44]

Although these discoveries have been made with NO_2 and ozone interference during formaldehyde sampling new method development has been lacking because standard methods have not yet been modified to reflect these latest discoveries. Comparable to formaldehyde sampling, acetaldehyde sampling on DNPH coated sorbents exhibit similar interferences. Collection efficiencies (CE) concerns with acetaldehyde are demonstrated during a 24-h sampling period (EPA standard sampling period) with CE ranging from 1-62%. [45] Consequently the concentrations of acetaldehyde that were adsorbed on the DNPH-coated material are frequently underestimated and concentration biases continue to propagate through important data collection outlets. The need for a practical solution for increase CE with acetaldehydes lies in developing a new sorbent material used in sampling.

CHAPTER VI

OSU-6 SORBATE AS ALDEHYDE SAMPLING MEDIUM

1. OSU-6 Sorbate

Many organic compounds and sampling environments are unstable with respect to oxidation, decomposition, and reactions with functional groups present on the surface of the adsorbent. In this study, a nanoporous silica material called OSU-6 will be investigated for its use in acetaldehyde and formaldehyde capture and desorption. The use of this material will mitigate problems that arise during sampling with the use of nanoconfinement technology that stabilizes unstable organic compounds. This silica material consists of hexagonal arrays of tubular pores with a diameter of 3.5 nm. The Barrett-Joyner-Halenda (BJT) pore diameter and high curvature allow a large range of different chemical compounds to bind by the cumulative addition of nonspecific Van der Waals forces.[46] The non-specific nature of the attractive forces with sorbates promulgated by the nanoconfinement effect means that it is capable of sorbing an extensive array of chemical classes with high capacity.

OSU-6 does not contain any functional groups or additives that can interfere with analysis like other available sorbents such as graphitized carbon black. This material has previously been shown to have high thermal stability and resistance to hydrolysis when compared to other available mesoporous or nonporous silica.[47] Adsorbed molecules are in proximity to more than one of the pore walls and are held by stronger forces. Therefore, the neighboring adsorbed

molecules enhance the adsorption effect. A series of laboratory tests and calculations were performed using OSU-6 to determine its adsorption capabilities with acetaldehyde and formaldehyde.

2. BET Analysis

Adsorption isotherms are used to measure the amount of gas adsorbed by a material at a constant temperature as a function of pressure. Characterization of the pore structure is important to understand the diffusion of the gas molecules within the porous system. Braunauer, Emmett, and Teller (BET) isotherm for nitrogen gas adsorption-desorption is a commonly used technique to study the physical adsorption of the material. During BET analysis nitrogen is adsorbed on the surface at cryogenic temperatures (-150°C), because most gases and solids interact weakly. The temperature of the solid is held at isothermal conditions, while the pressure of the adsorbing gas (nitrogen) increases. Increasing the pressure causes more molecules to adsorb on the surface forming a thin layer, in which the number of molecules on the monolayer can be recorded from the volume adsorbed. The available surface can then be calculated from the cross-sectional area of the adsorbate. A mathematical model must be used to calculate the surface area since gas adsorption as a function of pressure does not follow a linear relationship.[48]

The BET model assumes multilayer adsorption of a gas on the adsorbent's surface and provides information on how the solid will interact with its environment. In materials containing small pores (2-3 nm in diameter), capillary condensation can take place above the pressure region instead of multilayer adsorption, this data should be excluded during subsequent calculations to avoid an overestimation of specific surface area.

The specific surface area of the sorbent material can be determined by the physical adsorption of nitrogen onto the surface at cryogenic temperatures. The amount of adsorbate gas is measured by

a volumetric flow technique, to which calculations can be applied. The physical properties of the sorbent such as pore size, pore-volume, surface area, and particle size are all properties that can influence adsorption/desorption.

The adsorption-desorption isotherm for OSU-6 sorbate is shown in Figure 6.1. The curves are typical for mesoporous materials containing hexagonal channel arrays. This isotherm resembles Type II isotherms according to IUPAC classification, which is identified by adsorption on nanoporous solids through multilayer adsorption followed by capillary condensation. An increase in adsorption took place above $P/P_0 = 0.2$, which suggests capillary condensation of N_2 within the pores confirming the presence of nanopores. The capillary condensation in the nanoporous matrix and limiting uptke causes an H-1 hysteresis loop.[49]

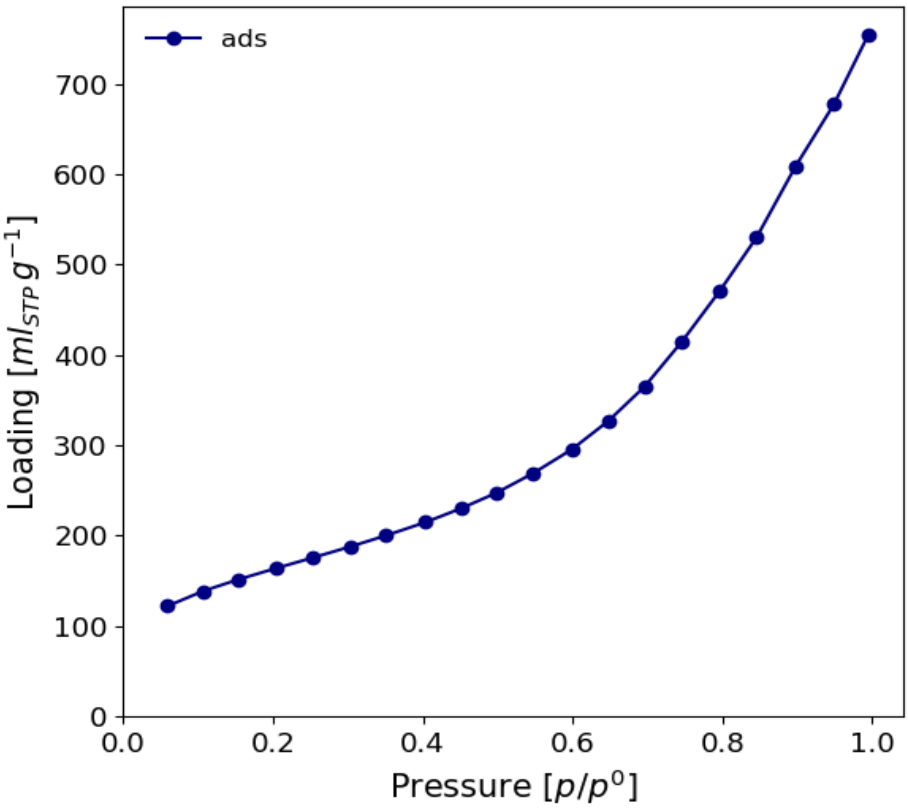

Figure 6.1. Nitrogen Adsorption isotherm for OSU-6

The BET equation below utilizes the information from the isotherm to determine the surface area of the sample where X is the weight of nitrogen adsorbed at a given pressure (P/P_0), X_m is the monolayer capacity, which is the volume of gas adsorbed at standard temperature and pressure (STP), and C is constant.[50]

$$\frac{1}{X[P_0/P]} = \frac{1}{X_m C} + \frac{C-1}{X_m C}\left(\frac{P}{P_0}\right) \qquad \text{[Equation VI-1]}$$

2.1. Multi-Point BET

During a multi-point BET, five data points in the P/P_0 range of 0.05 to 0.30 are used to determine the surface area using the above equation. The monolayer capacity X_m can be determined by the following equation:

$$X_m = \frac{1}{s+i} = \frac{C-1}{C_s} \qquad \text{[Equation VI-2]}$$

From the monolayer capacity determination, the total surface area can then be calculated from the following equation where L_{av} is Avogadro's number, A_m is the cross-sectional area of the adsorbate (0.162 nm^2 for N_2 molecule) and M_v is the molar volume (22414 mL)

$$S = \frac{X_m L_{av} A_m}{M_v} \qquad \text{[Equation VI-3]}$$

A linear section from the adsorption curve is used for these calculations. The BET equation is plotted to determine the monolayer of adsorbed gas quantity and BET constant. From the monolayer adsorbed gas volume, the specific surface area was determined. The BET plot is

shown in figure 6.2 where five points were chosen, and the model was applied to achieve a linear fit. We assume a linear relationship for adsorption isotherms in the range of $0.5 < \rho/\rho_0 < 0.30$.

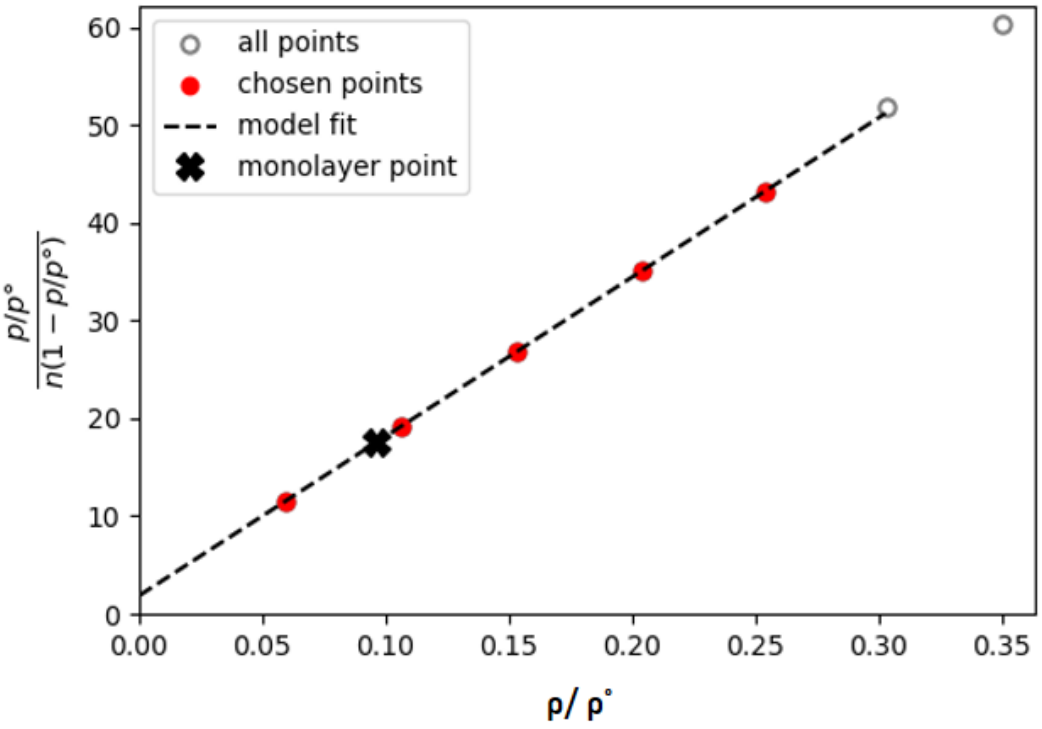

Figure 6.2 . Multipoint BET plot for OSU-6

2.2. BJH Method

The pore volume is determined in a subsequent experiment in which the gas pressure is increased further until all of the pores are filled with the liquid nitrogen. Following this, the pressure is incrementally reduced until all the condensed gas is evaporated. The BJH (Barrette, Joyner, and Halenda) method was then applied to calculate the pore volume. These calculated values are outlined in Table 6.1.

Table 6.1. Specific Surface Area and Pore Volume of OSU-6 determined from BET and BJH analysis

Material	Specific Surface Area (m^2/g)	Total Pore Volume (cm^3/g)
OSU-6	583	3.12

3. Aldehyde Quantification

3.1. Acetaldehyde Quantification

After the completion of the breakthrough determination (Chapter VII), the analyte can then be quantified using thermal desorption-gas chromatography-mass spectrometry (TD-GC/MS). A standard thermal desorption tube (EPA Method TO-17) was packed with fresh OSU-6 and exposed with acetaldehyde for 3 ,6 , 9, and 12 minutes at various RH levels. Following acetaldehyde capture, the tube was then thermally desorbed, pre-concentrated, and injected into the GC-MS. The chromatograph from the GC(MS) for acetaldehyde is shown below.

3.2. Formaldehyde Quantification

Prior to formaldehyde quantification via TD-GC(MS) an intermediate step must be completed. In order to obtain a representative signal from the GC(MS), the formaldehyde must first be desorbed from the OSU-6 sorbent tube onto a DNPH-coated sorbent tube (Figure 6.3). Through the functionalized tube an appropriate concentration of formaldehyde can be determined. Although sampling interference can arise with DNPH from air oxidants such as nitrogen dioxide and ozone, using an OSU-6 sorbent tube to sample the analyte initially will mitigate any problems that stem from these compounds.

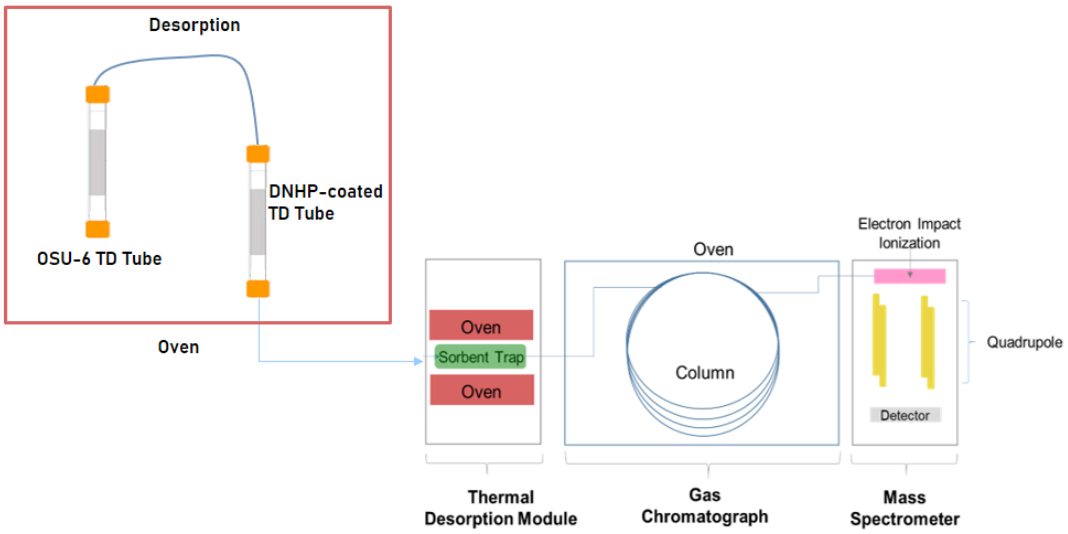

Figure 6.3. Desorption from OSU-6 TD tube onto DNPH-coated TD-tube before GC(MS) analysis

Once the formaldehyde was desorbed onto the DNPH-coated tube it was then injected into the GC(MS) for quantification. From the chromatograph, we see that the intermediate step of desorbing from the OSU-6 TD tube onto the DNPH functionalized tube the concentration of formaldehyde in the sample was able to be determined. This was completed at the same RH and column lengths as the acetaldehyde experiments.

4. Sampling Capacity

Although the physical characteristics of the sorbent are vital properties for analyte capture, the extraction ability of sorbents during TD-GC(MS) analysis depends on the breakthrough volume and sorbent capacity. The breakthrough volume is the amount of gas that causes a compound to migrate through an adsorbent bed of one gram at a specific temperature. [51] The breakthrough volume allows for an estimation of the maximum sampling volume that guarantees a quantitative

sampling of a compound using a certain adsorbent mass at specific sampling conditions. The breakthrough volume can be described by a breakthrough curve, which involves the relationship between the analyte concentration and the volume passed through the sorbent. The kinetic and retention parameters can influence the breakthrough volume (BTV) and the performance of the sorbent. The term breakthrough volume is comparable to the retention volume of the analytes, however, in order to express this value in terms that can be widely used with different column sizes, it is expressed as the volume of the carrier gas that will purge the analyte of a given volume or weight of the sorbent bed. [52]

The breakthrough volume is typically determined by using online or offline methods. These two experimental approaches include elution and frontal chromatography. These two methods involve filling an adsorbent tube with a known amount of adsorbent material and analyzing the breakthrough via GC. The chromatograms from these experiments provide data to quantify the breakthrough behavior. The actual BTV can be calculated using the reduced breakthrough time. [53] Typical experimental determination methods, off-line methods, in particular, are very time-consuming and expensive.

In this study, a benchtop sampling apparatus (Figure VI-4) was used to determine the sampling capacity of the OSU-6 sorbent. Air is passed through a humidification module which is controlled by a Dakota Instruments mass flow controller (± 1%) varying the flow rate based on the target RH. The tested RH values were 0%, 40%, and 80%. To ensure the sorbent has fully saturated the humidity inside the analysis chamber was monitored using an Omega USB-RH Sensor (±3%). Once the humidity levels stabilized, zero-grade air was passed over the sorbent for 1 hour. Zero-grade air was employed as the carrier gas for the target analyte, this was controlled through two mass-flow controllers. The total flow rate was held at 50 mL/min with the formaldehyde concentration at 0.5 ppm (lower than OSHA exposure limits). The use of an automatic switch was

employed to mitigate a spike in resistance that occurs at the onset of the experiment and minimize error with breakthrough times.

The breakthrough experiments were conducted with column lengths of 30mg, 45mg, 60mg, and 75mg. The OSU-6 (40/60 mesh) was packed into a Markes' industry-standard thermal desorption tube with an 8.9-cm length and 4-mm internal diameter. The two ends of the tube were sealed using a small piece of glass wool and secured with a metal spring to withstand the high flow of gases. Prior to breakthrough analysis, the packed sorbent tubes were conditioned in a Markes' TC-20 tube conditioner. The tubes were loaded into the conditioner and heated under a flow of research plus nitrogen (99.9999%) gas at 180° C for 2 hours.

The breakthrough of the target analyte was detected using a Grove-HCHO chemiresisitve sensor which was stored in the analysis chamber at the end of the TD tube containing OSU-6 sorbent. The breakthrough time was recorded by the time taken by the sorbent to become 50% saturated with the analyte and corrected for the value obtained from the blank column. The same experiment was conducted for acetaldehyde but at a higher concentration of 50 ppm.

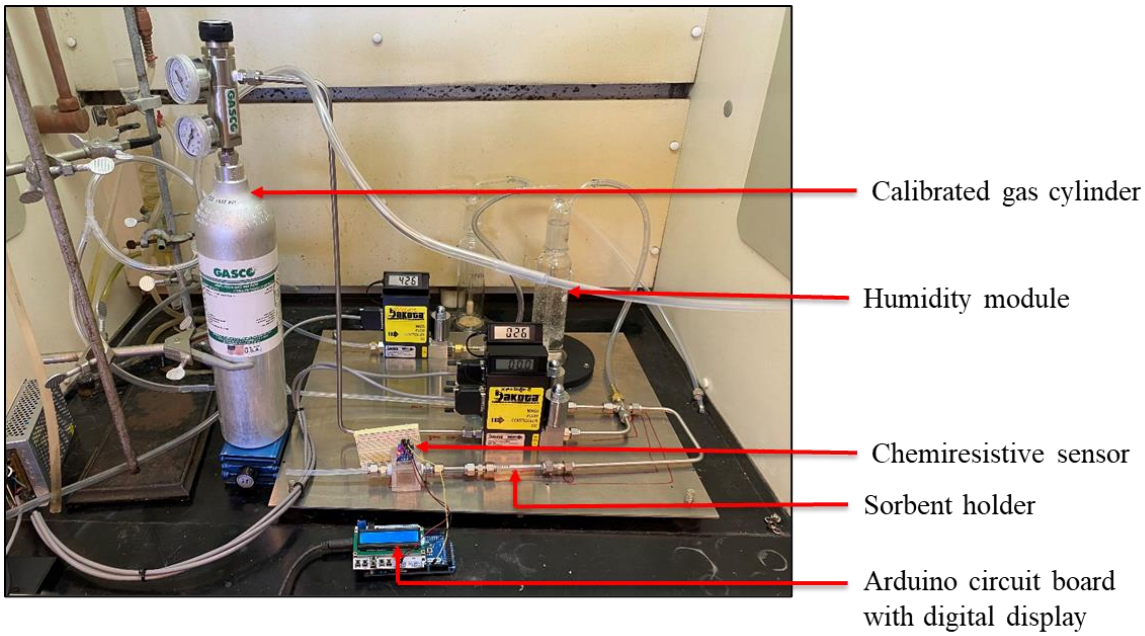

Figure 6.4. A representative apparatus that incorporates chemiresistive sensors for the real-time detection of aldehydes

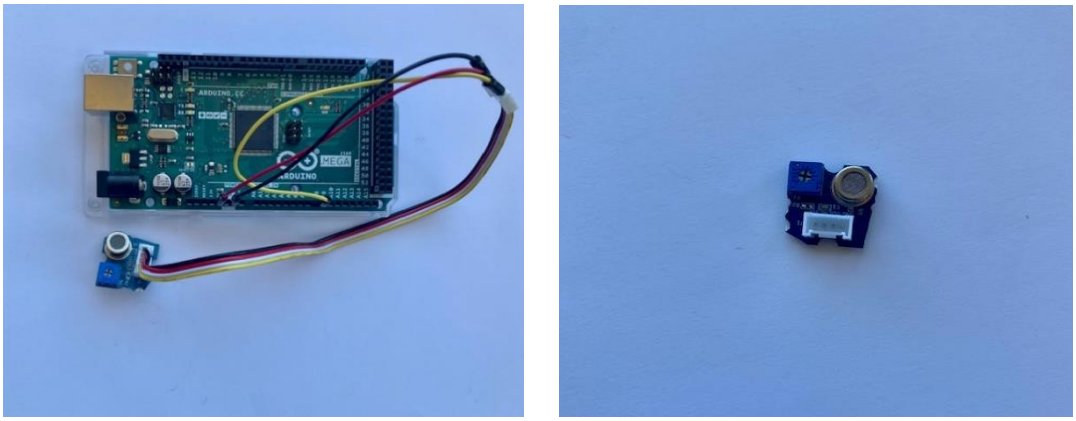

Figure 6.5. Chemiresisitve sensor with Arduino circuit board (right) and Groove HCHO chemiresisitve sensor (left)

CHAPTER VII

ALDEHYDE BREAKTHROUGH QUANTIFICATION

1. Breakthrough Experiments

The breakthrough experiments were performed by passing zero-grade air through the sorbent column. After allowing the sensor to stabilize the target analyte was passed through, a decrease in the signal for the chemiresisitve sensor was observed until it reached a minimum intensity. The breakthrough point denotes 100% of the analyte permeating through the sorbent. For all of the experiments, the breakthrough time was measured when the sorbent adsorbed 50% of the analyte exposure concentration. This time will become longer by increasing the sorbent column mass. The effect on the adsorption of water vapor during analysis specifically with polar molecules is of great importance and must be investigated. To assess the effects of moister concerning adsorption capacities varying levels of relative humidity (RH) were introduced to the column before and during analysis.

The sampling capacity of the sorbent for acetaldehyde and formaldehyde was determined as a breakthrough volume (BV). This is used to evaluate the performance of the sorbent under various column lengths and relative humidity. The breakthrough volume is used to assess the safe

sampling volume (SSV) before the analyte of interest is quantitatively eluted off the packed sorbent bed and is absent or undetected. Understanding the BV is necessary in order to assure the analyte of interest is adsorbed on the surface and are not purged off the sample during collection. The chemiresistive sensor (Figure 6.5) was used to determine the amount of gas passing through the column. When the sensor interacts with the target organic gas the resistance of the sensor decreases, which can be used to determine the breakthrough points of the analyte from the change in resistance.

Thermal desorption tubes were used in this experiment as a default sample holder to conduct the breakthrough analysis of formaldehyde and acetaldehyde vapor through a sorbent column. Only a background signal was observed using the chemiresisitve sensor at the onset of the experiment when the analyte was passed through the sorbent column. As the OSU-6 sorbent started to saturate with the aldehyde vapor a breakthrough from the background signal sets off. A decrease in signal is observed until it reaches a minimum intensity at a breakthrough point when the sorbent is completely saturated.

The uptake capacity for formaldehyde and acetaldehyde on the OSU-6 sorbate was analyzed using a benchtop apparatus containing a chemiresistive sensor for real-time analysis. The data was recorded at various RH (0%, 40%, and 80%) with several column lengths (30mg, 45mg, 60mg, and 75mg). As the pores in the sorbent started to saturate, the contaminated gas started to escape through the column and reached the sensor which caused a decrease in the resistance value. Figure 6.6 depicts a representative signal obtained from the chemiresisitve sensor that was located in a plastic housing at the end of the TD tube containing 60mg of OSU-6 sorbent at 40% RH.

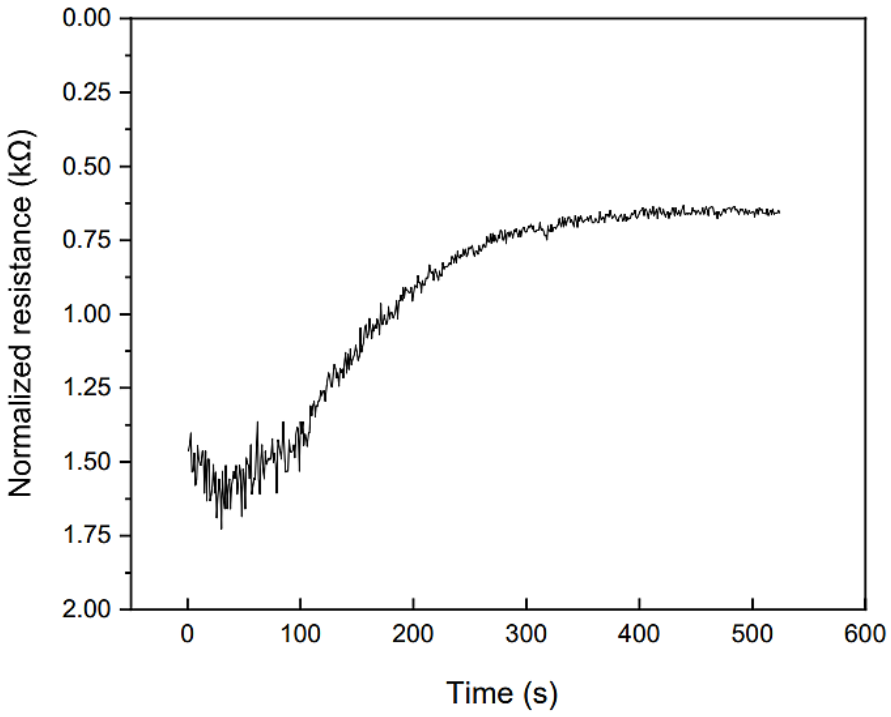

Figure 7.1 Change in the resistance measured by Groove HCHO sensor with an increase in the formaldehyde concentration

The resistance was normalized to show an increase with corresponding analyte concentration, so the y-axis illustrates the decrease in the resistance with an increase in the formaldehyde concentration. The breakthrough time was denoted by the time taken for the sorbent to reach 50% saturation with the target analyte. During a typical uptake experiment, the resistance value of the sensor stayed constant as the sorbent adsorbed the target analyte (formaldehyde or acetaldehyde). To reduce the effects of a resistance spike at the onset of the experiment an automatic switch was installed in the setup. The breakthrough time was expected to increase with an increase in the sorbent column mass or length.

The breakthrough curve below is a representative signal obtained for acetaldehyde, measured with a Grove HCOC sensor with a TD tube containing 60mg OSU-6 at 40% RH.

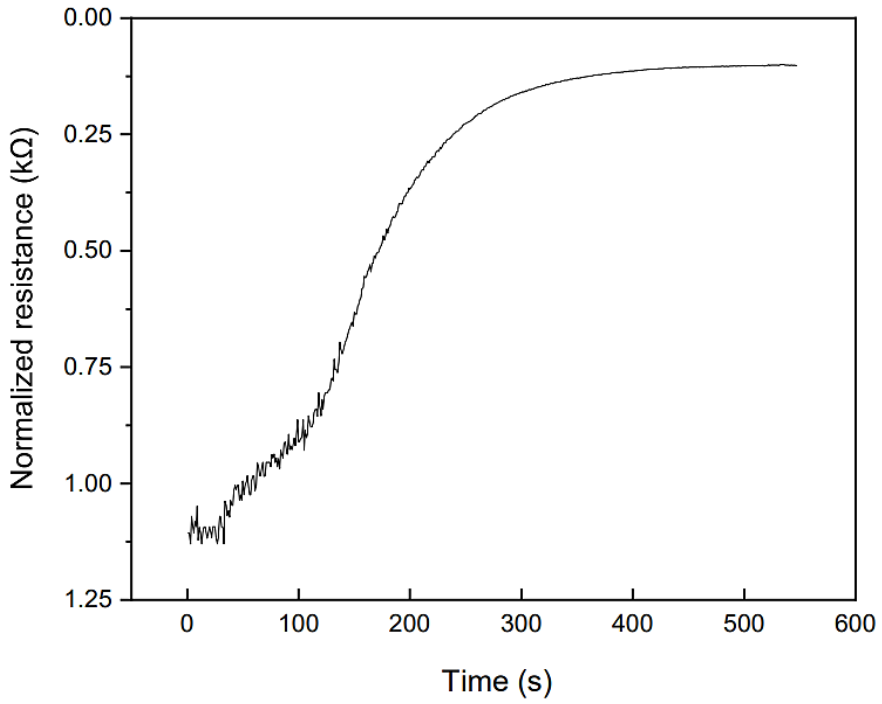

Figure 7.2. Change in the resistance of the Groove HCHO sensor with an increase in the acetaldehyde concentration

For each breakthrough curve obtained, the time between the initial exposure and the point corresponding to 50% of the breakthrough intensity (50% breakthrough time) was determined and then corrected with the value that was acquired for the column without OSU-6 sorbent (blank column).

The 50% breakthrough time for all three RH values with formaldehyde were plotted linearly as shown in Figure 7.3 and the breakthrough values are quantified in table 6.2.

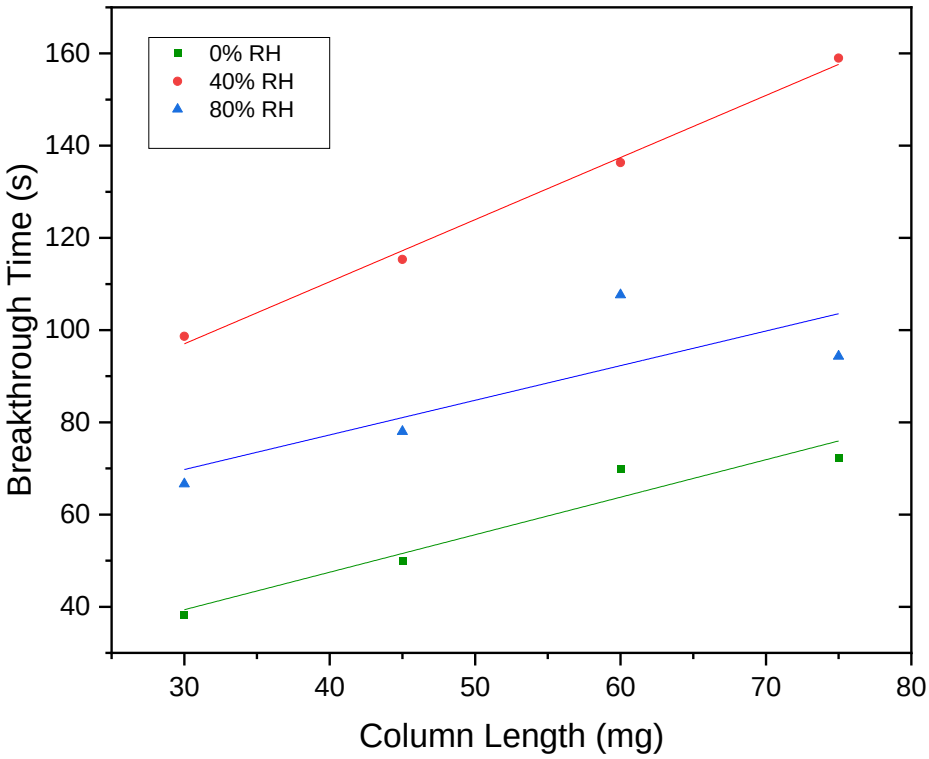

Figure 7.3. 50% Breakthrough Times for formaldehyde at 0%, 40%, and 80% RH values with various column lengths

Table 7.1. Corroboration of Breakthrough Times for Formaldehyde at 0%, 40%, and 80% RH values with column lengths of 30 mg, 45 mg, 60 mg, and 75 mg

Analyte	Mass of sorbent (mg)	50% Breakthrough Time (s) at 0% RH	50% Breakthrough Time (s) at 40% RH	50% Breakthrough Time (s) at 80% RH
CH_2O	30	38	98	66
CH_2O	45	50	115	78
CH_2O	60	77	136	107
CH_2O	75	72	159	94

The data reveals the lowest recorded breakthrough times for formaldehyde were tested under 0% RH conditions. Typically, water vapor is adsorbed by polar sorbents and their breakthrough capacity is reduced for most organic compounds. High RH can block the available pores for VOC exposure and reduce the adsorption capacity for non-water-soluble compounds.

However, the breakthrough capacity for water-soluble compounds (formaldehyde) increases in the presence of humidity. This could account for the low values associated with the 0% RH results. From the data, the samples tested under 40% and 80% RH showed promising sorption capacities. Previous research has shown that the optimum relative humidity for sampling formaldehyde was 50%, where lower RH resulted in lower capacities due to less adsorbed moisture for adsorbing formaldehyde.[54]

The breakthrough times for acetaldehyde are shown below in Figure VI-8 and are quantified in Table VI-3. Contrary to the formaldehyde data the breakthrough times increased by reducing the RH levels. The columns tested under 0% RH had the longest breakthrough times because the acetaldehyde could fully saturate on the surface of the sorbent. However, the columns tested under 80% RH has the quickest breakthrough times.

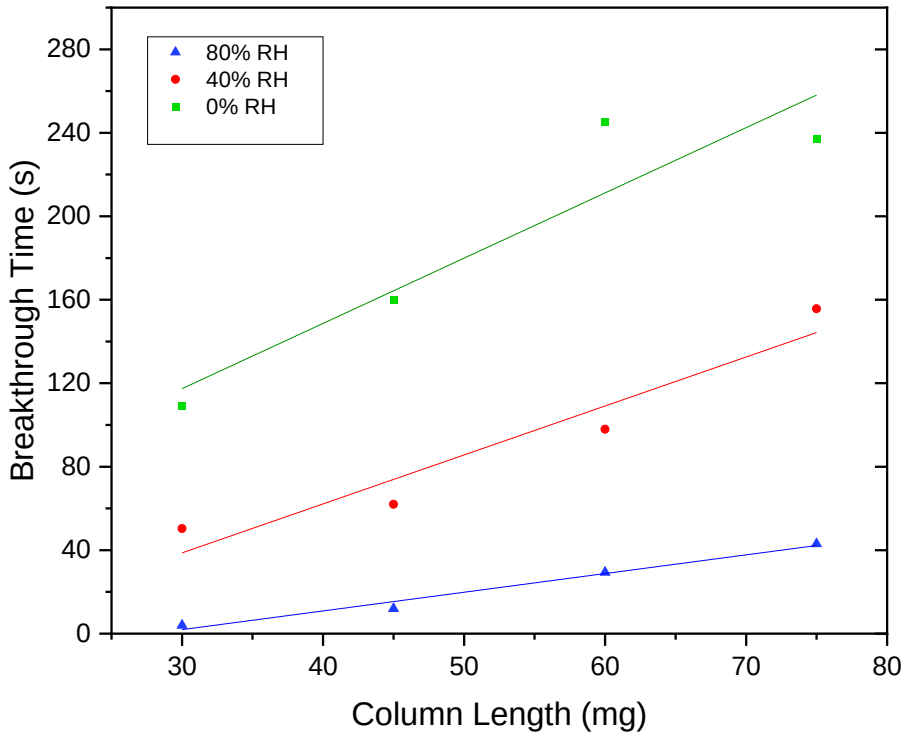

Figure 7.4. 50% Breakthrough Times for Acetaldehyde at 0%, 40%, and 80% RH values with various column lengths

Table 7.2. Corroboration of Breakthrough Times for Acetaldehyde at 0%, 40%, and 80% RH values with column lengths of 30 mg, 45 mg, 60 mg, and 75 mg

Analyte	Mass of sorbent (mg)	50% Breakthrough Time (s) at 0% RH	50% Breakthrough Time (s) at 40% RH	50% Breakthrough Time (s) at 80% RH
C_2H_4O	30	109	50	4
C_2H_4O	45	160	62	12
C_2H_4O	60	245	98	29
C_2H_4O	75	237	155	43

It has been reported that at higher humidity's acetaldehyde adsorption is impeded by water molecules decreasing its hydrophobicity resulting in less adsorption. During the sampling

process, the accumulation of water vapor on the sorbent can outnumber the sampled aldehyde molecule by more than 1000%.[55, 56] This can cause the displacement of collected acetaldehyde with water molecules, which could led to premature breakthrough and sample loss.

2. Experimental Uptake

While breakthrough times were extracted from the breakthrough curve collected using the chemiresisitve sensor, the experimental uptake values were also determined for those experiments subsequently using the following formula. The values are quantified in Table VI-4.

$$Experimental\ Uptake = \frac{\left[breakthroughtime\ (min) \times \text{flow}\ \left(\frac{\text{L}}{min}\right) \times \text{analyte exposure concentration}\ \left(\frac{\text{mg}}{\text{L}}\right)\right]}{\text{mass of sorbent (g)}}$$

[Equation VI-4]

Table 7.3. Experimental Uptake Capacity Values for Formaldehyde and Acetaldehyde with column lengths of 30mg, 45mg, 60mg, and 75mg at relative humidity values of 0%, 40%, and 80%

Analyte	Mass of sorbent (mg)	Experimental uptake capacity (mg/g) at 0% RH	Experimental uptake capacity (mg/g) at 40% RH	Experimental uptake capacity (mg/g) at 80% RH
CH_2O	30	0.010	0.027	0.018
CH_2O	45	0.009	0.021	0.014
CH_2O	60	0.010	0.018	0.014
CH_2O	75	0.008	0.017	0.010

Analyte	Mass of sorbent (mg)	Experimental uptake capacity (mg/g) at 0% RH	Experimental uptake capacity (mg/g) at 40% RH	Experimental uptake capacity (mg/g) at 80% RH
C_2H_4O	30	0.030	0.013	0.001
C_2H_4O	45	0.029	0.011	0.002
C_2H_4O	60	0.034	0.013	0.004
C_2H_4O	75	0.026	0.017	0.004

3. Conclusion

Although the uptake capacity for formaldehyde at 0% RH was anomalous and was lower when compared to the other two relative humidity's, the sorbent still showed significant adsorption capabilities. From this study and previous research, it is clear that for adsorption to take place with formaldehyde the sampling must be conducted with at least 40% RH. The uptake capacities for acetaldehyde were highest when measured with 0% RH. However, similar to the formaldehyde experiments significant adsorption was observed at 40% RH.

The experimental uptake values for each column length represented a linear relationship which is necessary for effective adsorbates. The capacity per gram was the same for each column length with the standard deviations represented in Table 6.5 below. This indicates that the OSU-6 is acting as a true adsorbent where its relationship with mass and uptake capacity is linear.

Table 7.4. Average uptake capacity for acetaldehyde and formaldehyde

Analyte	Experimental uptake capacity (mg/g) at 0% RH	Experimental uptake capacity (mg/g) at 40% RH	Experimental uptake capacity (mg/g) at 80% RH
CH_2O	0.009 (±0.0008)	0.020 (±0.003)	0.014 (±0.002)
C_2H_4O	0.029 (±0.002)	0.013 (±0.002)	0.011 (±0.001)

Typically, breakthrough volume experiments are conducted at 0% RH, this is a point of contention because the environment where these pollutants are present will usually have some level of humidity present. The breakthrough volume performance of the OSU-6 sorbent in the 40% RH conditions demonstrates its ability to be used in active sampling in operating conditions of a workplace, house, or school. [57]

CHAPTER VIII

ACTIVE ALDEHYDE SAMPLING WITH OSU-6

1. Active Sampling Test Method

The OSU-6 (40/60 mesh) was packed into a Markes' industry-standard thermal desorption tube with an 8.9-cm length and 4-mm internal diameter. The two ends of the tube were sealed using a small piece of glass wool and secured with a metal spring to withstand the high flow of gases. Prior to breakthrough analysis, the packed sorbent tubes were conditioned in a Markes' TC-20 tube conditioner. The tubes were loaded into the conditioner and heated under a flow of research plus nitrogen gas at 180° C for 2 hours.

A benchtop sampling apparatus was constructed to generate precise gas concentrations. Air is passed through a humidification module which is controlled by a Dakota Instruments mass flow controller (± 1%) varying the flow rate based on the target RH. The tested RH values were 0%, 40%, and 80%. To ensure the sorbent has fully saturated the humidity inside the analysis chamber was monitored using an Omega USB-RH Sensor (±3%). Once the humidity levels stabilized, zero-grade air was passed over the sorbent for 1 hour. Zero-grade air was employed as the carrier gas for the target analyte, this was controlled through two mass-flow controllers.

The total flow rate was held at 50 mL/min with the formaldehyde concentration at 0.5 ppm (lower than OSHA exposure limits). The use of an automatic switch was employed to mitigate a spike in resistance that occurs at the onset of the experiment and minimize error with breakthrough times.

2. Thermal Desorption-GC(MS)

The sampling tubes were prepared using a standard stainless steel thermal desorption tube(8.9-cm length and 4-mm internal diameter, and 6-mm outer diameter). The design of this tube allows for thermal desorption to occur inside the GC injector by interchanging the GC injector inlet with the sample tube. Each prepared sample was packed with 30 mg of fresh OSU-6 (40/60 mesh). Prior to analyte exposure, the tubes were conditioned in a Markes TC-20 tube conditioner. The tubes were loaded into the conditioner and heated under a flow of research plus nitrogen gas at 180 ° C for 2 hours.

Following conditioning, the tubes were exposed 400 ppm of the analyte for 3,6,9, and 12 minutes for acetaldehyde and 5,10,15 minutes for formaldehyde under 0% RH and 40% RH conditions. The samples were collected at a flow rate of 10 mL/min controlled by two Dakota Instruments mass flow controllers (± 1%). The target RH level was achieved by varying the amount of air flowing through the humidity module that was connected to the sampling tube.

Analysis was performed by gas chromatography/mass spectrometry (GC(MS)) coupled with thermal desorption (TD) using a Markes TD-100 connected to an Agilent GC(MS). The TD instrument was used to thermally desorb the aldehydes within the sorbent tube following exposure. The desorption experiments took place at 150 ° C using helium at a flow rate of 210 mL/min for 5 minutes. A cold trap (U-T11GPC-25 or U-T12ME-2S) was used to condense the desorbed vapors, this flushed with helium for 1 minute at a rate of 20 mL/min at -10 ° C. The trap was then ramped to 280 °C for several seconds at 10mL/min and then held at the final

temperature for 3 minutes. To further dilute the output of the cold trap a split flow of 200 mL/min was used. The desorbed analytes were then injected into the GC column with a column flow of 2 mL/min. The chromatographs were recorded using a GC (Agilent 6890 equipped with a 30 m × 0.25 mm DB-5MS column) and a mass spectrometer (Agilent 5973N). Under a flow of helium, calibration standards were made using Markes thermal desorption tubes, and their solution calibration loading apparatus.

3. Formaldehyde Quantification Method

Before GC(MS) quantification for the formaldehyde samples, they must undergo desorption onto a DNPH-coated silica gel tube. This was conducted under a predetermined sampling rate (10 ml/min) for 5,10-, and 15-minute exposure time. Once sampled on the OSU-6 the tubes are desorbed onto the DNPH coated Tenax tubes. Following this step, the amount of formaldehyde can properly be quantified using GC(MS). A representative chromatograph is shown below in Figure 8.1.

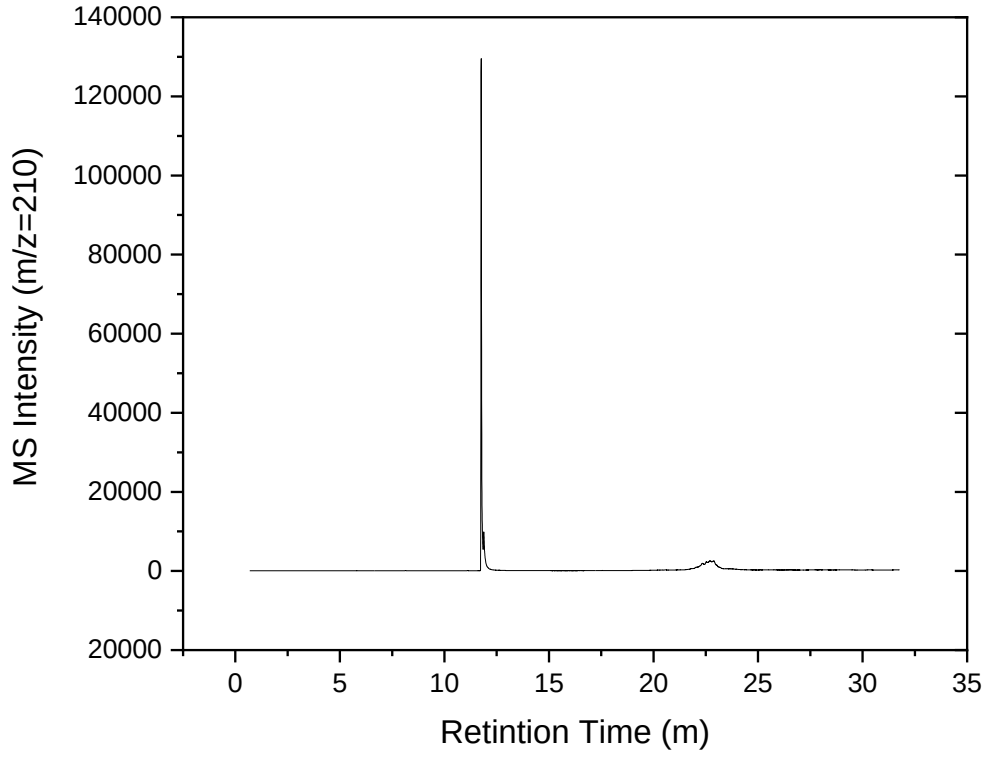

Figure 8.1 Formaldehyde chromatograph from TD-GC(MS) from DNPH functionalized tube

The adsorption on the OSU-6 matrix was verified by thermal desorption combined with GC(MS). The obtained results confirmed the capability of OSU-6 sorbent to effectively sample formaldehyde under various conditions. The results are shown below as a function of time vs. thermal desorption intensity.

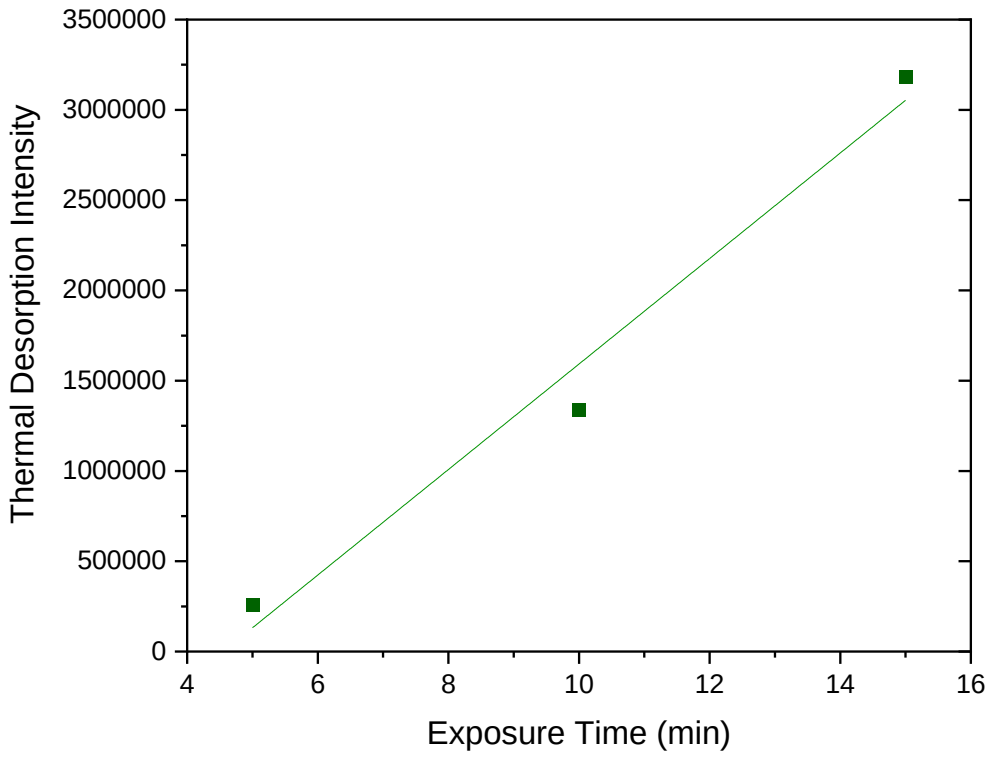

Figure 8.2 Linear plot of formaldehyde exposure time and thermal desorption intensity

From Figure 8.2 we can see that OSU-6 was able to quantify formaldehyde even at low concentrations. This becomes important for active sampling, especially a compound like formaldehyde, because even at low concentrations serious health effects are observed.

4. Acetaldehyde Quantification

Acetaldehyde can directly be observed with TD-GC(MS) so the intermediate step which is used for formaldehyde quantification can be removed. The sampled analyte was directly desorbed and transferred to the GC(MS); a representative chromatograph is shown below in Figure 8.3.

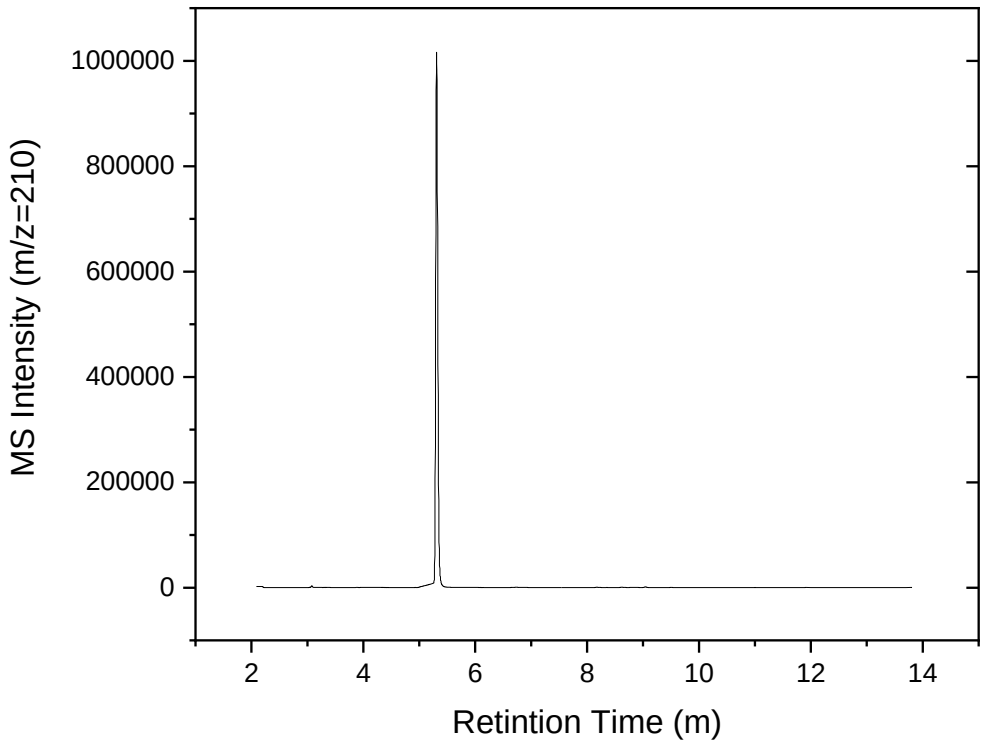

Figure 8.3. Acetaldehyde chromatograph from TD-GC(MS) from OSU-6 sampling tube

The sampling tubes were loaded with acetaldehyde (10 ml/min) for various times and the concentrations were observed as a function of time and thermal desorption intensity, the results for acetaldehyde quantification are shown in Figure 8.4.

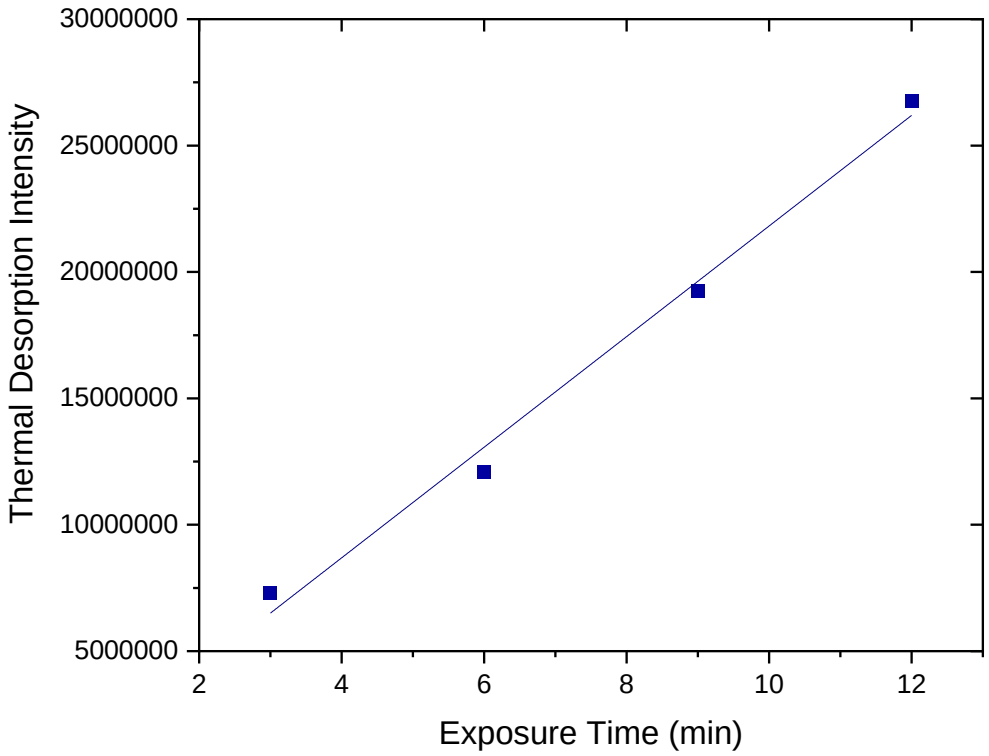

Figure 8.4. Linear plot of acetaldehyde exposure time and thermal desorption intensity

From the two plots a linear relationship between exposure time and thermal desorption intensity is observed. This indicates that the OSU-6 sorbent is successfully capturing the analyte and subsequent desorption for quantification is achieved even at low concentrations. This sorbent material was used at various column lengths and relative humidity levels, and still showed high sorption capacities. The use of this new material can be integrated into traditional active sampling methods for reactive carbonyl compounds. In addition, the new breakthrough determination method can be a quick and easy low-cost solution to traditional offline methods that are currently being employed.

CHAPTER IX

CONCLUSION

In Part 1, XPS was used to characterize binding configurations of multi-junction solar cells in order to determine if nitrogen defects were passivated after annealing and hydrogenation treatments. The GaInNAs materials were evaluated extensively undergoing multiple chemical surface treatments and depth profiling via ion beam sputtering (Chapter II). The initial spectra revealed an unknown peak in the nitrogen associated region, which led us to acquire a set of pure semiconducting samples (InGaAs, InAs, GaAs, GaP, and GaN) to help with understanding the N 1s results in Chapter III.

The pure samples (GaAs and GaN) confirmed the peak that was observed in the GaInNAs materials that had yet to be reference in the literature. The focus of the project was now on identifying this peak in the nitrogen region. The pure samples of GaAs and GaN both revealed the same feature with the same characteristics. This is leading us to believe that the peak is associated with interstitial nitrogen in the lattice due to its high binding energy (410eV). The nitrogen associated region was studied extensively to ensure the binding energy was accurately assigned and the peak was reproducible.

After studying multiple variations of these materials, we have concluded that this unidentified peak is a form of interstitial nitrogen in the lattice. The high binding energy of this peak and its intensification after nitrogen ion implantation leads us to this conclusion. The future direction of

this project will be to perform DFT calculations on these binding energies in order to determine with geometries provide the XPS peak at the experimental location.

In Part 2, a new sorbent material for capturing highly reactive compounds was studied for its use in active sampling. With an increase in anthropogenic sources of VOCs urbanized areas are becoming more susceptible to high concentrations and exposure to these toxic compounds that can have adverse effects on human health. Among these known pollutants, a interest in sampling low molecular weight aldehydes is important due to their carcinogenic nature even at low concentrations.

A nanoporous silica sorbent named OSU-6 was explored in this study for its use in acetaldehyde and formaldehyde sampling followed by thermal desorption and gas chromatography/mass spectrometry (TD-GC/MS) analysis (Chapter VI). The use of this material will mitigate problems that arise during sampling with the use of nanoconfinement technology which stabilizes reactive organic compounds. A series of analyses were performed to determine the material's sorption capacity in a variety of sampling conditions. Following the breakthrough determination, the concentrations were quantified (Chapter VII) using thermal desorption-gas chromatography/mass spectrometry (TD-GC/MS).

From these experiments, we have determined that OSU-6 sorbent is an excellent sorbent material for capturing and desorbing low molecular weight aldehydes. From various test conditions we have concluded that this material has successfully captured these compounds even at low concentrations and high relative humidity environments. The nanoconfinement technology and the materials interness allows it to successfully capture these compounds without reacting and forming secondary products. Following a subsequent analysis step, the OSU-6 sorbent was able to release the compounds using thermal desorption where it was then quantified with GC(MS).

The formaldehyde was effectively quantified using a new 2-step method in which it was captured using the OSU-6 sorbent and desorbed onto a DNPH coated tube. This allowed for GC(MS) determination of the formaldehyde concentrations. These features make OSU-6 a candidate for active sampling in a variety of conditions, along with a new uptake capacity determination method.

REFERENCES

1. Babic, R. R.; Stankovic Babic, G.; Babic, S. R.; Babic, N. R., 120 YEARS SINCE THE DISCOVERY OF X-RAYS. *Medicinski pregled* **2016,** *69* (9-10), 323-330.

2. Innes, P. D.; Thomson, J. J., On the velocity of the cathode particles emitted by various metals under the influence of Röntgen rays, and its bearing on the theory of atomic disintegration. **1907,** *79* (532), 442-462.

3. Alov, N. V., Fifty years of X-ray photoelectron spectroscopy. *Journal of Analytical Chemistry* **2005,** *60* (3), 297-300.

4. Nordling, C.; Sokolowski, E.; Siegbahn, K., Precision Method for Obtaining Absolute Values of Atomic Binding Energies. *Physical Review* **1957,** *105* (5), 1676-1677.

5. Ossiander, M.; Riemensberger, J.; Neppl, S.; Mittermair, M.; Schäffer, M.; Duensing, A.; Wagner, M. S.; Heider, R.; Wurzer, M.; Gerl, M.; Schnitzenbaumer, M.; Barth, J. V.; Libisch, F.; Lemell, C.; Burgdörfer, J.; Feulner, P.; Kienberger, R., Absolute timing of the photoelectric effect. *Nature* **2018,** *561* (7723), 374-377.

6. Hantsche, H., Comparison of basic principles of the surface-specific analytical methods: AES/SAM, ESCA (XPS), SIMS, and ISS with X-ray microanalysis, and some applications in research and industry. **1989,** *11* (6), 257-280.

7. Yamamoto, S.; Yokogawa, H.; Hashimoto, H., Cylindrical Mirror Analyzer for Measuring Energy Spectrum of Photostimulated Exoelectrons. *Japanese Journal of Applied Physics* **1985,** *24* (S4), 281.

8. Lefebvre, J.; Galli, F.; Bianchi, C. L.; Patience, G. S.; Boffito, D. C., Experimental methods in chemical engineering: X-ray photoelectron spectroscopy-XPS. **2019,** *97* (10), 2588-2593.

9. Payne, B. P.; Keech, P. G.; McIntyre, N. S. In *X-ray Photoelectron Study of the Oxides Formed on Nickel Metal and Nickel-Chromium 20% Alloy Surfaces Under Reducing and Oxidizing Potentials in Basic, Neutral and Acidic Solutions*, Cham, Springer International Publishing: Cham, 2016; pp 1065-1085.

10. Siegbahn, K. In *Electron Spectroscopy for Chemical Analysis*, Boston, MA, Springer US: Boston, MA, 1973; pp 493-522.

11. Cazaux, J., About the charge compensation of insulating samples in XPS. *Journal of Electron Spectroscopy and Related Phenomena* **2000,** *113* (1), 15-33.

12. Metson, J. B., Charge compensation and binding energy referencing in XPS analysis. **1999,** *27* (12), 1069-1072.

13. Briggs, D., Handbook of X-ray Photoelectron Spectroscopy C. D. Wanger, W. M. Riggs, L. E. Davis, J. F. Moulder and G. E.Muilenberg Perkin-Elmer Corp., Physical Electronics Division, Eden Prairie, Minnesota, USA, 1979. 190 pp. $195. **1981,** *3* (4), v-v.

14. Shard, A. G., Practical guides for X-ray photoelectron spectroscopy: Quantitative XPS. **2020,** *38* (4), 041201.

15. Shirley, D. A., High-Resolution X-ray Photoemission Spectrum of the Valence Bands of Gold. *Physical Review B* **1972,** *5* (12), 4709-4714.

16. Tougaard, S., Practical algorithm for background subtraction. *Surface Science* **1989,** *216* (3), 343-360.

17. Cumpson, P. J., Angle-resolved XPS and AES: Depth-resolution limits and a general comparison of properties of depth-profile reconstruction methods. *Journal of Electron Spectroscopy and Related Phenomena* **1995,** *73* (1), 25-52.

18. Lam, N. Q., Ion bombardment effects on the near-surface composition during sputter profiling. **1988,** *12* (2), 65-77.

19. Oswald, S.; Reiche, R., Binding state information from XPS depth profiling: Capabilities and limits. *Applied Surface Science* **2001,** *179*, 307-315.

20. Seah, M. P., Universal Equation for Argon Gas Cluster Sputtering Yields. *The Journal of Physical Chemistry C* **2013,** *117* (24), 12622-12632.

21. Brown, C. R.; Estes, N. J.; Whiteside, V. R.; Wang, B.; Hossain, K.; Golding, T. D.; Leroux, M.; Al Khalfioui, M.; Tischler, J. G.; Ellis, C. T.; Glaser, E. R.; Sellers, I. R., The effect and nature of N–H complexes in the control of the dominant photoluminescence transitions in UV-hydrogenated GaInNAs. *RSC Advances* **2017,** *7* (41), 25353-25361.

22. Bank, S. R.; Yuen, H. B.; Bae, H.; Wistey, M. A.; Jr., J. S. H., Overannealing effects in GaInNAs(Sb) alloys and their importance to laser applications. *Applied Physics Letters* **2006,** *88* (22), 221115.

23. Seah, M. P., Summary of ISO/TC 201 Standard: ISO 14701:2011 – Surface chemical analysis – X-ray photoelectron spectroscopy—measurement of silicon oxide thickness. *Surface and Interface Analysis* **2012,** *44* (7), 876-878.

24. Greczynski, G.; Hultman, L., X-ray photoelectron spectroscopy: Towards reliable binding energy referencing. *Progress in Materials Science* **2020,** *107*, 100591.

25. Helander, M. G.; Greiner, M. T.; Wang, Z. B.; Lu, Z. H., Note: Binding energy scale calibration of electron spectrometers for photoelectron spectroscopy using a single sample. *Review of Scientific Instruments* **2011,** *82* (9), 096107.

26. Lebedev, M. V.; Mankel, E.; Mayer, T.; Jaegermann, W., Wet Etching of GaAs(100) in Acidic and Basic Solutions: A Synchrotron−Photoemission Spectroscopy Study. *The Journal of Physical Chemistry C* **2008,** *112* (47), 18510-18515.

27. DeSalvo, G. C.; Bozada, C. A.; Ebel, J. L.; Look, D. C.; Barrette, J. P.; Cerny, C. L. A.; Dettmer, R. W.; Gillespie, J. K.; Havasy, C. K.; Jenkins, T. J.; Nakano, K.; Pettiford, C. I.; Quach, T. K.; Sewell, J. S.; Via, G. D., Wet Chemical Digital Etching of GaAs at Room Temperature. *Journal of The Electrochemical Society* **2019,** *143* (11), 3652-3656.

28. Molnar, R. J.; Maki, P.; Aggarwal, R.; Liau, Z. L.; Brown, E. R.; Melngailis, I.; Götz, W.; Romano, L. T.; Johnson, N. M., Gallium Nitride Thick Films Grown by Hydride Vapor Phase Epitaxy. *MRS Online Proceedings Library* **1996,** *423* (1), 221-226.

29. Akindoyo, J. O.; Beg, M. D. H.; Ghazali, S.; Islam, M. R.; Jeyaratnam, N.; Yuvaraj, A. R., Polyurethane types, synthesis and applications – a review. *RSC Advances* **2016,** *6* (115), 114453-114482.

30. Xiao, H.-D.; Ma, H.-L.; Xue, C.-S.; Zhuang, H.-Z.; Ma, J.; Zong, F.-J.; Zhang, X.-J., Synthesis and structural properties of beta-gallium oxide particles from gallium nitride powder. *Materials Chemistry and Physics* **2007,** *101* (1), 99-102.

31. Wolter, S. D.; Luther, B. P.; Waltemyer, D. L.; Önneby, C.; Mohney, S. E.; Molnar, R. J., X-ray photoelectron spectroscopy and X-ray diffraction study of the thermal oxide on gallium nitride. **1997,** *70* (16), 2156-2158.

32. Chen, P.; Zhang, R.; Xu, X. F.; Zhou, Y. G.; Chen, Z. Z.; Xie, S. Y.; Li, W. P.; Zheng, Y. D., The oxidation of gallium nitride epilayers in dry oxygen. *Applied Physics A* **2000,** *71* (2), 191-194.

33. Howes, M. J.; Morgan, D. V., *Gallium arsenide: Materials, devices, and circuits*. 1985.

34. Lay, T. S.; Kuo, W. T.; Chen, L. P.; Lai, Y. H.; Hung, W. H.; Wang, J. S.; Chi, J. Y.; Shih, D. K.; Lin, H. H., Probing the electronic structures of III–V-nitride semiconductors by X-ray photoelectron spectroscopy. **2004,** *22* (3), 1491-1494.

35. Zeng, Y.-J.; Ye, Z.-Z.; Lu, J.-G.; Zhu, L.-P.; Li, D.-Y.; Zhao, B.-H.; Huang, J.-Y., Effects of Al content on properties of Al–N codoped ZnO films. *Applied Surface Science* **2005,** *249* (1), 203-207.

36. Cheung, S. H.; Nachimuthu, P.; Joly, A. G.; Engelhard, M. H.; Bowman, M. K.; Chambers, S. A., N incorporation and electronic structure in N-doped TiO2(110) rutile. *Surface Science* **2007,** *601* (7), 1754-1762.

37. Bian, J. M.; Li, X. M.; Gao, X. D.; Yu, W. D.; Chen, L. D., Deposition and electrical properties of N–In codoped p-type ZnO films by ultrasonic spray pyrolysis. **2004,** *84* (4), 541-543.

38. Ievtushenko, A. I.; Khyzhun, O.; Shtepliuk, I.; Tkach, V.; Lazorenko, V.; Lashkarev, G., X-ray Photoelectron Spectroscopy Study of Nitrogen and Aluminum-Nitrogen Doped ZnO Films. *Acta Physica Polonica Series a* **2013,** *124*, 858-861.

39. Chou, C.-Y.; Lin, C.-H.; Chen, W.-H.; Li, B.-J.; Liu, C.-Y., High-dielectric-constant silicon nitride thin films fabricated by radio frequency sputtering in Ar and Ar/N2 gas mixture. *Thin Solid Films* **2020,** *709*, 138198.

40. Lewin, E.; Counsell, J.; Patscheider, J., Spectral artefacts post sputter-etching and how to cope with them – A case study of XPS on nitride-based coatings using monoatomic and cluster ion beams. *Applied Surface Science* **2018,** *442*, 487-500.

41. Peng, F.; Cai, L.; Yu, H.; Wang, H.; Yang, J., Synthesis and characterization of substitutional and interstitial nitrogen-doped titanium dioxides with visible light photocatalytic activity. *Journal of Solid State Chemistry* **2008,** *181* (1), 130-136.

42. Pal, S.; Mahapatra, R.; Ray, S. K.; Chakraborty, B. R.; Shivaprasad, S. M.; Lahiri, S. K.; Bose, D. N., Microwave plasma oxidation of gallium nitride. *Thin Solid Films* **2003,** *425* (1), 20-23.

43. Watkins, N. J.; Wicks, G. W.; Gao, Y., Oxidation study of GaN using X-ray photoemission spectroscopy. **1999,** *75* (17), 2602-2604.

44. Kelly, R., Factors determining the compound phases formed by oxygen or nitrogen implantation in metals. *Journal of Vacuum Science and Technology* **1982,** *21* (3), 778-789.

45. DeLouise, L. A., Nitridation of GaAs(110) using energetic N+ and N+2 ion beams. *Journal of Vacuum Science & Technology A* **1993,** *11* (3), 609-614.

46. Hecht, J. D.; Frost, F.; Chassé, T.; Hirsch, D.; Neumann, H.; Schindler, A.; Bigl, F., In situ characterization of the nitridation of AIII–BV semiconductor surfaces by means of X-ray photoelectron spectroscopy. *Applied Surface Science* **2001,** *179* (1), 196-202.

47. Diwald, O.; Thompson, T. L.; Goralski, E. G.; Walck, S. D.; Yates, J. T., The Effect of Nitrogen Ion Implantation on the Photoactivity of TiO2 Rutile Single Crystals. *The Journal of Physical Chemistry B* **2004,** *108* (1), 52-57.

48. Kadowaki, M.; Saengdeejing, A.; Muto, I.; Chen, Y.; Frankel, G. S.; Doi, T.; Kawano, K.; Sugawara, Y.; Hara, N., Roles of Interstitial Nitrogen, Carbon, and Boron in Steel Corrosion: Generation of Oxyanions and Stabilization of Electronic Structure. *Journal of The Electrochemical Society* **2020,** *167* (8), 081503.

49. Rühle, S., Tabulated values of the Shockley–Queisser limit for single junction solar cells. *Solar Energy* **2016,** *130*, 139-147.

50. Yamaguchi, M.; Takamoto, T.; Araki, K.; Ekins-Daukes, N., Multi-junction III–V solar cells: current status and future potential. *Solar Energy* **2005,** *79* (1), 78-85.

51. Pavelescu, E.-M.; Wagner, J.; Komsa, H.-P.; Rantala, T. T.; Dumitrescu, M.; Pessa, M., Nitrogen incorporation into GaInNAs lattice-matched to GaAs: The effects of growth temperature and thermal annealing. **2005,** *98* (8), 083524.

52. Mintairov, A. M.; Sun, K.; Merz, J. L.; Yuen, H.; Bank, S.; Wistey, M.; Harris, J. S.; Peake, G.; Egorov, A.; Ustinov, V.; Kudrawiec, R.; Misiewicz, J., Atomic arrangement and emission properties of GaAs(In, Sb)N quantum wells. *Semiconductor Science and Technology* **2009,** *24* (7), 075013.

53. Janotti, A.; Zhang, S. B.; Wei, S.-H.; Van de Walle, C. G., Effects of Hydrogen on the Electronic Properties of Dilute GaAsN Alloys. *Physical Review Letters* **2002,** *89* (8), 086403.

54. Janotti, A.; Wei, S.-H.; Zhang, S. B.; Kurtz, S.; Van de Walle, C. G., Interactions between nitrogen, hydrogen, and gallium vacancies in ${\mathrm{GaAs}}_{1\ensuremath{-}x}{\mathrm{N}}_{x}$ alloys. *Physical Review B* **2003,** *67* (16), 161201.

55. Gabás, M.; Lopez-Escalante, M. C.; Algora, C.; Rey-Stolle, I.; Galiana, B.; Palanco, S.; Barrado, J., *ARXPS analysis of a GaAs/GaInP heterointerface with application in III–V multijunction solar cells*. 2012; p 000385-000389.

56. Gabás, M.; Lopez-Escalante, M.; Algora, C.; Rey-Stolle, I.; Barrigon, E.; Garcia, I.; Galiana, B.; Palanco, S.; Bijani, S.; Barrado, J., XPS as characterization tool for PV: From the substrate to complete III-V multijunction solar cells. *Conference Record of the IEEE Photovoltaic Specialists Conference* **2011**, 001711-001715.

57. Foley, C. P.; Lyngdal, J., Analysis of indium nitride surface oxidation. **1987,** *5* (4), 1708-1712.

58. Deminskyi, P.; Pedersen, H., Atomic layer deposition of InN using trimethylindium and ammonia plasma. *Journal of Vacuum Science and Technology* **2019,** *37*, 020926.

59. Wagner, C. D.; Muilenberg, G. E., *Handbook of X-ray Photoelectron Spectroscopy: A Reference Book of Standard Data for Use in X-ray Photoelectron Spectroscopy*. Perkin-Elmer: 1979.

60. Hoshii, T.; Yokoyama, M.; Yamada, H.; Hata, M.; Yasuda, T.; Takenaka, M.; Takagi, S., Impact of InGaAs surface nitridation on interface properties of InGaAs metal-oxide-semiconductor capacitors using electron cyclotron resonance plasma sputtering SiO2. **2010,** *97* (13), 132102.

61. Feng, L.; Zhang, L.-d.; Liu, H.; Gao, X.; Miao, Z.; Cheng, H.-c.; Wang, L.; Niu, S., *Characterization study of native oxides on GaAs(100) surface by XPS*. SPIE: 2013; Vol. 8912.

62. Kumar, M.; Bhat, T.; Rajpalke, M.; Roul, B.; Misra, P.; Kukreja, L.; Sinha, N.; Kalghatgi, A.; Krupanidhi, S., Self-assembled flower-like nanostructures of InN and GaN grown by plasma-assisted molecular beam epitaxy. *Bulletin of Materials Science* **2010,** *33*, 221-226.

63. Zhang, C. G.; Chen, W. D.; Bian, L. F.; Song, S. F.; Hsu, C. C., Preparation and characterization of GaN films by radio frequency magnetron sputtering and carbonized-reaction technique. *Applied Surface Science* **2006,** *252* (6), 2153-2158.

64. Grodzicki, M.; Rousset, J. G.; Ciechanowicz, P.; Piskorska-Hommel, E.; Hommel, D., XPS studies on the role of arsenic incorporated into GaN. *Vacuum* **2019,** *167*, 73-76.

65. Bertóti, I., Characterization of nitride coatings by XPS. *Surface and Coatings Technology* **2002,** *151-152*, 194-203.

66. Zhang, S. B.; Wei, S. H., Nitrogen solubility and induced defect complexes in epitaxial GaAs:N. *Phys Rev Lett* **2001,** *86* (9), 1789-92.

67. Ahlgren, T.; Vainonen-Ahlgren, E.; Likonen, J.; Li, W.; Pessa, M., Concentration of interstitial and substitutional nitrogen in GaNxAs1−x. *Applied Physics Letters* **2002,** *80* (13), 2314-2316.

68. Bösker, G.; Stolwijk, N. A.; Thordson, J. V.; Södervall, U.; Andersson, T. G., Diffusion of Nitrogen from a Buried Doping Layer in Gallium Arsenide Revealing the Prominent Role of As Interstitials. *Physical Review Letters* **1998,** *81* (16), 3443-3446.

69. Petravic, M.; Deenapanray, P. N. K.; Coleman, V. A.; Kim, K.-j.; Kim, B.; Li, G., Core-level photoemission and near-edge X-ray absorption fine-structure studies of GaN surface under low-energy ion bombardment. *Journal of Applied Physics* **2004,** *95* (10), 5487-5493.

70. Li, W.; Pessa, M.; Likonen, J., Lattice parameter in GaNAs epilayers on GaAs: Deviation from Vegard's law. *Applied Physics Letters* **2001,** *78* (19), 2864-2866.

71. Laaksonen, K.; Komsa, H. P.; Rantala, T.; Nieminen, R., Nitrogen interstitial defects in GaAs. *Journal of physics. Condensed matter : an Institute of Physics journal* **2008,** *20*, 235231.

72. Carrier, P.; Wei,S.; Zhang, S. B.; Kurtz, S., Evolution of structural properties and formation of N-N split interstitials in GaAs1−xNx alloys. *Physical Review B* **2005,** 71, 165212.

PART II References

1. Li, W. B.; Wang, J. X.; Gong, H., Catalytic combustion of VOCs on non-noble metal catalysts. Catalysis Today 2009, 148 (1), 81-87.

2. Ortiz, A.; Guerreiro, C.; de Leeuw, F.; Horálek, J., Air Quality in Europe - 2017 report. 2017.

3. Okada, Y.; Nakagoshi, A.; Tsurukawa, M.; Matsumura, C.; Eiho, J.; Nakano, T., Environmental risk assessment and concentration trend of atmospheric volatile organic compounds in Hyogo Prefecture, Japan. Environ Sci Pollut Res Int 2012, 19 (1), 201-13.

4. Magnusson, R.; Nilsson, C.; Andersson, B., Emissions of aldehydes and ketones from a two-stroke engine using ethanol and ethanol-blended gasoline as fuel. Environ Sci Technol 2002, 36 (8), 1656-64.

5. Ho, S. S.; Ip, H. S.; Ho, K. F.; Ng, L. P.; Chan, C. S.; Dai, W. T.; Cao, J. J., Hazardous airborne carbonyls emissions in industrial workplaces in China. J Air Waste Manag Assoc 2013, 63 (7), 864-77.

6. Pala, M.; Ugolini, D.; Ceppi, M.; Rizzo, F.; Maiorana, L.; Bolognesi, C.; Schilirò, T.; Gilli, G.; Bigatti, P.; Bono, R.; Vecchio, D., Occupational exposure to formaldehyde and biological monitoring of Research Institute workers. Cancer Detect Prev 2008, 32 (2), 121-6.

7. O'Brien, P. J.; Siraki, A. G.; Shangari, N., Aldehyde sources, metabolism, molecular toxicity mechanisms, and possible effects on human health. Crit Rev Toxicol 2005, 35 (7), 609-62.

8. Feron, V. J.; Til, H. P.; de Vrijer, F.; Woutersen, R. A.; Cassee, F. R.; van Bladeren, P. J., Aldehydes: occurrence, carcinogenic potential, mechanism of action and risk assessment. Mutation Research/Genetic Toxicology 1991, 259 (3), 363-385.

9. Zhang, J.; Lioy, P. J.; He, Q., Characteristics of aldehydes: concentrations, sources, and exposures for indoor and outdoor residential microenvironments. Environ Sci Technol 1994, 28 (1), 146-52.

10. Balakrishnan, K.; Ramaswamy, P.; Sankar, S., Biomass Smoke and Health Risks – The Situation in Developing Countries. In Air Pollution: Indoor Air Pollution, Pluschke, P., Ed. Springer Berlin Heidelberg: Berlin, Heidelberg, 2004; pp 219-239.

11. Burge, P. S., Sick building syndrome. 2004, 61 (2), 185-190.

12. Mallawarachchi, H.; Silva, L., Green Framework to Improve Indoor Air Quality in Buildings. 2012.

13. Fiedler, N.; Laumbach, R.; Kelly-McNeil, K.; Lioy, P.; Fan, Z. H.; Zhang, J.; Ottenweller, J.; Ohman-Strickland, P.; Kipen, H., Health effects of a mixture of indoor air volatile organics, their ozone oxidation products, and stress. Environ Health Perspect 2005, 113 (11), 1542-8.

14. Jerrett, M.; Arain, A.; Kanaroglou, P.; Beckerman, B.; Potoglou, D.; Sahsuvaroglu, T.; Morrison, J.; Giovis, C., A review and evaluation of intraurban air pollution exposure models. Journal of Exposure Science & Environmental Epidemiology 2005, 15 (2), 185-204.

15. Spinelle, L.; Gerboles, M.; Kok, G.; Persijn, S.; Sauerwald, T., Review of Portable and Low-Cost Sensors for the Ambient Air Monitoring of Benzene and Other Volatile Organic Compounds. Sensors (Basel) 2017, 17 (7), 1520.

16. Kumar, A.; Víden, I., Volatile organic compounds: sampling methods and their worldwide profile in ambient air. Environ Monit Assess 2007, 131 (1-3), 301-21.

17. Rudolph, J.; Müller, K. P.; Koppmann, R., Sampling of organic volatiles in the atmosphere at moderate and low pollution levels. Analytica Chimica Acta 1990, 236, 197-211.

18. De Bortoli, M.; Knöppel, H.; Pecchio, E.; Schauenburg, H.; Vissers, H., Comparison Of Tenax And Carbotrap For VOC Sampling In Indoor Air. Indoor Air 1992, 2 (4), 216-224.

19. Peng, C. Y.; Batterman, S., Performance evaluation of a sorbent tube sampling method using short path thermal desorption for volatile organic compounds. J Environ Monit 2000, 2 (4), 313-24.

20. Cal, M. P.; Rood, M. J.; Larson, S. M., Removal of VOCs from humidified gas streams using activated carbon cloth. Gas Separation & Purification 1996, 10 (2), 117-121.

21. Li, L.; Sun, Z.; Li, H.; Keener, T. C., Effects of activated carbon surface properties on the adsorption of volatile organic compounds. Journal of the Air & Waste Management Association 2012, 62 (10), 1196-1202.

22. Kroupa, A.; Dewulf, J.; Van Langenhove, H.; Víden, I., Breakthrough characteristics of volatile organic compounds in the -10 to + 170 degrees C temperature range on Tenax TA determined by microtrap technology. Journal of chromatography. A 2004, 1038 (1-2), 215-223.

23. Harper, M.; Purnell, C. J., Diffusive Sampling — A Review. American Industrial Hygiene Association Journal 1987, 48 (3), 214-218.

24. Brown, R. H.; Purnell, C. J., Collection and analysis of trace organic vapour pollutants in ambient atmospheres: The performance of a Tenax-GC adsorbent tube. Journal of Chromatography A 1979, 178 (1), 79-90.

25. Ventura, K.; Příhoda, P.; Churáček, J., Application of solid sorbents to the trace analysis of alkyl esters of acrylic acid in air. Journal of Chromatography A 1995, 710 (1), 167-173.

26. Van Der Straeten, D.; Van Langenhove, H.; Schamp, N., Comparison between theoretical and experimental sampling efficiencies on Tenax GC. Journal of Chromatography A 1985, 331, 207-218.

27. Liška, I.; Kuthan, A.; Krupčík, J., Comparison of sorbents for solid-phase extraction of polar compounds from water. Journal of Chromatography A 1990, 509 (1), 123-134.

28. Bidleman, T. F.; Simon, C. G.; Burdick, N. F.; You, F., Theoretical plate measurements and collection efficiencies for high-volume air samplers using polyurethane foam. Journal of Chromatography A 1984, 301, 448-453.

29. Kephalopoulos, S.; Kotzias, D. D.; Kimmo, K.; Carslaw, N.; Paolo, C.; Fossati, S.; Hoffmann, T.; Langer, S.; Larsen, B.; Monn, C.; Nicolas, M.; Salthammer, T.; Schlitt, C.; Richard, W.; Wolkoff, P., EUROPEAN COLLABORATIVE ACTION Impact of Ozone-initiated Terpene Chemistry on Indoor Air Quality and Human Health. Report No 26. 2007.

30. Wolkoff, P., Some guides for measurements of volatile organic compounds indoors. Environmental Technology 1990, 11 (4), 339-344.

31. Idris, S.; Robertson, C.; Morris, M.; Gibson, L., A comparative study of selected sorbents for sampling of aromatic VOCs from indoor air. Anal. Methods 2010, 2, 1803-1809.

32. Zhu, L.; Shen, D.; Luo, K. H., A critical review on VOCs adsorption by different porous materials: Species, mechanisms and modification methods. Journal of Hazardous Materials 2020, 389, 122102.

33. Gallego, E.; Roca, F. J.; Perales, J. F.; Guardino, X., Comparative study of the adsorption performance of an active multi-sorbent bed tube (Carbotrap, Carbopack X, Carboxen 569) and a Radiello(®) diffusive sampler for the analysis of VOCs. Talanta 2011, 85 (1), 662-72.

34. Woolfenden, E., Sorbent-based sampling methods for volatile and semi-volatile organic compounds in air. Part 2. Sorbent selection and other aspects of optimizing air monitoring methods. J Chromatogr A 2010, 1217 (16), 2685-94.

35. Maier, I.; Fieber, M., Retention characteristics of volatile compounds on tenax TA. Journal of High Resolution Chromatography 1988, 11 (8), 566-576.

36. Woolfenden, E., Monitoring VOCs in Air Using Sorbent Tubes Followed by Thermal Desorption-Capillary GC Analysis: Summary of Data and Practical Guidelines. Journal of the Air & Waste Management Association 1997, 47 (1), 20-36.

37. Coffey, C.; LeBouf, R.; Lee, L.; Slaven, J.; Martin, S., Effect of Calibration and Environmental Condition on the Performance of Direct-Reading Organic Vapor Monitors. Journal of Occupational and Environmental Hygiene 2012, 9 (11), 670-680.

38. Di Renzo, F.; Cambon, H.; Dutartre, R., A 28-year-old synthesis of micelle-templated mesoporous silica. Microporous Materials 1997, 10 (4), 283-286.

39. Tsuneo, Y.; Toshio, S.; Kazuyuki, K.; Chuzo, K., The Preparation of Alkyltrimethylammonium–Kanemite Complexes and Their Conversion to Microporous Materials. Bulletin of the Chemical Society of Japan 1990, 63 (4), 988-992.

40. Hoffmann, F.; Cornelius, M.; Morell, J.; Fröba, M., Silica-based mesoporous organic-inorganic hybrid materials. Angew Chem Int Ed Engl 2006, 45 (20), 3216-51.

41. Bleloch, A.; F. G. Johnson, B.; V. Ley, S.; J. Price, A.; S. Shephard, D.; W. Thomas, A., Modified mesoporous silicate MCM-41 materials: immobilised perruthenate—a new highly active heterogeneous oxidation catalyst for clean organic synthesis using molecular oxygen. Chemical Communications 1999, (18), 1907-1908.

42. Vogel, M.; Büldt, A.; Karst, U., Hydrazine reagents as derivatizing agents in environmental analysis – a critical review. Fresenius' Journal of Analytical Chemistry 2000, 366 (8), 781-791.

43. Karst, U.; Binding, N.; Cammann, K.; Witting, U., Interferences of nitrogen dioxide in the determination of aldehydes and ketones by sampling on 2,4-dinitrophenylhydrazine-coated solid sorbent. Fresenius' Journal of Analytical Chemistry 1993, 345 (1), 48-52.

44. Tang, S.; Graham, L.; Shen, L.; Zhou, X.; Lanni, T., Simultaneous Determination of Carbonyls and NO2 in Exhausts of Heavy-Duty Diesel Trucks and Transit Buses by HPLC following 2,4-Dinitrophenylhydrazine Cartridge Collection. Environmental Science & Technology 2004, 38 (22), 5968-5976.

45. Herrington, J. S.; Fan, Z.-H.; Lioy, P. J.; Zhang, J., Low Acetaldehyde Collection Efficiencies for 24-Hour Sampling with 2,4-Dinitrophenylhydrazine (DNPH)-Coated Solid Sorbents. Environmental Science & Technology 2007, 41 (2), 580-585.

46. Apblett, A., PhD; Materer, N., PhD; Kadossov, E., PhD; Shaikh, S., MBA, Superior Monitoring of Chemical Exposure Using Nanoconfinement Technology. Military Medicine 2021, 186 (Supplement_1), 795-800.

47. Al Othman, Z. A.; Apblett, A. W., Synthesis and characterization of a hexagonal mesoporous silica with enhanced thermal and hydrothermal stabilities. Applied Surface Science 2010, 256 (11), 3573-3580.

48. Dollimore, D.; Spooner, P.; Turner, A., The bet method of analysis of gas adsorption data and its relevance to the calculation of surface areas. Surface Technology 1976, 4 (2), 121-160.

49. Sing, K. S. W.; Everett, D. H.; Haul, R. A. W.; Moscou, L.; Pierotti, R. A.; Rouquérol, J.; Siemieniewska, T., Reporting Physisorption Data for Gas/Solid Systems With Special Reference to the Determination of Surface Area and Porosity. De Gruyter: 2016.

50. Brunauer, S.; Deming, L. S.; Deming, W. E.; Teller, E., On a Theory of the van der Waals Adsorption of Gases. Journal of the American Chemical Society 1940, 62 (7), 1723-1732.

51. Dettmer, K.; Engewald, W., Ambient air analysis of volatile organic compounds using adsorptive enrichment. Chromatographia 2003, 57 (1), S339-S347.

52. Peters, R. J. B.; Bakkeren, H. A., Sorbents in sampling. Stability and breakthrough measurements. Analyst 1994, 119 (1), 71-74.

53. Fernandez, M. R. S.; Diaz-Marta, G. L. A., Adsorption-Thermal Desorption-Gas Chromatography Applied to the Determination of Wine Aromas. In Plant Volatile Analysis, Linskens, H. F.; Jackson, J. F., Eds. Springer Berlin Heidelberg: Berlin, Heidelberg, 1997; pp 175-192.

54. Pei, J.; Zhang, J. S., On the performance and mechanisms of formaldehyde removal by chemi-sorbents. Chemical Engineering Journal 2011, 167 (1), 59-66.

55. Soo, J.-C.; Lebouf, R. F.; Chisholm, W. P.; Nelson, J.; Roberts, J.; Kashon, M. L.; Lee, E. G.; Harper, M., Evaluation of Sorbent Sampling and Analysis Procedures for Acetone in Workplace Air: Variations of Concentration and Relative Humidity. Annals of Work Exposures and Health 2019, 64 (1), 96-105.

56. Park, J.; Govindan, M.; Kim, D., MgO modified zeolite facilitated low temperature chemisorptive removal of gaseous acetaldehyde into value added intermediate as desorption product. Chemosphere 2021, 276, 130281.

57. Staff, M. C. Humidifiers: Ease skin, breathing symptoms. (accessed 07/13).

VITA

Samantha Scudder

Candidate for the Degree of

Doctor of Philosophy

Dissertation: XPS CHARACTERIZATION OF DILUTE NITRIDE INDIUM GALLIUM ARSINIDE MATERIALS NANOPOROUS SILICA FOR ACTIVE SAMPLING OF ALDEHYDES

Major Field: Chemistry

Biographical:

Education:

Completed the requirements for the Doctor of Philosophy in Chemistry at Oklahoma State University, Stillwater, Oklahoma in December, 2021.

Completed the requirements for the Bachelor of Science in Biochemistry at Schreiner University, Kerrville, Texas in 2016.